國立交通大學

材料科學與工程學系

博士論文

無電鍍鈷鎢磷薄膜對銲錫之擴散阻障特性研究

A Study on the Diffusion Barrier Characteristics of Electroless Co(W,P) Thin Films to Solders

學生：潘虹君（Hung-Chun Pan）

指導教授：謝宗雍 博士（Dr. Tsung-Eong Hsieh）

中華民國 101 年 6 月

無電鍍鈷鎢磷薄膜對銲錫之擴散阻障特性研究

學生：潘虹君　　　　　　　　　　　　　　　指導教授：謝宗雍 博士

國立交通大學 材料科學與工程學系

摘　要

本論文研究以無電鍍（Electroless Plating）技術製備非晶態（Amorphous）與複晶態（Polycrystalline）之鈷鎢磷（Co(W,P)）薄膜，探討其對銲錫的擴散阻障（Diffusion Barrier）特性。研究的銲錫種類包括共晶錫鉛（Eutectic PbSn）、錫鉍（SnBi）與錫銀銅（SnAgCu，SAC），試片經液態時效（Liquid-state Aging）與固態時效（Solid-state Aging）後，分析 Co(W,P)與銲錫的合金反應及擴散阻擋能力。PbSn 與 SAC 系統並計算其介金屬化合物（Intermetallic Compound，IMC）成長之活化能（Activation Energy，E_a），並以推球試驗（Ball Shear Test）評估界面接合強度與破壞模式。

時效測試結果顯示，經液態時效之非晶態 Co(W,P)與銲錫反應生成之 IMC，在 PbSn 與 SnBi 系統中 IMC 主要爲 $CoSn_2$ 及 $CoSn_3$ 相，SAC 系統中 IMC 則爲 $CoSn_3$+$(Co,Cu)Sn_3$ 相；隨著時效時間的增加，IMC 會因球化（Spallation）而進入銲錫中，同時反應界面生成一由奈米尺度之 IMC 晶粒組成的複晶態富磷層（P-rich Layer），未反應的 Co(W,P)則有再結晶且析出 Co_2P 相等現象。固態時效試驗則觀察到層狀 IMC 生成於富磷層之上，且無球化行爲，且未反應之 Co(W,P)薄膜仍維持非晶態。

經液態與固態時效後，複晶態 Co(W,P)與銲錫反應生成一較厚的 IMC 層於非晶

態之富鎢層（Amorphous W-rich Layer）上，且無球化行爲；此一非晶態富鎢層無法阻擋銲錫與 Co(W,P)後續的合金反應，故阻障之能力應肇因於原子鍵結之特性，材料之結晶結構爲何不宜做爲擴散阻障機制的分類依據。

擴散阻障特性之研究結果顯示，非晶態 Co(W,P)爲複合式擴散阻障層，即犧牲型擴散阻障層（Sacrificial-type Barrier）與填塞型阻障層（Stuffed-type Barrier）之組合；複晶態 Co(W,P)則主要爲犧牲型擴散阻障層。IMC 成長之 E_a計算顯示，PbSn/非晶態 Co(W,P)系統之 E_a = 338.6kJ/mole，PbSn/複晶態 Co(W,P)系統之 E_a = 167.5 kJ/mole；SAC/非晶態 Co(W,P)系統之 E_a = 110.7 kJ/mole，SAC/複晶態 Co(W,P)系統之 E_a = 81.8 kJ/mol。

推球測試結果顯示 PbSn 系統及 SAC/poly-Co(W,P)試片之破壞模式以延性破壞（Ductile Mode）爲主，而 SAC/α-Co(W,P)試片在短時間熱處理下主要是界面破斷（Interfacial Break Mode），若經長時間熱處理則轉爲銲墊舉離模式（Pad Lift Mode）。分析結果顯示銲墊舉離模式肇因於高磷成分的非晶態 Co(W,P) 有礙於銲錫之潤濕性（Wettability）而降低界面接合強度，且 Co_2P 相析出及非晶態 Co(W,P)再結晶現象將導致未反應之 Co(W,P)脆化及熱膨脹係數改變進而產生熱應力。故無電鍍 Co(W,P)薄膜之磷含量不僅影響界面合金反應之行爲，也是影響其擴散阻障能力與銲錫接點可靠度的重要因素。

A Study on the Diffusion Barrier Characteristics of Electroless Co(W,P) Thin Films to Solders

Student: Hung-Chun Pan　　　　Advisor: Dr. Tsung-Eong Hsieh

Department of Materials Science and Engineering
National Chiao Tung University

Abstract

Diffusion barrier characteristics of electroless amorphous and polycrystalline Co(W,P) (termed α-Co(W,P) and poly-Co(W,P) hereafter) to eutectic PbSn, SnBi and SnAgCu (SAC) solders are investigated in this study. The samples were treated by liquid- and solid-state aging tests and the alloy reactions and diffusion barrier capabilities were evaluated. For PbSn and SAC systems, the activation energy of intermetallic compound (IMC) growth (E_a), interfacial bonding strength and failure modes were also analyzed.

In all solder/α-Co(W,P) samples subjected to liquid-state aging, spallation of IMC into solder, formation of a nano-crystalline P-rich layer at reacting interface, and the recrystallization of Co(W,P) containing Co_2P precipitates were observed. The IMCs observed in PbSn and SnBi samples were mainly $CoSn_2$ and $CoSn_3$, whereas that in SAC sample were mixture of $CoSn_3$ and $(Co,Cu)Sn_3$. As to solders/α-Co(W,P) samples subjected to solid-state aging, IMCs resided on the P-rich layer without spallation.

In the samples containing poly-Co(W,P), thick IMC neighboring to an amorphous W-rich layer was seen regardless of the solder and aging types. It was found that the amorphous W-rich layers could not inhibit subsequent alloy reactions. Hence, diffusion barrier capability should be correlated to the nature of chemical bonds, rather than the amorphism of microstructure. Moreover, α-Co(W,P) was a composite-type barrier, *i.e.*, sacrificial- plus stuffed-type barrier, while poly-Co(W,P) is mainly a sacrificial-type barrier. Analytical results indicated that the P content in Co(W,P) is a crucial factor affecting the structural evolution at the solder/electroless Co(W,P) interface.

The values of E_a's for IMC growth in PbSn/α-Co(W,P) and PbSn/poly-Co(W,P) samples were separately equal to 338.6 and 167.5 kJ/mol, whereas the E_a's of IMC growth were 110.7 and 81.8 kJ/mol for SAC/α-Co(W,P) and SAC/poly-Co(W,P) samples, respectively.

Ball shear test revealed the ductile mode dominates the failure in PbSn/α-Co(W,P), PbSn/poly-Co(W,P) and SAC/poly-Co(W,P) samples in most aging conditions, whereas interfacial break dominates at short-time aged samples and pad lift dominates when aging time was long in SAC/α-Co(W,P) case. Analytical results indicated that the decrement of bonding strength due to pad lift failure was ascribed to the deterioration of adhesion due to high P content, loss of toughness due to the formation of Co_2P precipitates and the thermal stress induced by the change of CTE due to the recrystallization in aged Co(W,P) layer although high P content might enhance barrier capability. The P content of electroless plating layer affects not only the alloy reactions at solder/Co(W,P) interface, but also the diffusion barrier characteristics and reliability of solder joints.

誌　謝

回想這些年來，我的心情很複雜，但我要感謝 神、我的父母以及身邊的許多朋友，陪我走過了這段不短的日子。

感謝 神的愛、寬恕和憐憫，在我還是罪人的時候就愛了我。我得罪了 神、得罪了人，但祂幫助了我，使我現在可以常常喜樂、感恩地度日。祂也在各方面都看顧、保護我，我真是一點都不想再過以前不認識 神的生活了。

謝謝家人及我的父母對我的包容跟愛護，你們的默默付出、關懷、溫暖、幫助、陪伴與支持是我繼續努力的動力，能成爲你們的孩子對我而言真是一個極大的恩典，感謝主、感謝你們。

感謝謝詠芬博士樂意提攜我們且提供公司機台使我們可以方便進行研究相關分析，在此一併感謝之。

另外還要感謝大師兄、教官、怡靜、Julie、勝結的陪伴，你們一輩子都是我的好朋友！謝謝皮皮、文成、角頭、努涵在研究的路上跟我同行，有你們我就不孤單；感謝重伊、國良，跟你們一起在閎康裡學習的相處時光總是很有趣；謝謝郁仁、賀昌、百樂、羅傑、泱泱、皓葦、大頭、胤諴、官官、宏吉、金毛、阿排……等實驗室同學、學弟妹們，你們的幽默、熱情跟貼心讓我印象深刻，也讓我最後在學校的日子充滿喜樂，世界有你們真美好！還有張翼老師實驗室、吳樸偉老師實驗室及陳智老師實驗室的同學們，謝謝你們在實驗上的幫忙；還要感謝蒙恩蒙愛裡的眾多弟兄姊妹們，你們的鼓勵、支持、陪伴、打氣給了我好大的勇氣，讓我能繼續勇敢地往前走，認識你們真是一件美好的事情，願 神紀念你們爲我所做的一切，謝謝你們。

最後，希望每個我所認識的朋友，都能喜歡自己、又能喜樂健康地生活在這個

世界上且擁有美好的人際關係、能認識 神、明白自己的價值，也希望大家能擁有無憾的人生！

Contents

Figure Captions

Table Captions

Chapter 1

Introduction

With the progress of scale-down of electronic products, the peripheral-array interconnection technologies such as wire bonding (WB) and tape automated bonding (TAB) were gradually replaced by the area-array technologies such as the flip-chip (FC) bonding in first level package. The advantages of FC bonding include high packaging efficiency, good electrical performance, high input/output (I/O) counts and compactness of electronic products. The FC bonding connects the integrated circuit (IC) chip and substrate with the bump joints which can be built up by solders, metallic posts, conductive polymer, anisotropic conductive adhesives, polymeric composites, pressure contact, *etc* [1]. Among these, solder alloys are the most common materials for the body of bump joint. However, the usage of solders require the under bump metallurgy (UBM) to prevent the interdiffusion in between solder and IC bond pad so as to ensure a reliable operation of electronic devices. UBM is a multi-layered thin-film structure comprised of the adhesion layer, diffusion barrier layer and passivation layer. Diffusion barrier layer is the most important component of UBM and refractory metal layers such as tungsten (W), molybdenum (Mo) and their alloys prepared by physical vapor deposition (PVD) processes such as *e*-beam evaporation and sputtering are commonly adopted as the diffusion barrier layers of UBM.

Recently, electroless plating technology, *e.g.* electroless nickel (EN), becomes a competitive diffusion barrier materials for the advantages of low cost, high throughput, good step coverage, *etc.* In addition, it was found that the stress status in EN is comparatively lower than that in the sputtered Ni [2] and the amorphous feature in EN provides no grain boundary for short-circuit diffusion and satisfactory barrier properties [3-6].

On the other hand, suppression of RC delay and electromigration (EM) are important issues in the trend of IC scale-down. As a result, new low-*k* dielectric materials (for low capacitance) and copper (Cu) (for low resistance) are separately brought in to replace traditional SiO_2 interlayer dielectric (ILD) and aluminum (Al) interconnects. However, Cu is a rather active element that its diffusivity in Si is as high as 10^{-4} to 10^{-5} cm^2/sec. A diffusion barrier layer must be inserted in between Cu interconnects and Si to avoid the degradations caused by interdiffusion. Similarly, an effective diffusion barrier layer must be implanted in the UBM when FC bonding is applied to Cu-ICs.

Electroless cobalt-phosphorus (Co(P)) may serve as the diffusion barrier material for Cu metallization and a superior barrier capability to inhibit the interdiffusion between Cu and ILD has been reported [7]. Feasibility of Co(P) layer to the diffusion barrier layer of Cu and PbSn solder was also demonstrated [8]. Previous studies [9-11] reported the enhancement of thermal stability and diffusion barrier capability to Cu metallization by adding the tungsten (W) element in electroless Co(P). In addition, it has been illustrated that the amorphous electroless Co(W,P) is a mixed-type barrier, *i.e.*, a combination of sacrificial- and stuffed-type barrier, to PbSn solder and Cu [12]. Since electroless Co(W,P) exhibited a promising capability as a diffusion barrier, a further study is hence required in order to realize its applications as the diffusion barrier to present solder types.

This thesis studies the barrier characteristics of electroless Co(W,P) to solders including eutectic PbSn, SnBi and SnAgCu (SAC). Both amorphous and polycrystalline Co(W,P) layers were prepared, the alloy reactions and morphology evolution at the reacting interfaces in the samples subjected to liquid-state aging at 250°C and solid-state aging at 120 to 150°C were investigated so as to deduce the diffusion barrier characteristics of Co(W,P) to solders. The activation energy of IMC growth (E_a) and the bonding strength of Co(W,P)/PbSn and Co(W,P)/SAC systems were also evaluated so as to gain an in-depth understanding on the applicability of electroless Co(W,P) as the diffusion barrier layer to solders.

Chapter 2

Literature Review

2.1. Trends of IC Interconnection Technologies

In recent years, the very large scale integrated circuit (VLSI)/ultra large scale integrated circuit (ULSI) technology has profoundly advanced. With the continuous scale-down of VLSI/ULSI, multi-layer interconnect structure becomes an important issue in IC design. Though the IC scale-down effectively reduces the gate delay, it nevertheless drastically increases the interconnect delay, in particular in the

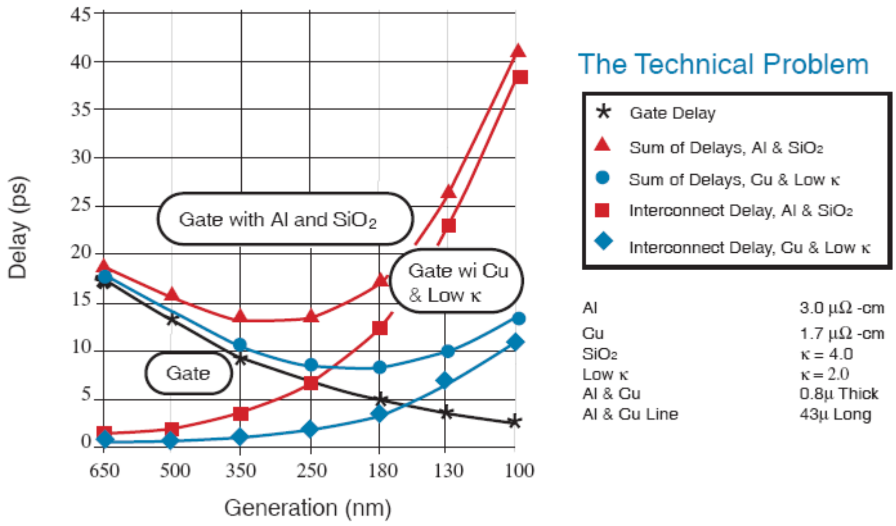

Figure 2-1. The contributions to RC delay from interconnect and gate in Al- and Cu-ICs [13].

conventional ICs within Al as the conducting line and SiO_2 as the ILD as illustrated in Fig. 2-1. The shrinkage of conducting line width also escalates the current density and consequently leads to the electromigration (EM) failure, resulting in the reliability concerns of electronic products. In order to overcome the difficulties caused by IC scale-down, new low-*k* dielectric material (for low capacitance) and Cu (for low resistance) are hence brought in present IC manufacture to replace traditional SiO_2 ILD and Al interconnects.

2.1.1. Cu Metallization

Cu metallization is a key breakthrough in contemporary IC manufacture when IBM announced the Cu-IC technology in early years of 90 [14-16]. The Cu metallization is also termed as the damascene technology (see illustration in Fig. 2-2 [17]) which is accomplished by a series of processes including photolithography to define the via position, PVD or electroless plating to fill the Cu in via holes, and chemical mechanical polishing (CMP) to polish off the unnecessary Cu. The advantages of Cu metallization for Si ICs include low resistivity and high EM resistance. In addition, the higher melting point and better mechanical property of Cu than those of Al lead to a higher sustainable current density, a lower failure rate of circuit and the improvement of IC reliability. However, there are some disadvantages of Cu metallization and the solutions are listed as below:

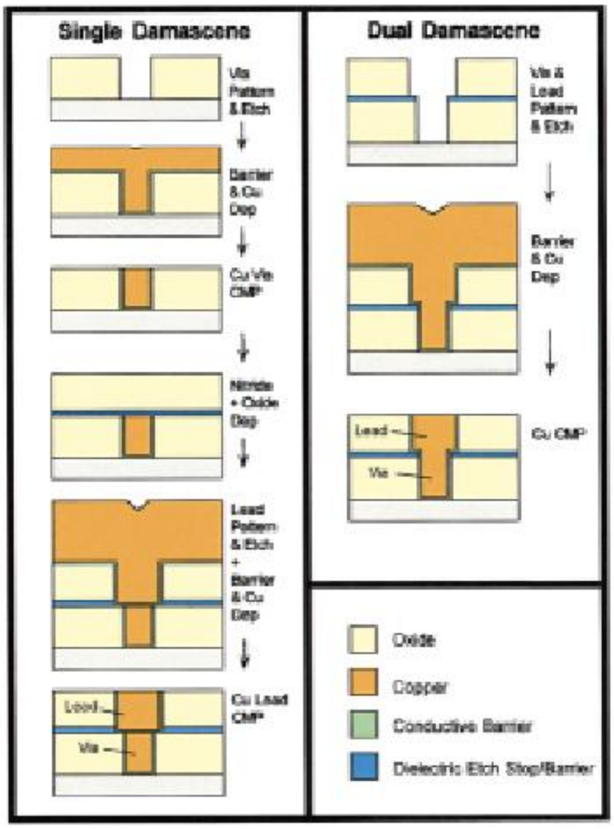

Figure 2-2. Single and dual damascene processes [17].

(1) High surface corrosion: Cu oxidizes rapidly at high temperature in air. Unlike the protective oxide formed on Al alloys to improve the corrosion resistance, Cu oxidizes even in relatively high vacuum with the slightest amount of water vapor. Hence, there are methods for preventing Cu from oxidization, *e.g.*, surface silicidation (a protective layer formed by annealing Cu in SiH_4 ambient [18]),

copper alloying (adding a small amount of magnesium (Mg), Al, or boron (B) [19-22] in Cu), *etc*.

(2) Chemical etching method: Cu is extremely difficult to be etched. When dry etching a specific pattern, the by-products are hard to evaporate away because of the lower vapor pressure of Cu halogenide. As illustrated in Fig. 2-2, dual damascene in conjunction with the CMP technology is used to overcome this manufacture difficulty [23-24].

(3) Poor adhesion: The adhesion between Cu and ILD is poor so that an adhesion layer has to be added to improve the adhesion strength.

(4) High diffusion rate: Cu diffuses into SiO_2 and Si in a relatively fast rate (the diffusivity of Cu in Si is about 10^{-4} to10^{-5} cm^2/sec) and results in device failures. For instance, Cu might induce stacking faults in SiO_2, leading to the high leakage current and low breakdown voltage in ILD. The Cu impurity in Si generates the deep defect levels in the bandgap of Si which, consequently, becomes the recombination centers to trap the electrons and decreases the life time of electrons in conduction band [25]. The life time decrement of charge carriers will prolong the reaction time and deteriorate the device efficiency.

2.2. Introduction to Electronic Packaging

The IC chips are rarely used in bare form; they have to be “packaged” for subsequent shipping/handling processes so that they can be assembled with other active/passive components to accomplish a specific operational function. Electronic packaging starts from the interconnection and encapsulation of monolithic IC chips, subsystem/system assembly to product finish as illustrated in Fig. 2-3 [1]. It provides four basic functions, *i.e.*, power distribution, signal propagation, heat dissipation, and mechanical support/protection. In the trend of device scale-down, packaging technology becomes a bottleneck for further upgrading the performance of electronic products. In recent years, many new packaging concepts, *e.g.*, ball grid array (BGA), chip scale package (CSP), direct chip attach (DCA), wafer-level packaging (WLP), *etc*., have been introduced in order to overcome the limitations resulted from traditional technologies. As to the interconnect technology, FC bonding resumes its active role in the market even though it is in fact an old concept originated from the controlled collapse chip connection (C4 or C^4) for solid logic technology (SLT) proposed by IBM in early 1960s [26] as shown in Fig. 2-4 [1]. The trend of performance upgrading, miniaturization and versatile functionality has driven FC bonding as a popular interconnect method for advanced electronic products. Presently, a vast amount effort has been poured into the research and development of FC bonding and its market share is expected to grow drastically in near future.

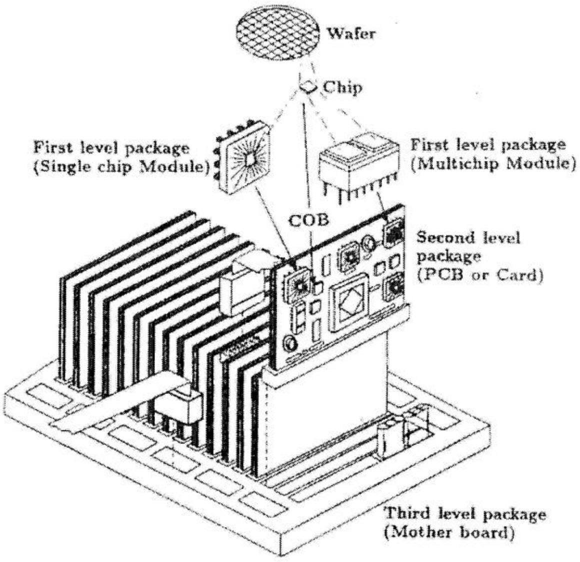

Figure 2-3. The first three levels of electronics packaging [1].

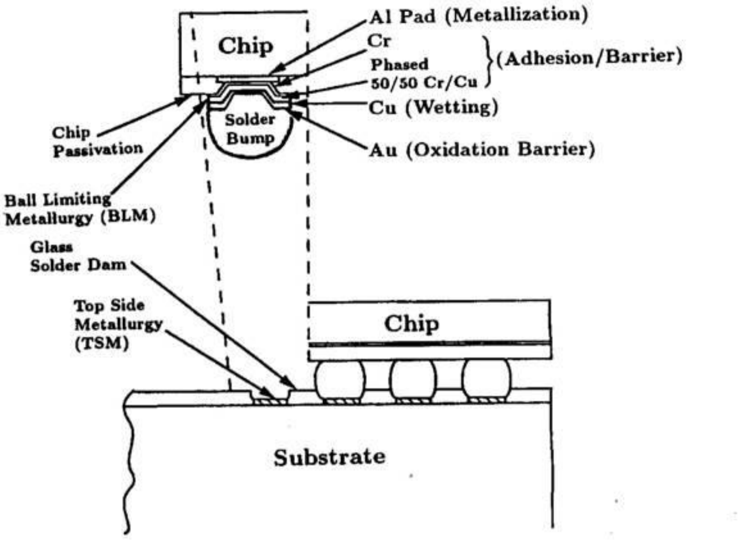

Figure 2-4. C4 technology proposed by IBM [1].

2.2.1. Interconnect Technologies of Electronic Packaging

There are three main interconnect technologies for first level packaging, *i.e.*, WB, TAB, and FC bonding as described in Fig. 2-5 [27]. Both WB and TAB are peripheral-type interconnection technologies so that they have limited I/O counts and packaging efficiencies. On the contrary, FC bonding is area-type interconnect method which allows a comparatively high I/O counts (> 10^4) and packaging efficiency (> 90%). Presently, WB dominates the market due to its technical simplicity and maturity whereas the application of TAB is limited to some specific products, for instance, the packaging of driver IC for liquid-crystal display (LCD). In comparison with WB, FC bonding is in fact a relatively complicated and expensive interconnect method so that in early years its utilization was only seen in some sophisticated electronic products such as supercomputers and work stations.

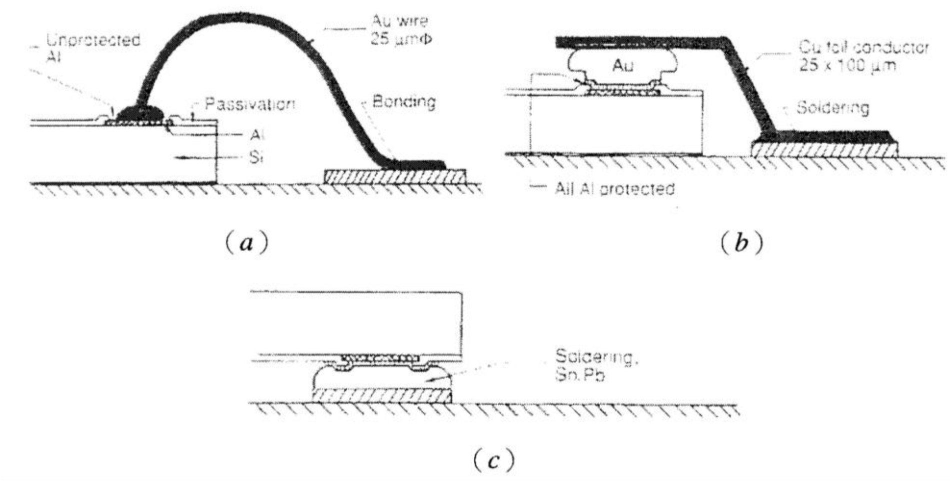

Figure 2-5. Schematic illustrations of (a) WB, (b) TAB, and (c) FC bonding [27].

Since the announcement by IBM in early 1960s, FC bonding has been recognized as an interconnect technology which bonds the IC chips in face-down manner on substrate by using a specific conducting material or interconnect concept. In typical FC bonding flow, die bumping and substrate metallization are separately accomplished and then the bumped die is attached to the substrate *via* appropriate thermal treatment. In most cases, polymeric resin will be injected into the gap in between the die and substrate after the completion of bonding. It forms the adhesive bonds so as to alleviate the thermal stress induced by the difference of thermal expansion coefficients (CTEs) of die and substrate. The bumps are not only the power/signal conducting paths in between the chip to substrate, but also the heat dissipation paths and mechanical support of the packaging structure. The FC manufacturing process flow is illustrated in Fig. 2-6 [1].

2.2.2. Structure of Solder Bump Joints

As stated previously, the bumps for FC bonding can be accomplished by various materials and fabrication processes. PbSn solders are the most common material for bump body. IBM used the high-temperature solder containing 97 *wt*.% of Pb for C4 technology whereas eutectic PbSn is the most common solder type compatible with the reflow bonding process. As a matter of fact, solders with various stoichiometric formulations have been developed and, with the call for environmental protection, Pb-free solders are flourishing in recent years. Though still not a complete drop-in solution for conventional PbSn solder, SnAg, SnCu, SnBi, and SnZn are promising Pb-free solders. The SnAg alloy doped with a moderate amount of Cu, SnAgCu (SAC), is well recognized for bumping fabrication due to its suitable physical and mechanical properties.

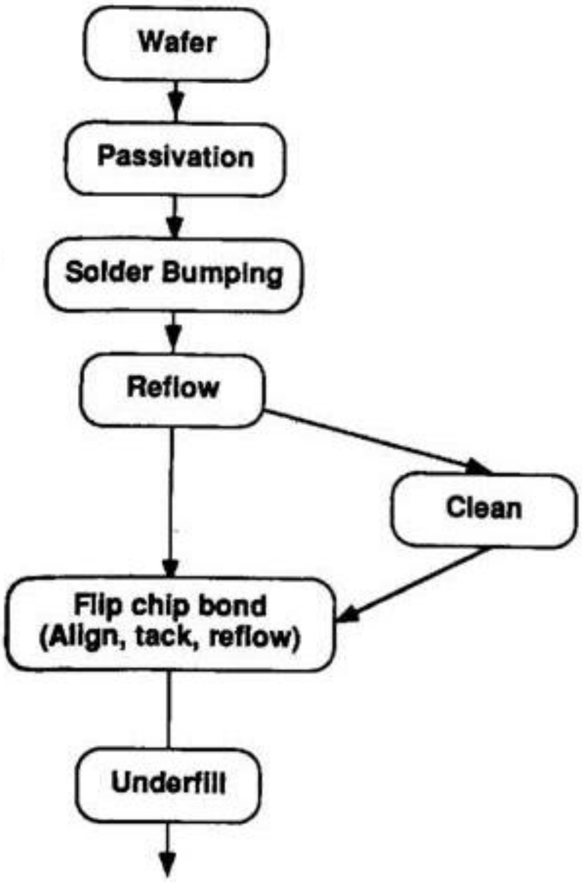

Figure 2-6. Typical process flow of FC bonding [1].

UBM is another essential component of FC bump structure. As shown in Fig. 2-7, it comprises of the adhesion layer, diffusion barrier layer and passivation layer commonly prepared by PVD methods. The functions of each layer in UBM are described as follows.

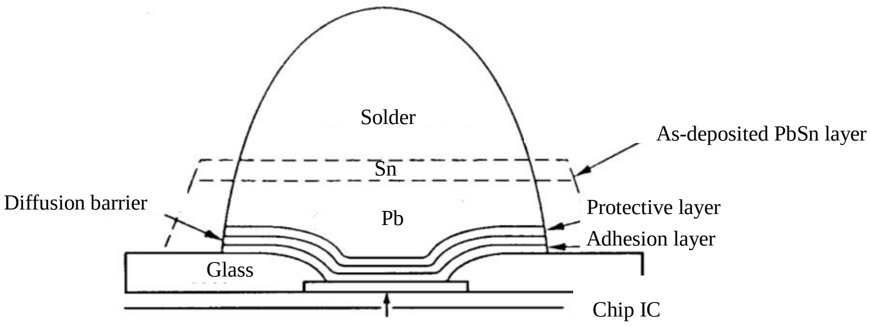

Figure 2-7. Solder bump structure [28].

(1) Adhesion layer is to ensure reliable adhesive strength in between IC bond pad and subsequent metal layer. Materials such as titanium (Ti), chromium (Cr), and tantalum (Ta) are common adhesion layers.

(2) Diffusion barrier layer is to impede the interdiffusion in between IC bond pad and bump body materials. Such a barrier layer plays a key role in maintaining the integrity of bump joint and the most common materials are refractory metals such as W, Mo and their alloys. In addition, EN layer is also a popular material for barrier purpose in presented days.

(3) Passivation layer is also called the protective or anti-oxidation layer. In some cases, a wetting layer is added in between the passivation layer and underlying diffusion

barrier layer to ensure good wettability of solder when the bump joints are formed. Cu is the common wetting layer material whereas noble metals such as gold (Au) and palladium (Pd) are frequently adopted as the passivation layer.

2.2.3. Classifications of Diffusion Barrier Layers

As mentioned above, a diffusion barrier layers impede the interdiffusion in between the IC bond pad and bump body materials. It is possible to have the diffusion barrier layer chemically inert to the bond pad materials; nevertheless, this means that there is no alloy reaction in between these two layers and, hence, their bonding strength would be too poor to form the sustainable bump joint. In practice, alloy reactions are expected to occur in between the barrier layer and bond pad material, however, the extent of reactions must be minimized to avoid a dramatic alternation on structural integrity. The performance of diffusion barrier layer is hence correlated to its sustenance to various annealing environments. An ideal diffusion barrier layer for UBM applications must be thermodynamically stable, low contact resistance, high adhesion property, high tolerance to thermal and mechanical stresses, and high electrical conductivity.

According to N.A. Nicolet [29], diffusion barrier layers can be divided into four categories according to the principles to inhibit the interdiffusion, *i.e.*, sacrificial-type barrier, stuffed-type barrier, passive-type barrier and amorphous-type barrier. The features of each kind of diffusion barrier layer are briefly described as follows.

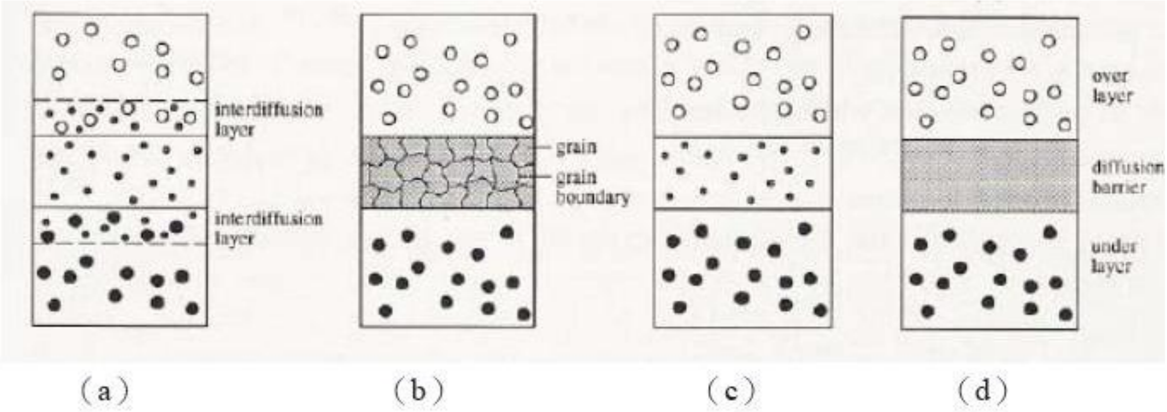

Figure 2-8. Classification of diffusion barrier layers: (a) sacrificial-type, (b) stuffed-type, (c) passive-type, and (d) amorphous-type diffusion barrier layers [29].

(1) Sacrificial-type barrier layer reacts with the bump body material until it is totally exhausted as illustrated in Fig. 2-8(a).

(2) Stuffed-type barrier layer prevents the diffusion by forming obstacles in fast-diffusion paths such as grain boundaries. Insertion of impurity atoms or formation of precipitates in grain boundaries is a common method to induce the stuffed-type barrier capability. An illustration of stuffed-type barrier is depicted in Fig. 2-8(b).

(3) Passive-type barrier layer prevents the alloy reactions in between the diffusion barrier layer and bond pad material by inserting a material which is thermodynamically stable and chemically inert to the bump body and bond pad materials as illustrated in Fig. 2-8(c).

(4) Amorphous-type barrier layer eliminates the grain boundary diffusion since such fast diffusion paths are absent due to the structure irregularity as illustrated in Fig. 2-8(d). Surely grain boundaries are also absent in single crystalline materials, however, single crystalline diffusion barriers are impractical since their preparation is relatively complicated. An amorphous substance with high recrystallization temperature may serve as the amorphous-type barrier.

Except for the material characteristics of diffusion barrier itself, the manufacturing process affects the diffusion barrier capability as well. The common diffusion barriers for Cu metallization are Ta, TaN, TiN, *etc*. However, the step coverage property of above thin films made by PVD is poor. Recently, EN, electroless Co(P) and Co(W,P) layers are benefit on good step coverage, uniform film quality, selective deposition [30], low-temperature process, lower resistivity than other refractory materials and lower manufacturing cost so that they are popular barrier material in recent years.

Taking the crystal structure into consideration, the diffusion barrier layers were also classified as single crystal, void-columnar poly-crystal, equiaxed columnar poly-crystal, nanocrystalline and amorphous barriers as illustrated in Fig. 2-9 [31].

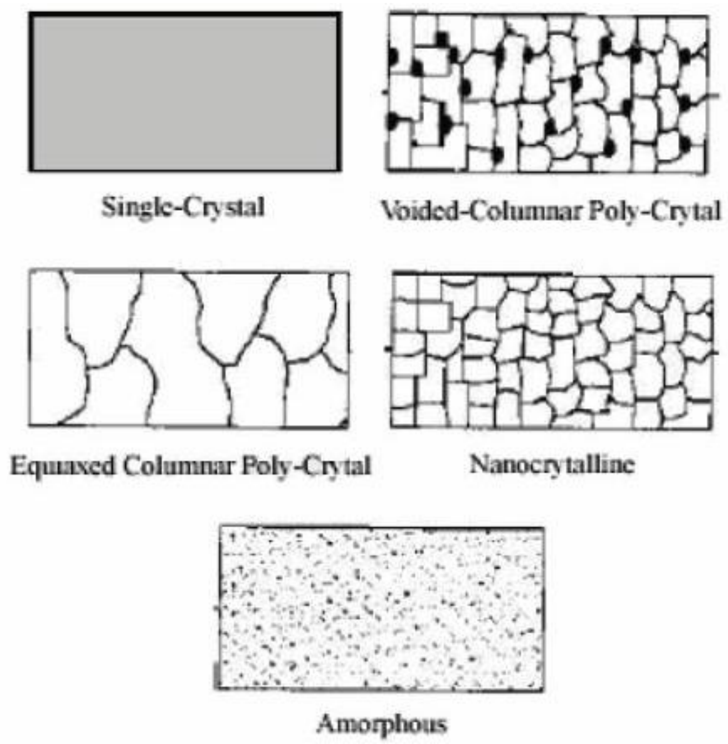

Figure 2-9. Illustrations of the structures of diffusion barrier layers [31].

It is well-known that grain boundaries are the fast diffusion paths, hence, the equiaxed columnar poly-crystal could hardly provide the satisfied diffusion barrier capability whereas the single-crystal and amorphous layer do. It is difficult to grow single crystal layer, but it is rather easier to obtain an amorphous film by PVD or electrochemical deposition method. When using electrochemical deposition method to prepare thin films, it is not under a thermodynamic equilibrium state so that amorphous structure is easy to form.

2.3. Reactions between Solder and Underlying Metals

It is well-known that alloy reactions occur when solder contacts with conductor metals (*i.e.* UBM, boards surface finishes, *etc*) directly during soldering. Intermetallic compounds (IMCs) will form and grow at the reacting interfaces, providing a good metallurgical bonding. However, excessive IMCs might affect the mechanical reliability of the joints for the inherent brittle feature and the tendency to generate structural defects such as Kirkendall voids. Hence, the materials selected as diffusion barrier should have lower reaction rate when soldering [32-38]. In principle, the IMC layers are formed in three consecutive stages: the dissolution of contact metal into the molten solder until solder is supersaturated with the dissolved metal throughout the interface, chemical reactions and solidification of IMCs [38]. During storage or in-use of the assemblies, the initial formed IMCs during soldering grow thicker or increase in number. Therefore, both solid/liquid and solid/solid systems must be studied to as to secure a better understanding on the reliability of soldered assemblies [38].

2.3.1. Reactions of Solders with Cu-based Metals

For Cu-based conductor metal reacting with Sn-based solder, IMCs such as Cu_3Sn (ε) and Cu_6Sn_5 (η) phases could form as indicated by the Cu-Sn binary phase diagram in Fig. 2-10 [39]. The Cu_6Sn_5 has two types of phases. The η' phase, the ordered long-period superlattice (LPS) based on the NiAs-type structure, is stable at room temperature [40-42]. Another phase type is the high-temperature η phase, also possessing NiAs structure. The equilibrium transformation temperature of η into η' phase is 186°C. During soldering and subsequent cooling, the time for the

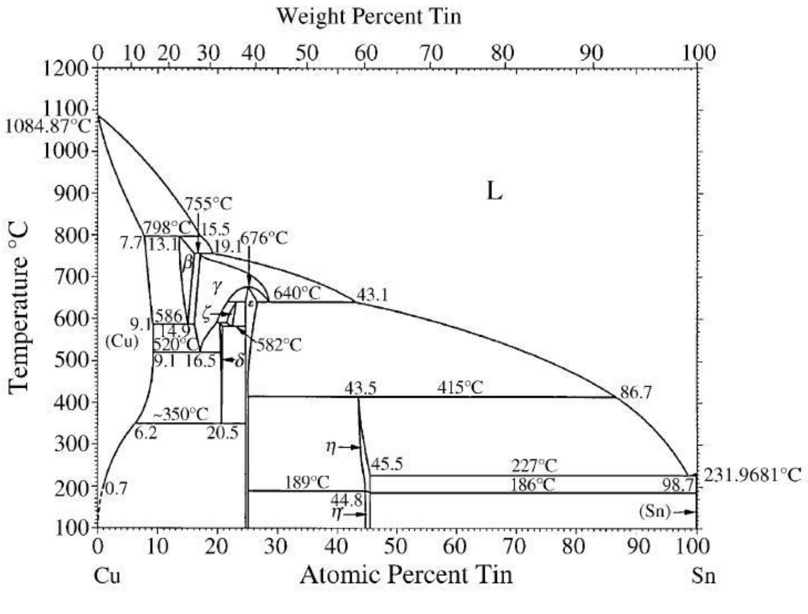

Figure 2-10. Cu-Sn binary phase diagram [39].

transformation from η into η' is in general not sufficient so that the η remains as the metastable phase [39] and the differential scanning calorimeter (DSC) measurements found that the transformation starts after 6-min thermal annealing at 175°C [43]. As to the ε phase, it was also reported possessing a long-period superstructure [43], but the ordering temperature is not as well defined as that of the η-phase. When Cu reacts with molten Sn, it dissolves rapidly and locally supersaturated in the vicinity of interface. At the metastable composition regions, Cu_6Sn_5 precipitates vary fast by the heterogeneous nucleation and growth at the Cu/liquid solder interface [38]. The thickness and the morphology of the IMCs is firstly determined by the Cu dissolution rate in liquid and the chemical reaction between Sn and Cu, and secondarily, by the diffusion of Cu into the liquid [38]. Notably, each of the Cu_6Sn_5 crystallites grows independently from the adjacent ones, and the roughness of interface was found to have an effect on the formation of the Cu_6Sn_5 crystallites. The rougher the surface is, the more crystallites will form per unit area [44]. Afterward, the IMC growth rate gradually slows down for the decrease of the dissolution of Cu to the molten Sn when IMCs formed. After extending the contact times, a thinner Cu_3Sn layer forms between Cu and Cu_6Sn_5 layer. The formation mechanism of the Cu_3Sn phase is diffusion and reaction type growth, in contrast to the mainly dissolution and reaction controlled formation of the Cu_6Sn_5 phase [38]. As to solid Cu/solid Sn reactions, Sn was the main diffusion species rather than Cu [45-47]. The grain boundary and interstitial diffusion mechanisms dominate over vacancy-mediated diffusion at relatively low temperatures with respect to the melting points of the corresponding materials (with metals 0.3-0.5T_m) [38,48-49]. In addition, the activation energy (E_a) for the interdiffusion in Cu_3Sn phase appears to be higher than that of Cu_6Sn_5 phase [46,50]. Therefore, the growth rate of the Cu_3Sn layer should require somewhat higher temperatures than the growth of the Cu_6Sn_5 layer. Cu_3Sn phase is reported to grow at the expense of the Cu_6Sn_5 phase and mainly consists of the columnar grains parallel to the diffusion direction, indicating either grain boundary diffusion is controlling the phase formation or that there is strong anisotropy in the growth of the Cu_3Sn phase in solid-state aging [51].

2.3.2. Reactions of Solders with Ni-based Metals

Owing to the high reaction rate of Cu and molten Sn, Ni is often used as a diffusion barrier layer in between Cu and Sn to obtain a thinner IMC layers in the Sn-Ni system. It has been reported that there are three IMCs stable below 260°C, *i.e.*, Ni_3Sn, Ni_3Sn_2, and Ni_3Sn_4 phases as shown by the Ni-Sn binary phase diagram in Fig. 2-11. Ni_3Sn phase has two structures (low-temperature hexagonal form and high-temperature cubic form) [39]. Ni_3Sn_2, has more than one structures. As indicated by the Ni-Sn binary phase diagram [39], Ni_3Sn_2 has a hexagonal closed-packed Ni-As structure at low temperatures (LT) and a hexagonal or orthorhombic symmetry at high temperatures (HT). Other researches described a hexagonal structure with partially filled $InNi_2$ structure for the Ni_3Sn_2 HT-phase [52-58], whereas the Ni_3Sn_2 LT-phase has one orthorhombic structure [54] or three different LT-phases two of which have incommensurate structure [52,56-58]. The transition temperature has been identified as 600°C [39], 477°C [56] or 517°C [58] or in a range of 295°C to 508°C [52]. Ni_3Sn_4 possesses only the monoclinic structure [39]. During soldering, Ni_3Sn_4 phase, rather than the Ni_3Sn or Ni_3Sn_2, forms at interface, even though Ni_3Sn_4 is the least thermodynamically stable compound and it possesses the most complicated structure among all Ni-Sn IMCs [38-39]. The reaction starts by the dissolution of Ni to molten Sn, with subsequent diffusion of Ni inside the liquid and chemical reactions to form Ni_3Sn_4. The dissolution of Ni is essentially stopped after the formation of the Ni_3Sn_4, and further growth of Ni_3Sn_4 occurs by diffusion of Sn through the IMC layer when Ni_3Sn_4 continuously forms at the interface [38]. Bader *et al.* [59] reported that Ni_3Sn_4 has three different morphologies simultaneously when Ni/molten Sn reaction starts: a fine-grained and planar layer at the Ni interface, long, thin, idiomorphic whiskers, and large, polygonal idiomorphic crystals. During liquid-state aging, the whiskers coarsen and transform to the large crystals, and the Ni_3Sn is the latest phase to form. Bader *et al.* [59] also pointed out that grain boundary diffusion of Ni dominates the phase growth at 240-300°C. As to the case solid Ni reacts with solid Sn, the growth rates of the stable Ni-Sn IMCs are quite slow and out of them only Ni_3Sn_4 can be detected [38,51,60], and the growth kinetics of the Ni_3Sn_4 phase appears to be parabolic and thus diffusion controlled [51]. Oh [51] found that Sn is the only diffusing species during the formation of Ni_3Sn_4, and the plausible reasons for the absence of Ni_3Sn and

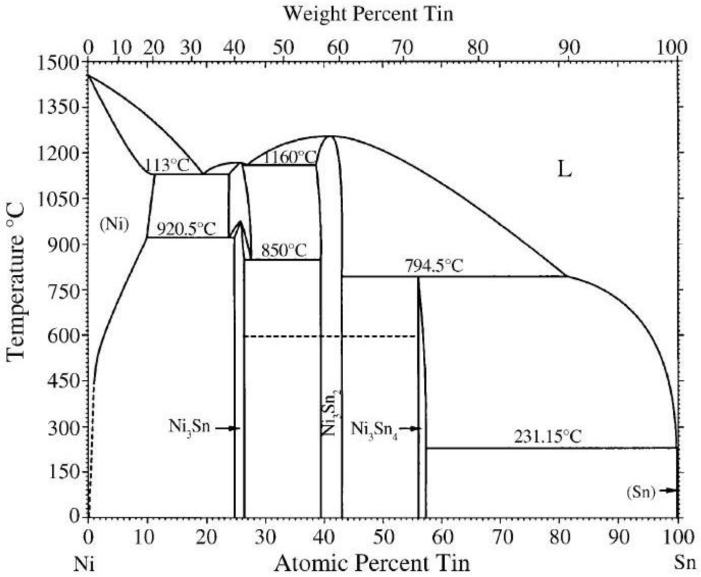

Figure 2-11. Ni-Sn binary phase diagram [39].

Ni_3Sn_2 phases are difficult nucleation and/or slow diffusion behavior in the missing phases. Only the micro-scale roughness promotes the nucleation of Ni_3Sn and Ni_3Sn_2 at temperatures as low as 100°C. However, Haimovich [60] pointed out the existence of platelet morphology of the metastable $NiSn_3$ compound and found that Pb effectively decreases the growth of the metastable phase when annealing in the temperature range of 75-232°C.

Notably, when using PbSn solder or pure Sn to react with Ni, the Ni_3Sn_4 phase is the first phase to form at the Sn/Ni interface. However, when using Pb-free solders that include even small amounts of Cu, the first phase to form is $(Cu,Ni)_6Sn_5$ [38,61-63]. Some Cu atoms in the Cu sublattice of the metastable $(Cu,Ni)_6Sn_5$ can be replaced by Ni [63]. This is owing to the fact that the dissolution of Ni to molten solder is much faster than the diffusion of Cu or Sn into solid Ni.

2.3.3. Electroless Ni(P) Applied on Conductor Metals

Electroless plating is promising for FC application due to its lower reaction rate and lower cost of the bumping process, hence, there are numerous researches on the reactions between EN UBM and solders in recent years [63-76]. There are about 7-9 *wt*.% (12-16 *at*.%) of phosphorus (P) contents in EN UBM since hypophosphite is used as the reducing agent during electroless plating. During aging, Ni reacts with solder to form Ni_3Sn_4 IMCs [77], hence, the deposition layer should be thick enough, generally about 5-6 μm in thickness [78], to retard the further diffusion. Consequently, the EN layer is enriched by P and formation of P-rich region or a Ni_3P layer with columnar grain structure [69,79]. It is reported that Ni_3P grows by the grain-boundary diffusion of Ni atoms or an interstitial diffusion of the P through the Ni_3P layer [69], and the Ni_3P layer embrittles the joint and results in the mechanical failures. Some researches pointed out that the Ni_3P layer is caused by the solder assisted crystallization of the amorphous EN layer [70,79-80] as shown in Fig. 2-12 [79].

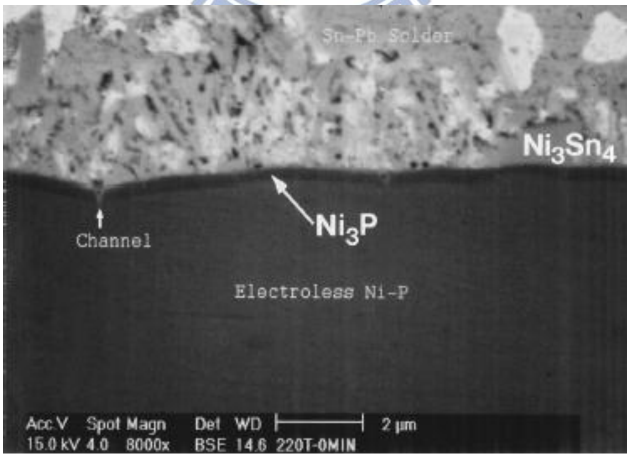

Figure 2-12. Cross-sectional SEM view of PbSn/Ni(P) sample subjected to 220℃ annealing for 30 sec [79].

Liu *et al*. [70] reported that the P-rich region was the mix of Ni_3P and Ni after reflow (15 min at 130-160°C followed by 5 min at 215°C) using as-deposited, approximately 12.5 *at.*% (about 6.5 *wt.*%) P, and amorphous or nano-crystalline EN film. The mixture of Ni_3P and Ni indicates that the Ni(P) layer has partially crystallized, and the unreacted EN remains amorphous or nanocrystalline. The solubility of P in crystalline EN was much smaller than that in the amorphous phase so that the extra P was rejected from the crystallized layer, followed by reaction with available Ni to form Ni_3P. This phenomenon is the so-called solder assisted crystallization. After the aging at 170°C for 15 days, Ni_3P-plus-Ni layer transformed to Ni_3P because of the more P diffusion in Ni_3P-plus-Ni layer, and Ni_3Sn_4 layer grew considerably in thickness (from 0.7 to 4 mm). However, when the aging was extended to 30 days, complex structures consisting of Ni_3Sn_4, Ni_3Sn_2, $Ni_{12}P_5$, and $Ni_{12}P_5$ plus Ni_3P appeared, and the Ni(P) layer was fully consumed. The formation of Ni_3Sn_2 and $Ni_{12}P_5$ was attributed to Sn diffusion through the Ni_3Sn_4 layer and following reaction with Ni_3P. Matsuki *et al*. [71] reported four distinct IMCs, *i.e.*, Ni_3Sn_4, orthorhombic $Ni_{48}Sn_{52}$ (also been previously proposed by Bhargava and Schubert [74]), Ni_2SnP, and Ni-P can be seen after the reflow using EN containing 14 *at.*% P. Vuorinen *et al*. [63] studied the interfacial reactions between SAC solder and amorphous (16 *at.*% P) EN/Au surface finish on printed wiring boards. After reflowed five times, columnar

Ni_3P layer between the EN and $Ni_{55}Sn_{35}P_{10}$ and $(Cu,Ni)_6Sn_5$ IMCs formed at the interface, which was observed by transmission electron microscopy (TEM).

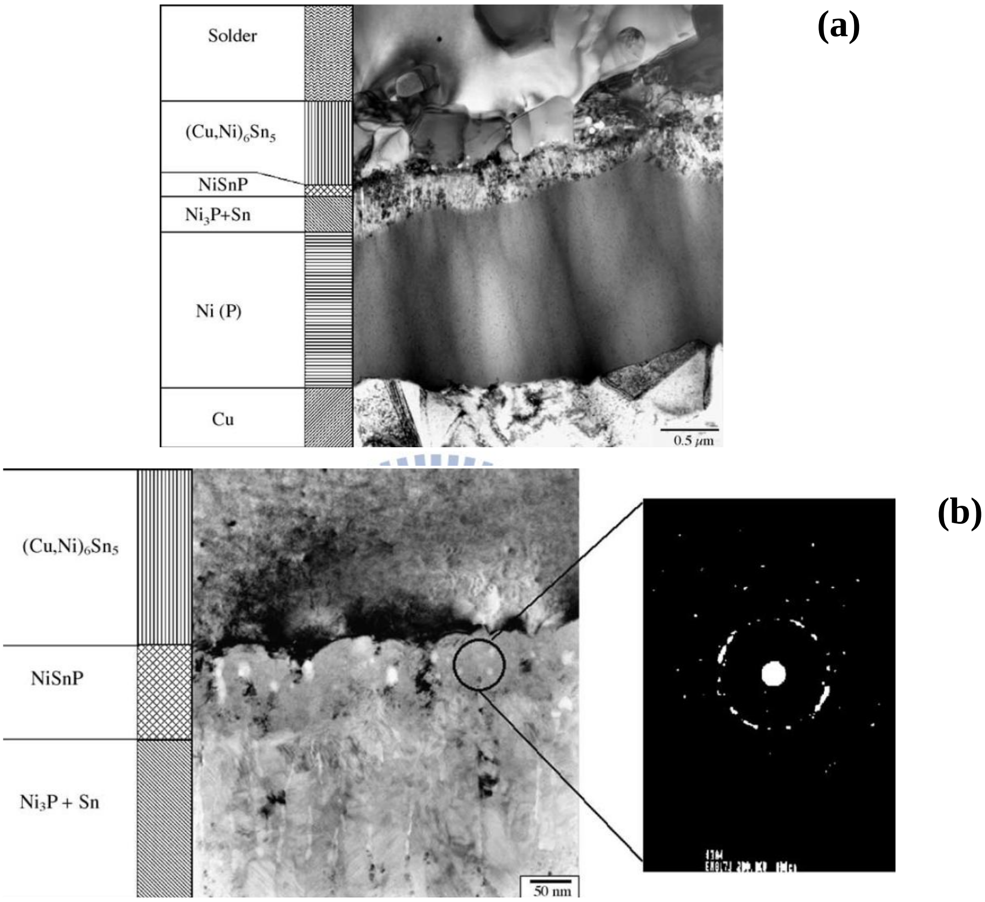

Figure 2-13. (a) TEM view of SAC/Ni(P) interface after reaction. (b) TEM view of the IMC and P-rich region and the diffraction pattern taken from the NiSnP layer [63].

In addition, the diffraction pattern taken from the NiSnP layer showed that it is not amorphous but nano-crystalline (see Fig. 2-13(b)). Vuorinen *et al*. [63] further reported that when P is high enough, Ni_3P seemed to be suppressed by NiSnP layer.

This phenomenon is resulted from the formation of a new liquid (L2) consisting of supersaturated P in between solid Ni(P) and the bulk liquid solder (L1) [38,63] due to the presence of metastable liquid miscibility gap in the Sn-P system [39]. During cooling, the nanocrystalline NiSnP layer solidified and transformed into more stable crystalline compound Ni_3P with columnar structure gradually. Other researchers [81-83] proposed that the NiSnP layer should result from the Sn diffusion into Ni_3P layer and cause the IMCs spallation.

It has been mentioned that when Ni-based conduct metal reacts with molten solder, Ni_3Sn_4 IMCs form at the interface, however, when solders contain Cu, $(Cu,Ni)_6Sn_5$ would form at the interface [38,61-63]. $(Ni,Cu)_3Sn_4$ and $(Ni,Cu)_3Sn_2$ IMCs were reported as well [75,81-84]. The formation mechanism of the complex reaction layer structure requires further investigation.

2.3.4. The IMC Phase Types in Co-Sn Phase Diagram

It is essential to understand the IMC types formed by the reactions of Co and Sn in order to realize the applications of electroless Co-based thin films as the diffusion barrier layers in UBM [3,8,12,31,85-87]. As illustrated by the Co-Sn binary phase diagram in Fig. 2-14 [88], several Co-based IMCs, *e.g.*, Co_3Sn_2, CoSn, and $CoSn_2$, may stably exist at temperature below 260°C. TheCo_3Sn_2 has two modifications below 500°C: the Co_3Sn_2 HT-phase (β) with hexagonal NiAs structure and the Co_3Sn_2 LT-phase (α) with orthorhombic Ni_3Sn_2 structure which is stable. Calculation of Jiang *et al.* indicated that the order-disorder transition of β-Co_3Sn_2 and α-Co_3Sn_2 phases occur at 563 to 568°C [89]. As to the CoSn, it possesses the hexagonal structure and is stable up to the peritectic temperature of 936°C. The $CoSn_2$ possesses tetragonal Al_2Cu structure and is stable below 525°C. The solid solubility of Co in tetragonal Sn solid solution is negligible, whereas that of Sn in α-Co is about 2 *at.*% Sn at 1033°C and about 1.67 *at.*% Sn in ε-Co at 536°C.

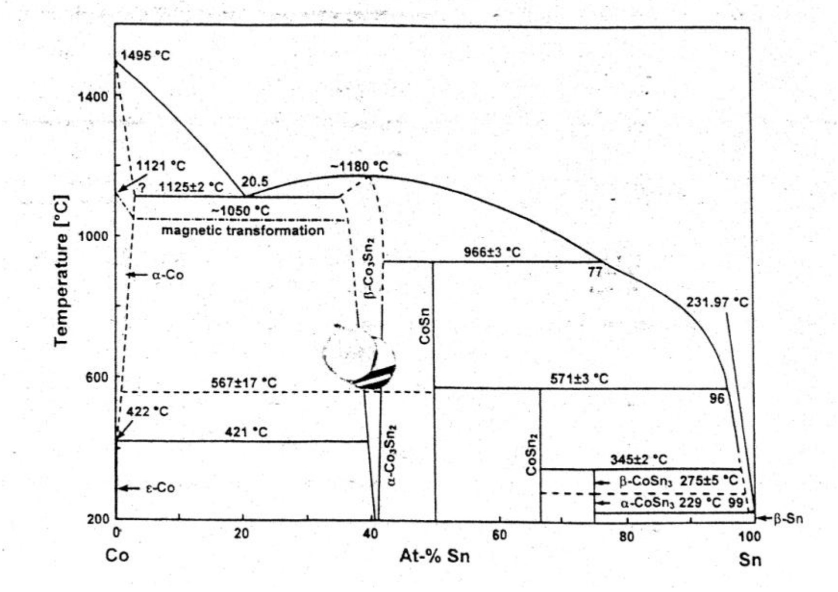

Figure 2-14. Co-Sn binary phase diagram [88].

Lang and Jeitschko reported the presence of α- and β-$CoSn_3$ [88]. The HT β-phase formed *via* the peritectical reaction of $CoSn_2$ with the Sn-rich melt at 345±2°C, whereas the LT α-phase is stable below 275±5°C and possesses the $PdSn_3$ structure. Jiang *et al.* calculated the formation enthalpy of solid Co-Sn at 298°K and found that the CoSn phase is the most thermodynamically stable IMC [89]. However, CoSn phase is rarely observed when metallic Co reacts with solders. Zhu *et al*. pointed out that CoSn emerges at 873°K while $CoSn_2$ forms at 673 and 773°K in the Sn/Co diffusion couples [90]. Zhu *et al*. also reported the presence of $CoSn_3$ at 573°K [91]. Wang and Chen found that $CoSn_3$ is the main product in the Sn/Co couples annealed at temperatures ranging from 150 to 200℃ and the meta-stable $CoSn_4$ phase forms at the corner [92,93]. In addition, Sn is the primary diffusion element while Co is essentially immobile [92].

2.3.5. Electroless Co(P) and Co(W,P) Applied to Conductor Metals

Ferromagnetic behaviors of electroless Co(P) films have been widely studied for serving as the magnetic recording materials in past years and the Co-P binary phase diagram is shown in Fig. 2-15 [94]. Chi and Cargill reported the average Co-Co atomic distance increases with increasing P content [95]. In addition, Hüller *et al* pointed out that Co(P) film is mainly amorphous when P contents of electroless Co(P) film are higher than 12 *at.*% [96]. Paunovic *et al.* investigated the feasibility of electroless Co(P) film, which is amorphous and with low resistance, to diffusion barrier of Cu metallization [97]. Hono and Laughlin [98] pointed out the solubility of P in Co is extremely low so that the P atoms would segregate at grain boundaries, thus providing the stuffed-type barrier capability. O'Sullivan *et al* [7] reported that the 50-nm thick Co(P) is an effective diffusion barrier to Cu up to 400°C. Above studies also indicated the P contents affects the crystallinity of electroless Co(P) films and the films transform to nanocrystalline or even to amorphous structure with supersaturated P content. This enables the stuffed-type diffusion barrier capability to Cu up to 400°C when P elements segregate to the grain boundaries of Co(P).

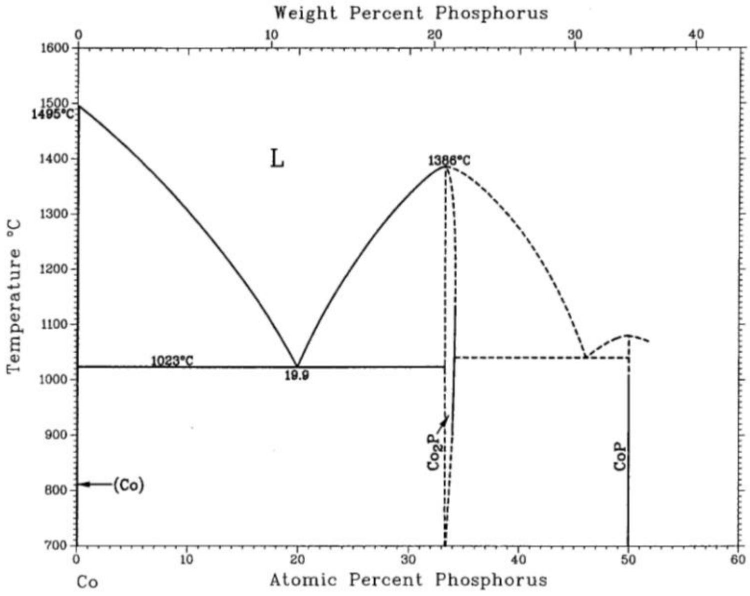

Figure 2-15. Co-P binary phase diagram [94].

Figure 2-16 depicted the Co-W binary phase diagram [94]. The Co-W phase diagram consists of: (1) the liquidus passes through a maximum at 1505°C and 10 *at.*% W; (2) an eutectic point at 1471°C and 21 *at.*% W; (3) a peritectic horizontal at 1689°C, with terminal compositions of 32 and 99.1 *at.*% W; (4) Co_7W_6 with rhombohedral structure forms peritectically at 48.5 *at.*% W; (5) the face-centered cubic (FCC) solid solution, α-Co, with a maximum solid solubility of 17.5 *at.*% W; (6) Co_3W with hexagonal Ni_3Sn structure forms as a result of the peritectoid reaction at 1093°C and 25.3 *at.*% W; and (7) the solid solution W, with a maximum solid solubility of 0.9 *at.*% Co at 1689°C. According to Takayama *et al.*, the solubility limit of W in α-Co decreases from 17.5 *at.*% at 1471°C to 0.5 *at.*% at 750°C [99].

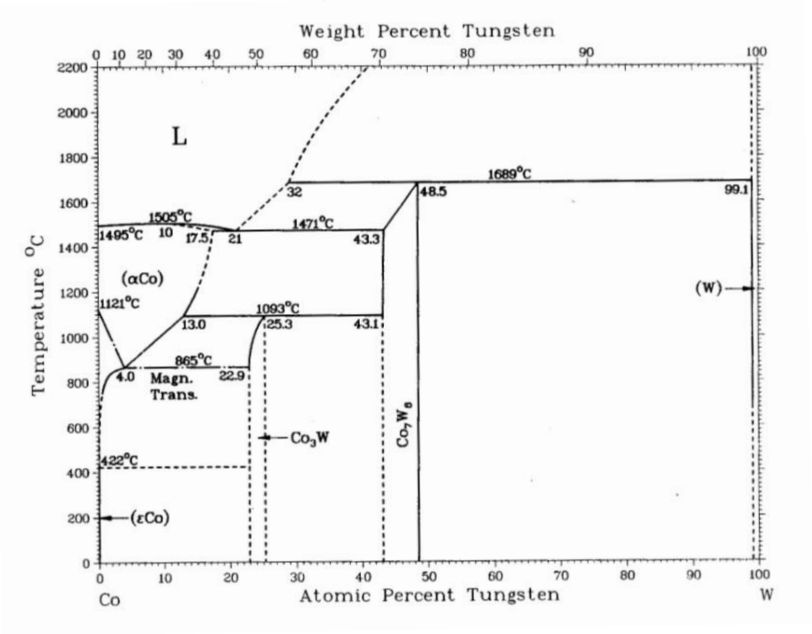

Figure 2-16. Co-W binary phase diagram [94].

Neumeier *et al*. found the solubility of Co in W is about 0.9 *at.*% at the peritectic temperature and is about 0.7 *at.*% at 700°C [100]. Inspired by previous study about the thermal enhancements and the increase of corrosion resistance by adding W atom in Ni(P) thin film, Kohn *et al*. [9-11] investigated the addition of W in Co(P) thin film to improve the diffusion barrier capability. After the 400°C-annealing for 8 hrs, the diffusion barrier capabilities of sputtered Co, electroless Co(P) and electroless Co(W,P) thin films were analyzed by secondary ion mass spectrometer (SIMS) and the results indicated that the electroless Co(W,P) thin film is the best diffusion barrier layer to retarded Cu atom diffusion. In addition, Kohn *et al.* [9] reported that the P and W impurities stabilize the hexagonal closed-packed (HCP) phase, delaying the transition to the FCC phase by more than 80℃ in comparison with pure Co in bulk form. It is also reported that 30-nm-thick Co(W,P) films may effectively inhibit the Cu diffusion after thermal treatments up to 500℃ [10]. In brief, electroless Co(W,P) should be a better diffusion barrier layer than electroless Co(P) does.

2.4. Electroless Deposition

2.4.1. Theory of Electroless Deposition

Electroless plating is a popular method to prepare the diffusion barrier layers. It is a method of depositing a metal on a substrate using a process of chemical reduction in an aqueous solution containing a chemical reducing agent without the electrical energy. The driving force for the reduction of metal ions and their deposition is supplied by the chemical reducing agent in solution, and the driving potential is essentially constant at all points of the surface of the component [101]. The subsequent deposition of metal also serves as the catalytic surface and involves several simultaneous reactions such as oxidation and reduction in an aqueous solution so that the electroless plating is also known as chemical or auto-catalytic plating. The oxidation is characterized as the loss of electrons whereas the reduction is that the gain of electrons. The reaction equations are expressed as follows [102]:

$$R + H_2O \rightarrow O_x + H^+ + e^- \qquad (2\text{-}1)$$

$$M^{n+} + ne^- \rightarrow M^0 \qquad (2\text{-}2a)$$

$$2H^+ + 2e^- \rightarrow H_{2(g)} \qquad (2\text{-}2b)$$

where R is the reducing agent, M^{n+} is the plating metal ion.

At the initial stage of electroless plating, the metal ions (M^{n+}) are selectively reduced only at the surface of a catalytic substrate immersed into an aqueous solution of the metal ions [6]. This is characterized as a metal displacement reaction, and the reaction equations are described as:

$$\mathrm{M}_1^0 \rightarrow \mathrm{M}_1^{n+} + ne^- \qquad (2\text{-}3)$$

$$\mathrm{M}_2^{n+} + ne^- \rightarrow \mathrm{M}_2^0 \qquad (2\text{-}4)$$

With continuous deposition, the deposit catalyzes the reduction reaction and deposits itself on the substrate through the catalytic action, which is the so-called autocatalytic plating [6].

In an electroless plating bath, there are some compositions listed below [6,102,103]:

(1) Metallic salt: the main plating source that provides the metal ions when plating. $NiSO_4$ and $CoSO_4$ are the common metallic salt for the electroless plating in FC technology.

(2) Reducing agent: a substance that brings about the reduction in other substances by itself oxidization. A reducing agent is also called a reductant or reducer. Strong reducing agents easily lose (or donate) electrons. The composition of plating layer could be controlled by using appropriate reducing agent. HCOH, $(CH_3)_2HN \cdot BH_3$(DMAB), $NaBH_4$, and NaH_2PO_2 are widely used as the reducing agents.

(3) Complex agents: a substance capable of forming a complex compound with

another material in solution to control the concentration of metal ions in plating bath and to prevent the insoluble precipitation. Citric acid, sodium citrate, succinic acid, and sodium acetate are common complex agents.

(4) Accelerator: a substance such as sulfide compounds and fluoride compounds that may increase the reaction rate. It also restrains the formation of hydrogen.

(5) Stabilizer: a substance that tends to maintain the chemical properties of the deposition bath, where some catalytic particles are suspended in the bath during electroless plating. The addition of stabilizers in plating bath may cause the absorption of the catalytic particles and stabilize the plating bath. The common stabilizers are sulfide compounds, chloride compounds, thiourea, and heavy metal salts.

(6) Buffer agent: a solution selected or prepared to minimize changes in hydrogen ion concentration of the plating bath so that the stability of plating bath and plating conditions will be maintained.

(7) Brightener: any of the agents which minimizes the deposited particle sizes and level the roughness of the deposition surface to yield smoother or brighter coatings.

(8) pH value conditioner: an agent capable of adjusting the pH values to keep the constant condition. Chemicals such as NaOH and KOH are commonly used.

2.4.2. Electroless Co(W,P)

When depositing Co on a catalytic surface in an aqueous solution with appropriate reacting temperature and pH value by electroless plating using hypophosphite as the reducing agent, electrochemical mechanism, both oxidation and reduction (redox), occurs simultaneously. The oxidation (here is the oxidation of $H_2PO_2^-$ on the catalytic surface) indicates an anodic process, and can be described as [104]:

$$H_2PO^-_{2\,(ads)} + OH^-_{(ads)} \rightarrow H_2PO_3^- + H_{(ads)} + e^- \qquad (2\text{-}5)$$

The electrons and adsorbed hydrogen atoms that are the products of electroless Co deposition in weak alkaline media can react with hydrogen ion from the water

$$H_{(ads)} + e^- + H^+_{(ads)} \rightarrow H_{2(g)} \qquad (2\text{-}6)$$

At the same time, the released electrons take part in the cathodic reactions, which include reductions of Co ions, phosphorus (P), and the co-deposition of W. The cathodic reactions can be presented as follows

$$Co^{2+} + 2H_2PO^{-}_{2\,(ads)} + 2OH^{-} \rightarrow Co^{0} + H_2PO_3^{-} + H_2 \tag{2-7}$$

$$H_2PO^{-}_{2\,(ads)} + e^{-} \rightarrow P\downarrow + 2OH^{-} \tag{2-8}$$

It is known that refractory metal, *e.g.*, Mo and W, can be deposited neither electrochemically nor chemically, but it can be co-deposited with an iron (Fe) group metals such as Fe, Co, and Ni. It exists in the anionic form of MoO_4^{2-} or WO_4^{2-} in a deposition bath and could form an intermediate complex compound with the main metal and complex agent. This complex compound is adsorbed on the electrode surface, and the iron group metal acts as a catalyst for the reduction of W. This co-deposition process may go in parallel with the reduction reaction of the iron group metal in the electrochemical deposition [104]. It has been suggested that intermediate tungsten-citrate complex at the substrate surface dissociates with the formation of WO_2^{2+} and this ion, in turn, is reduced to W [96]. Taking into account all above considerations, the overall W co-deposition reaction can be presented as [104]

$$WO_2^{2+} + 6H_2PO_2^{-} + 4H_2O \rightarrow W + 6H_2PO_3^{-} + 3H_2 + 2H^{+} \tag{2-9}$$

As described above, electroless reactions are influenced by concentrations of all the components and pH value of plating bath. The concentration of ions affects the proportion of all the depositing elements in the deposit, *e.g.*, the proportion of P affects the structure of deposited film directly. Moreover, the pH value affects the reaction rate, element proportions, and structure of film. The forming products are mainly H_2PO_3 and hydrogen ions, which lower the pH value, thus, pH value conditioner is essential to maintain the structure and elements in the deposited film.

2.5. Motivations

UBM is commonly manufactured by PVD methods such as *e*-beam evaporation or sputtering method. Recently, EN layer is applied on UBM manufacture. As mentioned above, electroless plating possesses the advantages such as simple equipments and low material cost, and is benefited by its selective and uniform deposition. Electroless plating hence becomes one of the competitive processes for UBM manufacture in FC-related technologies.

O’Sullivan *et al*. [7] reported a superior barrier capability of Co(P) to inhibit the interdiffusion between Cu and ILD in Cu-IC in comparison with EN. Our previous work confirmed that the electroless Co(P) film might also inhibit interdiffusion between eutectic PbSn solder and Cu [8]. In addition, enhancement of thermal property and diffusion barrier capability by incorporating W in Co(P) has been reported previously [9-11]. This thesis work hence investigated the feasibility of electroless Co(W,P) layer, both amorphous and polycrystalline, as the diffusion barriers to various solders including eutectic PbSn, SnBi, and SAC. The samples were treated by liquid-state aging at 250°C up to 5 hrs and the solid-state aging at 120°C or 150°C for 1000 hrs. Afterward, microstructure and composition characterizations were performed in order to analyze the alloy reactions and morphology evolution at the solder/Co(W,P) interfaces. The values of E_a for IMC growth and shear strength of the PbSn/Co(W,P) and SAC/Co(W,P) systems were also investigated. Analytical results illustrated the good diffusion barrier characteristics of electroless Co(W,P) to various solders and thus are feasible to the UBM for FC bonding.

Chapter 3

Experimental Methods

This work presents a study on the diffusion barrier characteristics of electroless Co(W,P) to PbSn, SnBi and SAC solders. E_a's of IMC growth and bonding strengths are investigated in PbSn/Co(W,P) and SAC/Co(W,P) systems regardless of crystallinities of Co(W,P) layers. Si wafers sequentially coated with 50-nm thick Ti and 100 nm-thick Cu were chosen as the substrate to simulate the Cu interconnects. After pretreatments, about 6-8 μm electroless Co(W,P) layers with various crystallinities were deposited on Cu/Ti/Si substrates. The structure of samples prepared in this study is schematically illustrated in Fig. 3-1. The methods of sample preparation, thermal treatments and microstructure/composition characterizations are described in the following sections.

3.1. Sample Preparation

3.1.1. Substrate Preparation

First, Si wafers were cleaned by RCA process. After forming a thin SiO_2 layer on Si by wet oxidation, the wafers were coated with Ti (50 nm)/Cu (100 nm) layer by *e*-beam evaporation. Ti layer serves as the adhesion layer whereas Cu layer simulates the Cu interconnects. The wafer was cut into pieces for further sample preparation. Before the electroless deposition, the Si/Ti/Cu substrates were cleaned by de-ionized water, acetone, and de-ionized water in sequence to eliminate the contamination.

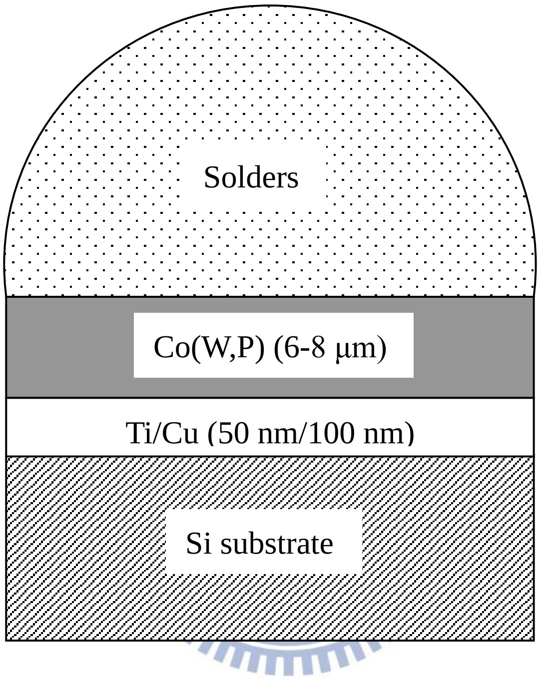

Figure 3-1. Structure of samples prepared in this study.

3.1.2. Pretreatment

Prior to the electroless plating, a pretreatment including roughening, sensitization and activation was performed to obtain a catalytic surface. The chemical formulation of pretreatment is listed in Table 3-1 and the purposes of each step are described as follows [103,105].

(1) Roughening: a treatment to eliminate the oxidation on Cu surface and to enhance

the roughness of substrate surface for improving the adhesion between substrate and deposited layer. With the increase in the substrate roughness, the surface concentration of the adsorbed Sn and Pd ions increases so that the sensitization becomes less essential in this case. Roughening is carried out with 5 *wt.*% H_2SO_4 for 30 sec.

(2) Sensitization: a treatment to escalate the adsorption of Pd ions on the surface. Besides, the sensitization reduces the induction period of the electroless metal deposition reaction, and reduces the size of deposited particles.

(3) Activation: a treatment to form catalytic nuclei for electroless plating thereon before immersing in an electroless bath. The conditions of activation such as pH of palladium chloride (PdCl) solution concentration, temperature, and surface roughness determine whether the sensitization is necessary or not.

Table 3-1. Chemicals and processing conditions of pretreatment.

Step	Component	Concentration	Immersion Time
Roughening	H_2SO_4	5 *wt.*%	30 sec
Sensitization	$SnCl_2 \cdot 2H_2O$ HCl	10 g/L 40 ml/L	5 min
Activation	$PdCl_2 \cdot 2H_2O$ HCl	0.1 g/L 8 ml/L	1 min

The existence of the adsorbed Sn ions on the substrate in sensitization process provides both a greater number of Pd ions on the substrate and a greater bonding strength of Pd ions on the surface. The mechanism of sensitization and activation is known to involve the concept of an equilibrium shift towards formation of complex Pd anions and predominance of the number of Pd ions over Sn ions on the surfaces.

3.1.3. Deposition of Electroless Co(W,P)

Afterward, about 6- to 8-μm thick electroless Co(W,P) layers were deposited on the Cu/Ti/Si substrates. The chemical formulation for electroless plating bath is listed in Table 3-2. During electroless plating, the pH value of plating bath was monitored by a pH meter and adjusted with KOH solution so as to achieve the Co(W,P) layers with desired crystallinities. The amorphous and polycrystalline Co(W,P) films (term as α-Co(W,P) and poly-Co(W,P) hereafter) were separately obtained at pH = 8.6 and 7.6, respectively. The α-Co(W,P) contains about 9 to 10 *at*.% of P and 0.4 to 0.9 *at*.% of W, whereas the poly-Co(W,P) contains about 4 *at*.% of P and 8 *at*.% of W.

Table 3-2. Chemicals and processing conditions of electroless Co(W,P) plating.

Component		Concentration (g/L)
Co Source	$CoSO_4 \cdot 7H_2O$	23
Reducing Agent	$NaH_2PO_2 \cdot H_2O$	18
Complex Agent	Na_3 Citrate	144
Buffer Agent	H_3BO_3	31
W Source	$Na_2WO_4 \cdot 2H_2O$	10
pH value		7.6 or 8.6
Temperature		90°C

After the electroless deposition, appropriate amounts of eutectic PbSn (Shenmao Technology Inc., SH-6309 RMA, Lot No.:7736; T_m = 183°C), SnBi (Shenmao Technology Inc., PF602-P, Lot No.:0802002; T_m = 138°C) and SAC (Sn-3.0 *wt*.% Ag-0.5 *wt*.% Cu, Shenmao Technology Inc., PF606-P, Lot no.:D0806083; T_m = 217 to 219°C) solder pastes were immediately applied on the Co(W,P) and a brief reflow at 250°C for 30 sec in forming gas (95% N_2-10%H_2) was performed to solidify the solder.

3.2. Thermal Treatment Methods

High-temperature storage test is typically used to determine the effect of time and temperature for thermally activated failure mechanisms of electronic devices. During the test, elevated temperatures (accelerated test conditions) are used without the applied electrical bias. JESD22-A103C [106] is the standard for high temperature storage test of electronic devices and it lists 7 test conditions: (a) +125 (–0/+10)°C, (b) +150 (–0/+10) °C, (c) +175 (–0/+10) °C, (d) +200 (–0/+10) °C, (e) +250 (–0/+10) °C, (f) +300 (–0/+10) °C, and (g) +85 (–0/+10) °C as shown in Table 3-3. Test condition should be selected in accord with the applicability of electronic device, material types and physical properties, packaging styles, customer requisitions, *etc*. Note that Condition B listed in Table 3-3 with 1000-hr test duration is most commonly adopted for evaluating the quality and reliability of electronic devices.

Table 3-3. High-temperature storage test conditions [106].

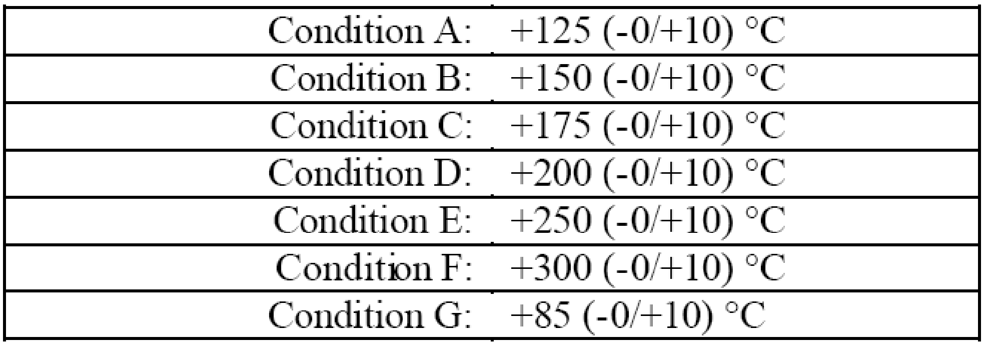

Condition A:	+125 (-0/+10) °C
Condition B:	+150 (-0/+10) °C
Condition C:	+175 (-0/+10) °C
Condition D:	+200 (-0/+10) °C
Condition E:	+250 (-0/+10) °C
Condition F:	+300 (-0/+10) °C
Condition G:	+85 (-0/+10) °C

In order to study the diffusion barrier characteristics and the interfacial reactions of electroless Co(W,P) to PbSn, SnBi and SAC solders, test conditions in JESD22-A103C standard were chosen, *e.g.*, Condition E (liquid-state aging at 250°C) and Condition B (solid-state aging at 150°C) although the JESD22-A103C is primary for testing the electronic devices. Notably, the melting point of SnBi solder is about 138°C, so that the test temperature was reduced to 120°C for solid-state aging test. The E_a of IMC growth and the bonding strength of Co(W,P)/PbSn and Co(W,P)/SAC systems were also evaluated so as to gain an in-depth understanding on the applicability of electroless Co(W,P) as the diffusion barrier layer in UBM structure. The details of the aging tests are described as follows.

3.2.1. Liquid-state Aging

Liquid-state aging test is to study the interfacial reactions between electroless Co(W,P) and liquid solders and the diffusion barrier mechanism of electroless Co(W,P) layer. The testing samples were placed on a hot plate, which is connected to a controller. The temperature of hot plate was set at 250°C, and a glass funnel with two pipes was used as a covering to ensure the testing samples were fully exposed to the forming gas (95% N_2-10%H_2) for up to 5 hrs regardless the solder types in the samples. After annealing, testing samples were quenched to room temperature and encapsulated with Acrylic cold mounting materials, afterwards, the cross-sectional surface of testing samples were grinded and polished for further micro-structural analyses.

3.2.2. Solid-state Aging

Solid-state aging test is to study diffusion barrier characteristics of electroless Co(W,P) layer, the interfacial reactions between solder and electroless Co(W,P), and E_a's of IMC growth of testing samples. Before solid-state aging test, the solder/Co(W,P) samples were encapsulated with Acrylic cold mounting materials, grinded, polished, and observed by SEM to investigated the initial IMC thickness Afterwards, the testing samples were vacuum-sealed and sent to the furnace for solid-state aging test at 120°C or 150°C for up to 1000 hrs. Samples annealed for 50, 200, 500, 800, and 1000 hrs at 120°C or 150°C were encapsulated, grinded, polished, and observed by SEM to investigate the IMC growth rate and the types of IMC phases. For the determination of the E_a's of IMC growth in PbSn/Co(W,P) and SAC/Co(W,P) systems, solid-state aging at 130°C and 170°C for at least 500 hrs were also performed and, for the purpose of comparison, the PbSn/pure Co samples were prepared by applying the PbSn solder paste on pure Co foil and tested at the same aging condition.

3.3. Ball Shear Test

As to samples for ball shear test, an array of circular bond pad pattern with 200 μm in diameter was formed on the substrates deposited with α-Co(W,P) or poly-Co(W,P) by the photolithography process using an SU-8 permanent photoresist (supplier: MicroChem Corp.; 5%-weight-loss thermal decomposition temperature = 279°C in air) as the mask layer. After attaching the 300-μm-diameter PbSn or SAC solder balls on the pads, a reflow treatment in forming gas (95% N_2-10%H_2) at 250°C for 1, 10, 20, 30 and 60 min was then carried out to form the solder ball joints. The shear test was performed in accord with the JSDEC Standard, JESD22-B117A [107], by using a Dage 4000 multipurpose bond tester supported by Schmidt Scientific

Taiwan Ltd. at Hsinchu, Taiwan, R.O.C. The shear tool standoff = 30 μm above the sample surface and shear speed = 100 μm/sec. The average shear force was deduced from the test results of at least 25 bumps for each sample preparation condition. According to the shear tests, the influence of P and W contents on the bonding joint strength was also investigated.

3.4. Microstructure and Composition Characterizations

3.4.1. Scanning Electron Microscopy (SEM)

After polishing, the testing samples were taken out from Acrylic cold mounting materials and fixed on a sample holder. Afterwards, samples were etched by etchant solution (98% methyl alcohol and 2% HCl) and coated with a thin Pt layer by Pt coater immediately to prevent from oxidation. The cross-sectional views of the samples were examined by the SEM (Jeol JSM-6500F or Hitachi S-4700) operated at 10 or 15 kV within the secondary electron image (SEI) mode so that high-resolution surface morphology can be obtained. Backscattered electron image (BEI) SEM analysis was performed for distinguishing the differences in atomic types involved in the sample. It was done on the samples with relatively smooth surfaces so that the etching and Pt coating can be omitted.

3.4.2. Composition Analysis

SEM analyses in conjunction with Energy Dispersive Spectrometer (EDS, Oxford Inca Energy 7557 or Genesis) and line scanning analyses were adopted to examine the microstructure and composition changes in the samples. IMCs were tested with at least 10 spots to ensure the phases. The computer’s Dead Time (DT) is set to run between 30% and 40% of the X-ray capture time to obtain the optimum EDS signal for EDS line scan analysis.

3.4.3. Transmission Electron Microscopy (TEM)

The cross-sectional views of the samples were examined by TEM (Philips Tecnai F-20) operated at 200 kV. Since the SEM samples mentioned above were prepared, the interfacial portions of the samples were cut by using the focused-ion-beam (FIB, FEI-201) as the cross-sectional TEM (XTEM) samples and were put on TEM copper grid for TEM analyses. The FIB and TEM were supported by Materials Analysis Technology, Inc. at Chupei, Taiwan, R.O.C.

3.4.4. X-ray Diffraction

The crystal structures of electroless Co(W,P) films were characterized with an *x*-ray diffractometer (XRD, M18 XHF, MacScience) operated at 200 mA and 50 kV.

The *x*-ray source was Cu-K_α radiation (λ = 0.154 nm) and the signal scanning rate was 4°/min.

Chapter 4

Results and Discussion

Electroless Co(W,P) to PbSn Solder

4.1.1. PbSn/α-Co(W,P) Samples

4.1.1.1. Liquid-state Aging for Long Times

Figures 4-1(a)-(f) present the cross-sectional SEM micrographs of PbSn/α-Co(W,P) couples subjected to liquid-state aging for as-reflow, 20 min, 30 min, 1 hr, 3 hrs and 5 hrs, respectively. We note the prolonged liquid-state aging is for examining a complete microstructure evolution in such sample types. As shown in Fig. 4-1(a), granular $CoSn_2$ intermetallic compound (IMC) coated with $CoSn_3$ by the peritectic reaction [12] or $CoSn_3$ IMCs emerged at the solder/Co(W,P) interface at the early stage of aging. Voids were occasionally observed and they might be caused by the evaporation of organic additives in the solder paste. In the sample subjected to 20-min aging, the IMCs coarsen and detachment of IMCs away from the reacting interface occurs as shown in Fig. 4-1(b). In addition, an about 1-μm thick continuous layer neighboring to unreacted Co(W,P) can be observed and the EDS analysis reveals it contains about 20 at.% of P and about 2.3 at.% of W. As a result of the accumulation of P elements at the reacting interface, such a P-rich layer is in fact a mixture of

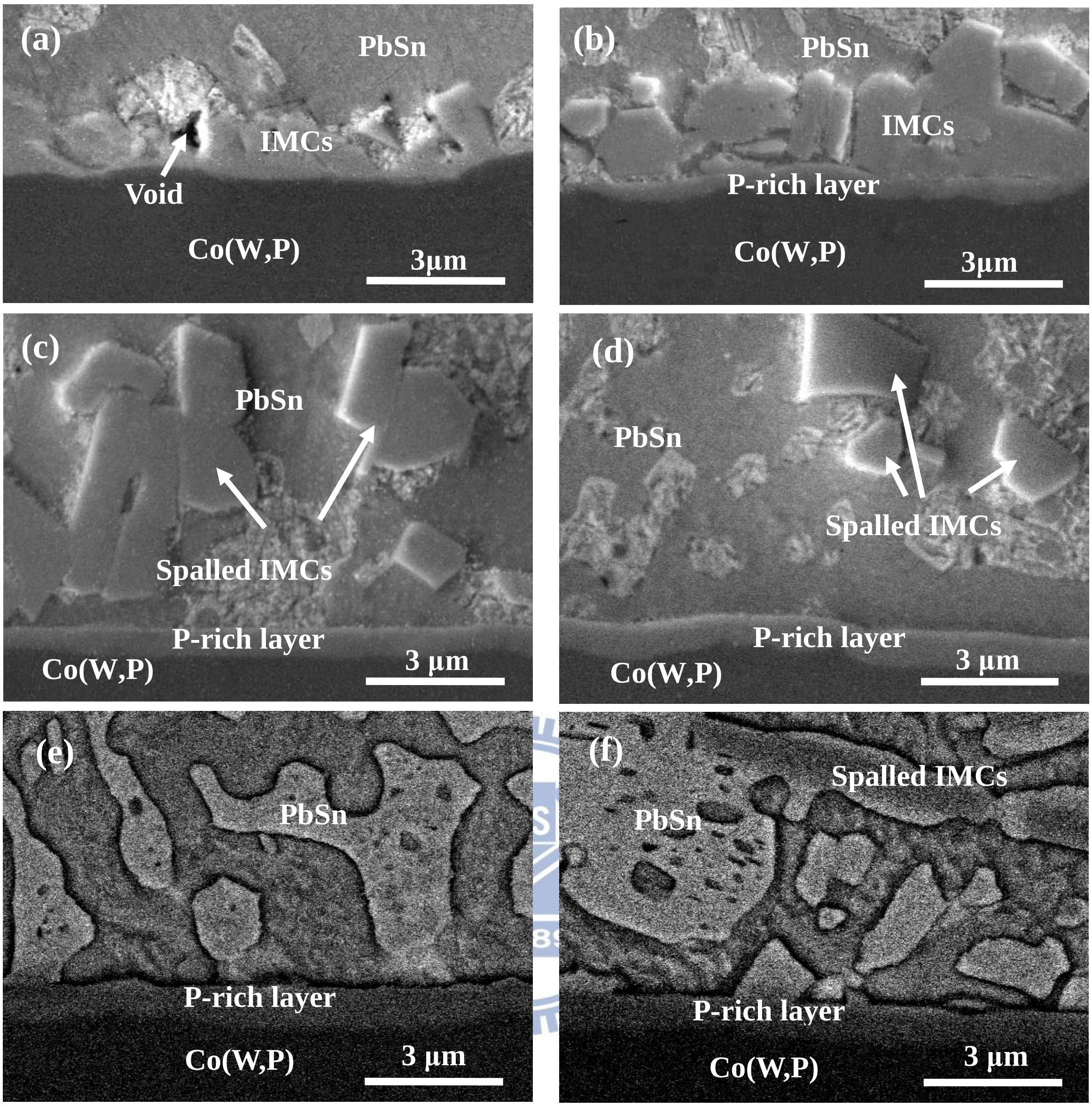

Figure 4-1. Cross-sectional SEM micrographs of PbSn/α-Co(W,P) samples subjected to liquid-state aging at 250°C for (a) 1 min, (b) 20 min, (c) 30 min, (d) 1 hr, (e) 3 hrs and (f) 5 hrs. (SEI mode; accelerating voltage = 10 kV)

nano-scale IMCs as reported as mentioned in previous study [12]. The spallation of IMCs became rather obvious after the aging for 30 min as shown in Fig. 4-1(c) and nearly all IMCs spalled into solder after 1-hr aging as depicted by Fig. 4-1(d). The

SEM images shown in Figs. 4-1(e) and 4-1(f) indicate that there is no dramatic change in interfacial morphology in the samples subjected to prolonged aging in which the thickness of P-rich layer remains the same at about 1 μm. The IMC spallation from PbSn/Co(W,P) interface into solder during prolonged liquid-state aging is ascribed to the P accumulation which reduces the adhesion the IMCs.

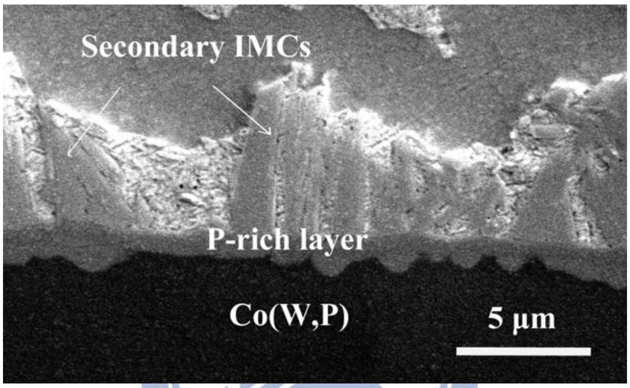

Figure 4-2. Cross-sectional SEM micrograph of PbSn/α-Co(W,P) sample subjected to 250°C/30-min liquid-state aging followed by 150°C/200-hr solid-state aging. (SEI mode; accelerating voltage = 15 kV)

Above results seem to indicate that the formation of continuous P-rich layer may deter subsequent Co-Sn reactions. In order to verify this phenomenon, a 250°C/30-min aged sample was further aged at 150°C for 200 hrs. As shown in Fig. 4-2, the growth of secondary IMCs from the P-rich layer into solder was observed.

A supply of Co and Sn elements would be required for forming such bush-like

IMCs, implying the P-rich layer cannot block the Co-Sn interdiffusion and the IMC spallation is in fact an unceasing process at the reacting interface during liquid-state aging. This also indicates the P accumulation at the reacting interface plays a key role in the evolution of interfacial morphology. When the P content at reacting interface remains low at the early stage of aging, the IMCs form and coarsen accordingly at the solder/Co(W,P) interface. With the increase of aging time, a continuous P-rich layer forms and the sufficiently high amount of P deteriorates the adherence of IMCs to P-rich layer and consequently leads to the IMC spallation. During the prolonged aging, the Sn elements continuously diffuse across the P-rich layer to react with Co to form the IMCs at the interface neighboring to Co(W,P) while the IMCs neighboring to the molten solder unceasingly spall away. In the meantime, the highly accumulated P elements interrupts the coarsening of IMCs and results in an ultrafine IMC mixture in the P-rich layer as mentioned in previous study [12]. Since the spallation of nano-scale IMCs could not be visibly detected by SEM in an *in-situ* manner, a reacting interface containing the P-rich layer with fixed thickness was hence observed in the samples subjected to prolonged aging.

4.1.1.2. Solid-state Aging

Analytical results regarding to the PbSn/α-Co(W,P) subject to solids-state aging have been reported in detail previously [12]. In conjunction with the results of liquid-state aging presented above, the formation of IMCs apparently implies the sacrificial-type barrier feature of α-Co(W,P) to eutectic PbSn solder. Further, our previous TEM characterization revealed a finely dispersed Co_2P precipitates in the α-Co(W,P) layer and the electroless layer tends to recrystallize during the aging treatment [12]. The formation of phosphide compounds and supersaturated P elements in α-Co(W,P) may block the diffusion of Cu into Co and, hence, the α-Co(W,P) may also possess the stuffed-type barrier capability since EDS has revealed a negligible interdiffusion between Co and underlying Cu layer. The α-Co(W,P) is hence a combined-type, *i.e.*, sacrificial- plus stuffed-type, diffusion barrier to PbSn solder.

4.1.2. PbSn/poly-Co(W,P) Samples

4.1.2.1. Liquid-state Aging

Figure 4-3(a) depicts the cross-sectional SEM image of PbSn/poly-Co(W,P) sample subjected to liquid-state aging for 1 hr and the corresponding EDS line scanning profiles is shown in Fig. 4-3(b). Unlike the sample containing α-Co(W,P), about 5-μm thick, scallop-type $CoSn_3$ IMCs form at the solder/poly-Co(W,P) interface without spallation. In addition, the XTEM/EDS analysis of PbSn/poly-Co(W,P) sample revealed an about 500-nm thick, amorphous layer with relatively high W

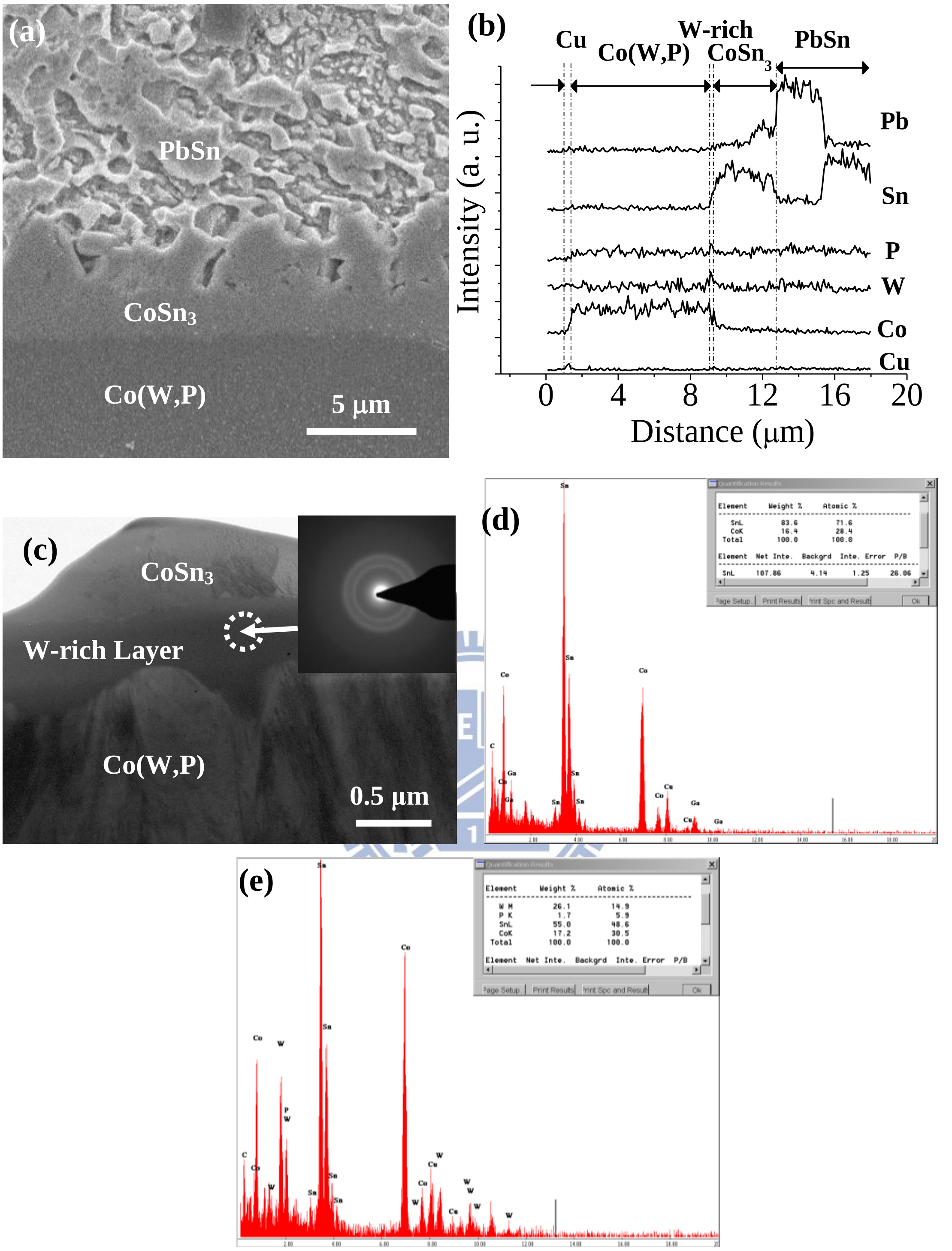

```
Element     Weight %     Atomic %
-------------------------------------------
   SnL         83.6         71.6
   CoK         16.4         28.4
 Total        100.0        100.0

Element  Net Inte.  Backgrd  Inte. Error  P/B
----------------------------------------------
 SnL     107.86       4.14       1.25     26.06
```

```
Element     Weight %     Atomic %
-------------------------------------------
   W M         26.1         14.9
   P K          1.7          5.9
   SnL         55.0         48.6
   CoK         17.2         30.5
 Total        100.0        100.0

Element  Net Inte.  Backgrd  Inte. Error  P/B
```

Figure 4-3. (a) Cross-sectional SEM micrograph of PbSn/poly-Co(W,P) sample subjected to 250°C /1-hr liquid-state aging and (b) corresponding EDS line scanning profiles. (SEI mode; accelerating voltage = 15 kV). (c) XTEM micrograph of the PbSn/poly-Co(W,P) sample subjected to

250°C/1-hr liquid-state aging. The dotted circle denotes the area where the selected area electron diffraction (SAED) pattern was taken. (d) TEM/EDS spectrum of $CoSn_3$ in (c). (e) TEM/EDS spectrum of W-rich layer in (c).

content (about 15 *at*.%) emerging in between the $CoSn_3$ IMCs and unreacted Co(W,P) as shown in Fig. 4-3(c). Since the W content is high in comparison with that in previous α-Co(W,P) system, we hence term it as the W-rich layer. Similar to the accumulation of P, the W-rich layer should result from the accumulation of W at the interface when Co reacts with Sn to form the IMCs due to the low solubility of W elements in the samples.

Since the amorphism has been categorized as a plausible barrier mechanism [29], a liquid-state aging up to 5 hrs was hence performed to verify whether the W-rich layer may retard subsequent interdiffusion. Nevertheless, the IMC layer was found to thicken to about 7 μm after the 5-hr aging in the presence of such an amorphous layer. Hence the barrier capability should ascribe to the nature of chemical bonds [108], rather than to the structure amorphism as proposed by previous classification scheme [29]. The decoupling of structure amorphism with the barrier capability will be discussed in Section 4.2 [85].

4.1.2.2. Solid-state Aging

Figures 4-4(a) and 4-4(b) separately present the cross-sectional SEM images of PbSn/poly-Co(W,P) samples subjected to solid-state aging for 1000 hrs and the corresponding EDS line scanning profiles. An about 3 μm in thickness, layer-like IMC formed at the solder/poly-Co(W,P) interface and, according to EDS analysis, it is mainly the $CoSn_3$ type. The formation of IMCs iterates the sacrificial type barrier feature of poly-Co(W,P) sample.

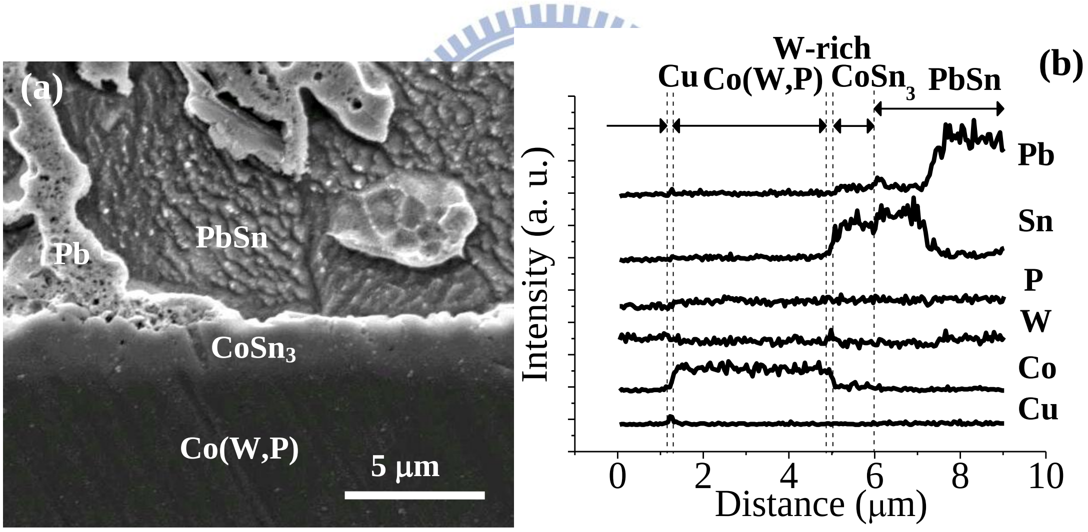

Figure 4-4. (a) Cross-sectional SEM micrograph of PbSn/poly-Co(W,P) sample subjected to 150°C/1000-hr solid-state aging and (b) corresponding EDS line scanning profiles. (SEI mode, accelerating voltage = 15 kV)

XTEM images of the 150°C/1000-hr aged sample are presented in Figs. 4-5(a) and 4-5(b). An about 250-nm thick amorphous W-rich layer (W content ~ 10 *at.*%) in between IMCs and unreacted Co(W,P) was similarly observed. The thinner W-rich layer in such a sample is attributed to the lower temperature of solid-state aging.

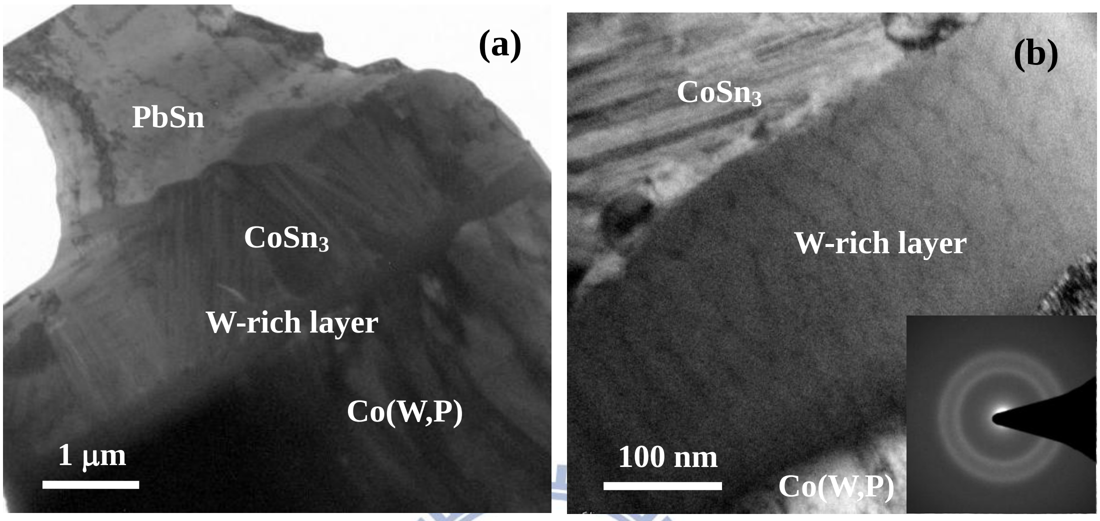

Figure 4-5. (a) XTEM micrograph of PbSn/poly-Co(W,P) sample subjected to 150°C/1000-hr solid-state aging. (b) Enlarged picture of W-rich layer and corresponding SAED pattern.

We note that TEM and EDS analyses detect negligible amount of Co_2P precipitates and/or the Co-W alloy phase in unreacted poly-Co(W,P) and the presence of grain boundaries in poly-Co(W,P) might serve as the fast diffusion paths. Although supersaturated P and W contents are present in poly-Co(W,P), their effects on stuffed-type barrier seem comparatively less than those in α-Co(W,P). Besides, subsequent kinetic analysis indicated the poly-Co(W,P) exhibits a lower E_a of IMC growth. This weakens the stuffed-type barrier capability in poly-Co(W,P) and, hence, the poly-Co(W,P) is termed mainly as a sacrificial-type barrier.

4.1.3. Determination of E_a of IMC Growth

Figure 4-6 presents the thickness consumption of Co(W,P) layer against the square root of aging time in the samples containing various electroless Co(W,P) layers deduced from the SEM characterizations. It can be readily seen that at the same aging time span, less amount of α-Co(W,P) is consumed regardless of the aging type. This indicates the α-Co(W,P) possesses a better barrier capability in terms of its sacrificial behavior. It is believed that the barrier capability of α-Co(W,P) layer is enhanced by its high P content which may block the interdiffusion in a more efficient manner in comparison with that in poly-Co(W,P) sample.

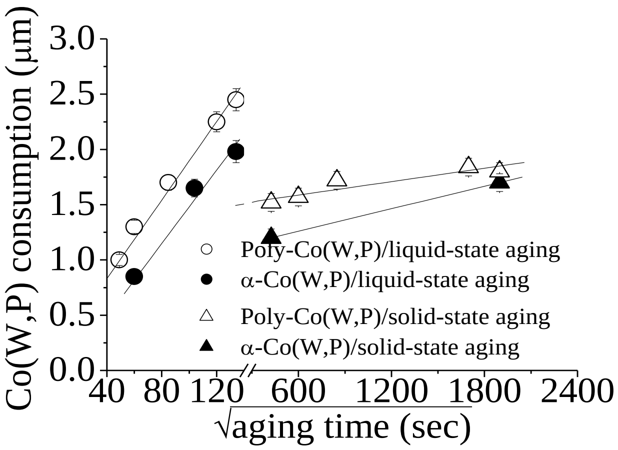

Figure 4-6. Consumption of Co(W,P) layer as a function of square root of aging time in the samples containing various electroless Co(W,P) layers.

Figure 4-6 also reveals that the consumptions of α-Co(W,P) and poly-Co(W,P) layers subjected to 1-hr liquid-state aging are about 1.98 and 2.45 μm, respectively, whereas the consumptions of α-Co(W,P) and poly-Co(W,P) layer subjected to 1000-hr solid-state aging are about 1.7 and 1.84 μm, respectively. Analytical results presented above hence indicates, regardless its crystallinity, about 2 μm-thick electroless Co(W,P) layer is required for UBM applied to FC bonding utilizing eutectic PbSn solder joints.

PbSn/α-Co(W,P) and PbSn/poly-Co(W,P) samples aged at 130-170℃ up to 500 hrs were carried out to determine the E_a of IMC growth. For the purpose of comparison, PbSn/pure Co samples were also investigated. As indicated by the plot of IMC thickness as a function of square root of aging time in Fig. 4-7(a), the linear profiles reveal the diffusion-controlled IMC growth in the time span of investigation. It is well known that the thickness-time relation can be expressed as [109-111]

$$x = \sqrt{Kt} \tag{4-6}$$

where x = total thickness of IMC layer, t = aging time duration and K = constant correlating to the diffusional growth of IMC. The values of K can be determined from the slopes of plots presented in Fig. 4-7(a) by employing the Arrhenius form:

$$K = A\exp\left(-\frac{E_a}{kT}\right) \tag{4-7}$$

where A = constant, k = Boltzmann's constant and T = absolute temperature.

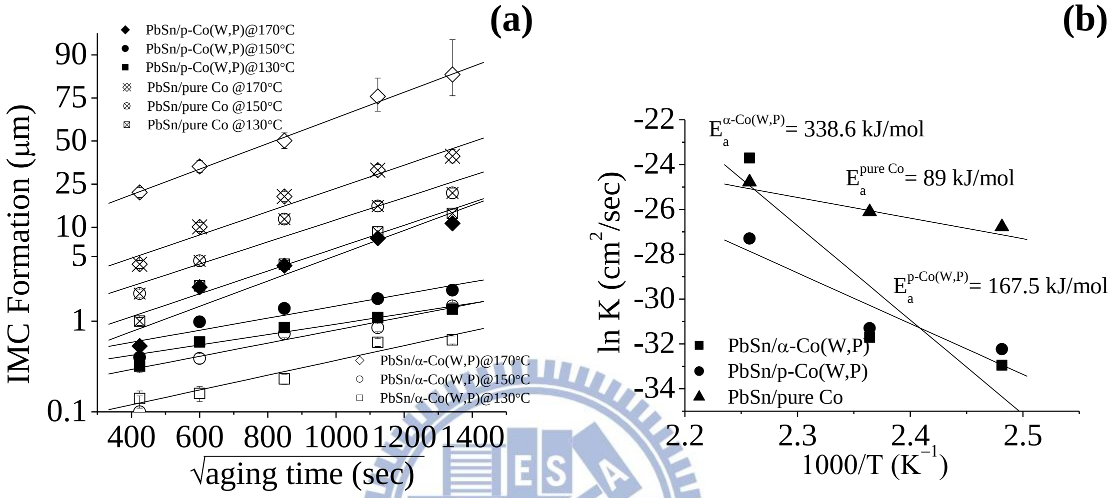

Figure 4-7. (a) IMC thickness against the square root of aging time for various PbSn/Co samples subjected to solid-state aging at 130-170℃ up to 500 hrs. (b) Plots of ln$K$ versus 1/T for the determination of the values of E_a for IMC growth.

According to the ln$K$ *versus* 1/T plot shown in Fig. 4-7(b), the values of E_a are found to be 338.6, 167.5, and 89 kJ/mole for electroless α-Co(W,P), electroless poly-Co(W,P) and pure Co, respectively. The highest value of E_a for α-Co(W,P) illustrates the best barrier efficiency, in agreement with the slowest Co thickness consumption and the enhancement of barrier capability due to its high P and W contents in such an electroless layer.

4.1.4. Ball Shear Test

Ball shear tests were carried out to evaluate the mechanical performance of PbSn/Co(W,P) joints subjected to liquid-state aging at various times and the average bonding strength is presented in Fig. 4-8. The test results reported by previous studies regarding of the PbSn/Ni(P) systems [112-113] were also added in Fig. 4-8 for the purpose of comparison. Figure 4-8 indicates the electroless Co(W,P) layers provide a higher bonding strength in comparison with the PbSn/Ni(P) systems. The shear strength of PbSn/α-Co(W,P) sample increases from 95 MPa at as-reflow condition to a peak value of 119 MPa when aged time is increased to 10 min. The shear strength decreases slightly to 111 MPa in 20-min aged sample and remains a constant value after 60-min aging. The suppression of bonding strength has been ascribed to the IMC spallation [114-115]. However, according to the failure mode characterization presented below, the decrease of shear strength in PbSn/α-Co(W,P) sample might be correlated to the high P content in electroless layer which suppresses the adhesion strength on underlying Cu layer. On the other hand, the PbSn/poly-Co(W,P) sample exhibits a better mechanical performance that the shear strength increases from 95.7 MPa at as-reflow condition to 132.8 MPa after 1-hr aging. Yoon *et al*. [116] and

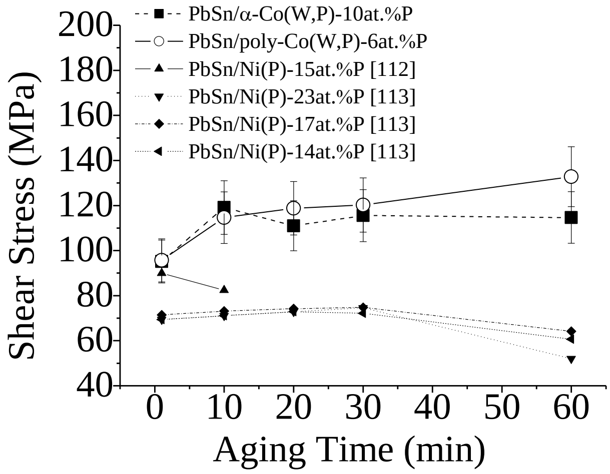

Figure 4-8. Shear stresses of PbSn/α-Co(W,P) and PbSn/poly-Co(W,P) samples subjected to liquid-stage aging for various times.

Sharif and Chan [117] also reported the persistence of bonding strength in the Sn-Zn solder/Ni(P) system subjected to 1-hr reflow. Such a phenomenon has been ascribed to the sagging of solder due to the weight, resulting in a larger contact area and thus a higher shear force after prolonged reflow [117]. Islam *et al*. proposed the increment of bonding strength is resulted from the strengthening of solder due to the homogenization during the reflow [118]. Notably, poly-Co(W,P) layer possesses a lower P content in comparison with α-Co(W,P) and there is no IMC spallation in such a system as shown in Fig. 4-3. The adverse effect due to the P accumulation is expected to be less in SAC/poly-Co(W,P) system so that a higher interfacial bonding strength is observed.

Failure modes for PbSn/α-Co(W,P) and PbSn/poly-Co(W,P) samples identified in terms of the SEM characterizations and the JEDEC22-B117A Standard [107] are separately presented in Figs. 4-9(a) and 4-9(b). In as-reflow sample, ductile mode (mode #1), *i.e.*, failure in solder bulk regardless of the existence of dimple failures [107,119], was observed in more than 40% of 25-tested PbSn/α-Co(W,P) and about 60% of 25-tested PbSn/poly-Co(W,P) samples.

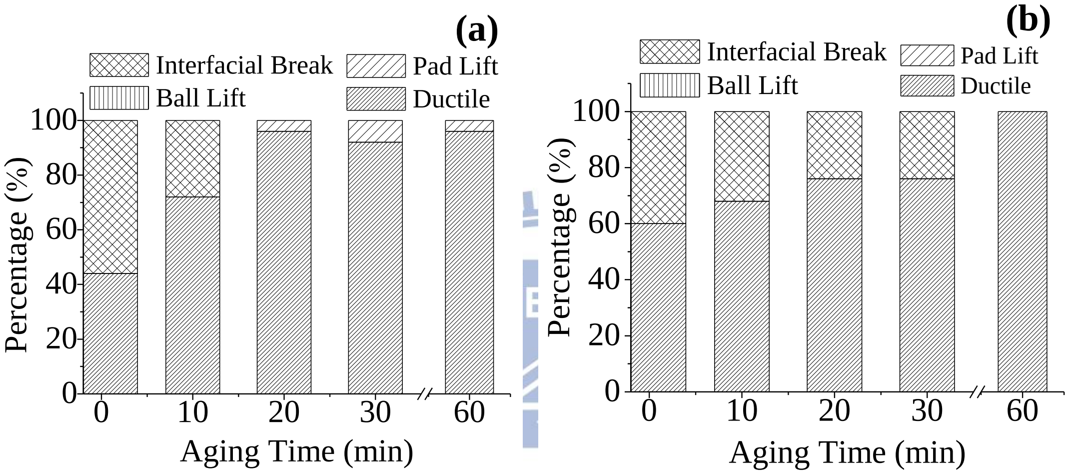

Figure 4-9. Summary of failure modes for (a) PbSn/α-Co(W,P) samples and (b) PbSn/poly-Co(W,P) samples.

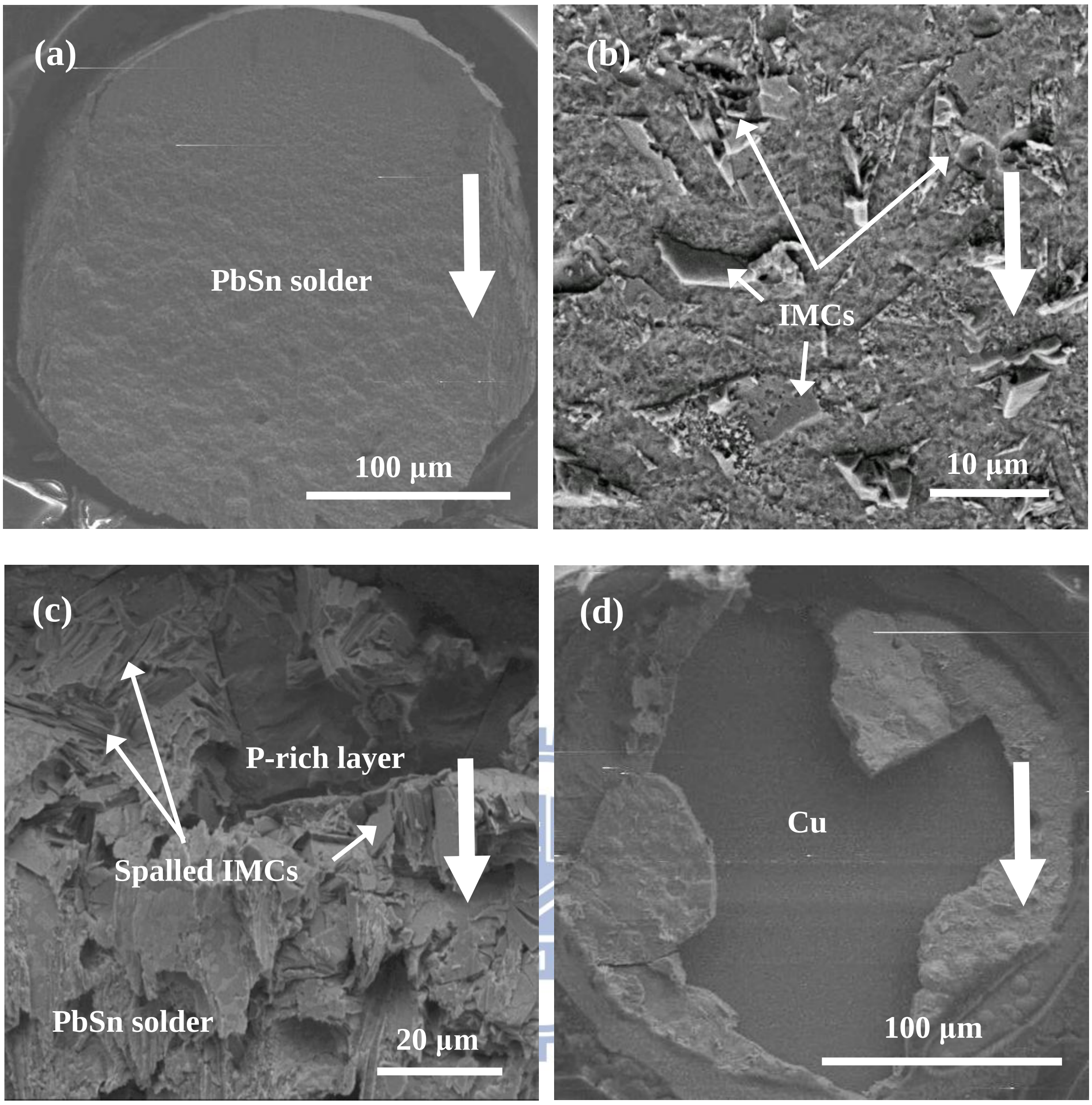

Figure 4-10. (a) Ductile failure in a PbSn/poly-Co(W,P) sample, (b) interfacial break in an as-reflow PbSn/poly-Co(W,P) sample, (c) ductile failure in PbSn/α-Co(W,P) sample subjected to 20-min aging and (d) pad lift in a PbSn/α-Co(W,P) sample subjected to 30-min aging. The arrow in each micrograph indicates the shear direction. (SEI mode; accelerating voltage = 15 kV)

A representative SEM image of ductile failure is shown in Fig. 4-10(a). Failure at solder/IMC interfaces, *i.e.*, the interfacial break (mode #4), was observed in the rest of as-reflow PbSn/α-Co(W,P) and PbSn/poly-Co(W,P) samples in which the exposure of IMC debris was observed in the fracture surface as shown in Fig. 4-10(b). The percentage of ductile failure mode increased with the increase of aging time in both samples, indicating a gradual completion of alloy interactions and thus an improvement of bonding strength in between solder and Co(W,P) layer. Dominance of ductile failure also indicated the interactions of PbSn and Co are fairly strong that it ensures the occurrence of fracture mainly in the bulk of solder. We note the ductile failure in PbSn/α-Co(W,P) sample subjected to prolonged aging is somewhat different from that observed in PbSn/poly-Co(W,P) samples. As shown by a SEM image of PbSn/α-Co(W,P) sample subjected to 20-min aging in Fig. 4-10(c), relatively flat areas with irregular peripheries was occasionally observed in the fracture surfaces. Solder dewetting might occur on the high-P-content surface and consequently weaken the bonding force of solder bump.

The fracture might initiate at the solder/P-rich layer interface and thus cause the exposure of flat P-rich layer surfaces when solder ball was removed. Degradation of solderability due to the accumulation of P elements in EN layer has been reported previously [120] and it might also be a cause of bonding strength decrement in

PbSn/α-Co(W,P) sample subjected to prolonged aging as shown in Fig. 4-8. Furthermore, pad lift (mode #2) failure emerged in PbSn/α-Co(W,P) sample aged for more than 20 min. A representative fracture surface morphology is presented in Fig. 4-10(d). This implies that the high P content in α-Co(W,P) might degrade its adherence on Cu underlayer. In addition, the presence of Co_2P precipitates might harden the α-Co(W,P) layer and thus it could not accommodate the thermal stress induced by the glassy transition of Co(W,P) layer which underwent a recrystallization during aging. This caused a breakage of Co(W,P) layer and, hence, the pad lift failure as illustrated in Fig. 4-10(d).

4.2. Electroless Co(W,P) to SnBi Solder

4.2.1. SnBi/α-Co (W,P) Samples

4.2.1.1. Liquid-state Aging

Figures 4-11(a)-(d) depict the cross-sectional SEM micrographs of SnBi/α-Co(W,P) samples subjected to liquid-state aging for 1 min, 20 min, 30 min, and 1 hr, respectively. At the beginning of heat treatment (Fig. 4-11(a)), thin lath-like Co-Sn IMCs grew out from the SnBi/Co(W,P) interface into the solder whereas isolated reaction zones formed in Co(W,P) region. As the aging times increased, the IMCs coarsened to thick platelets and the isolated reaction zones coalescenced to a continuous reaction layer as illustrated in Fig. 4-11(b). In the meantime, the IMCs partially spalled away from the reacting interface. After a 30-min liquid-state aging, most IMCs spalled into the solder and an approximately 500-nm thick reacting layer formed in between solder and Co(W,P) as shown in Fig. 4-11(c). As shown in Fig. 4-11(d), almost all the IMCs spalled away from the reaction interface when aging times were extended to 1 hr. The IMC spallation from SnBi/Co(W,P) interface into solder is similarly ascribed to the P accumulation which reduces the adhesion of IMCs. Formation of IMCs revealed by SEM analysis indicated that an α-Co(W,P) film is a sacrificial-type barrier to SnBi solder, so it is important that the Co(W,P) layer must be sufficiently thick to prevent complete dissolution into the SnBi solder.

EDS analysis indicated that the Co:Sn ratio in the lath-like IMCs is about 1:3 to 1:4. Furthermore, about 3-4 *at*.% Bi was frequently detected in the IMCs as shown in Fig. 4-11(e). In considering the inaccuracy of EDS spatial detection, the IMCs are most likely a $CoSn_3$ type doped with a small amount of Bi since Bi is partially soluble in Sn-rich alloy [39]. The reacting layer in between the solder and the Co(W,P) was found (by EDS) to comprise of various elements, *e.g.*, Co, Sn, P, W, and Bi, with P content as high as 15 *at*.% and W content about 2.25 *at*.% (see Fig. 4-11(f)). The increased P and W contents were ascribed to the accumulation of P and W elements at the reaction interface when Co was consumed by Sn to form the $CoSn_3$ IMCs. Owing to its high P content, the reaction layer is hereafter termed as a P-rich layer as discussed in Section 4.1.1.

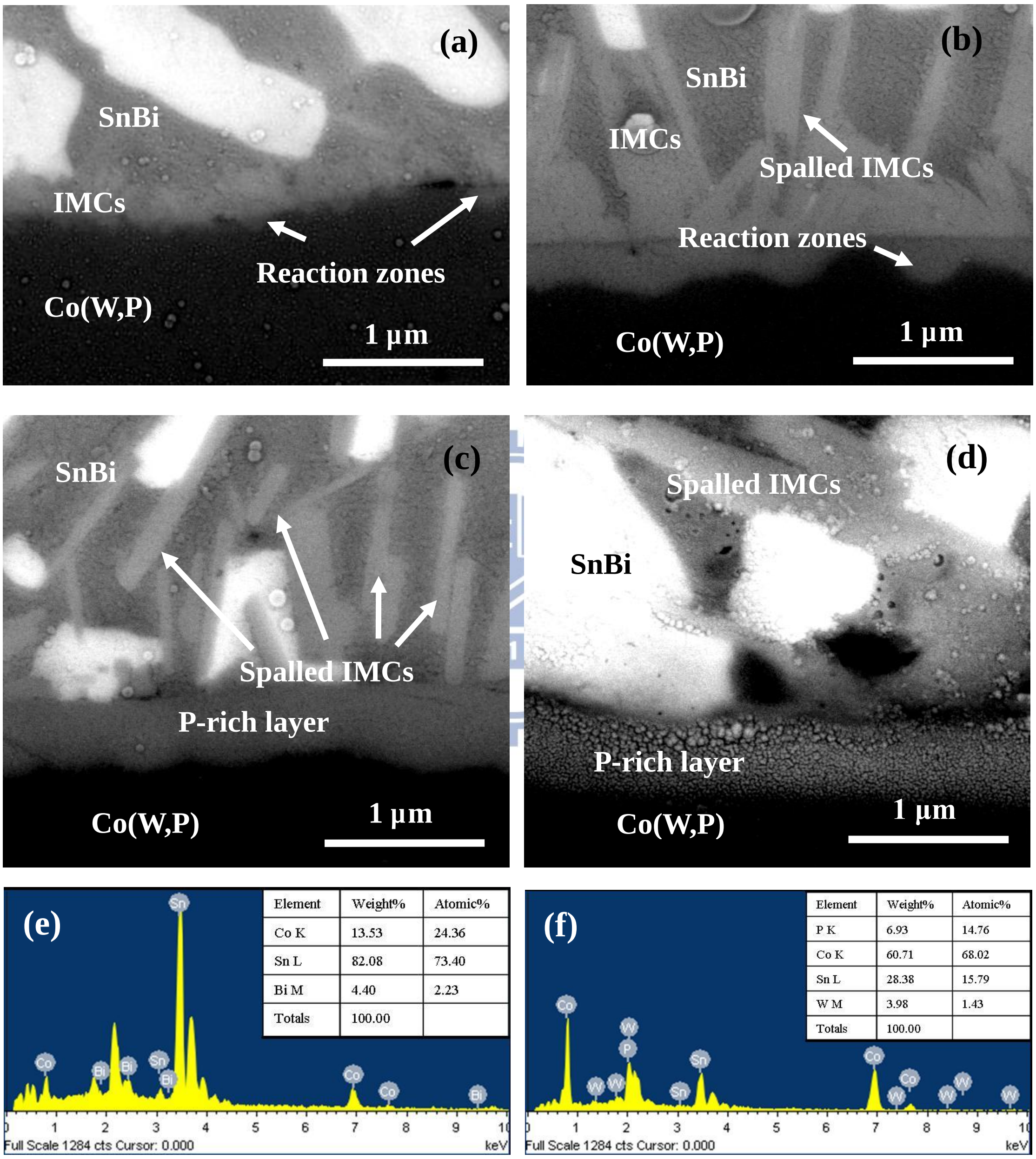

Element	Weight%	Atomic%
Co K	13.53	24.36
Sn L	82.08	73.40
Bi M	4.40	2.23
Totals	100.00	

Element	Weight%	Atomic%
P K	6.93	14.76
Co K	60.71	68.02
Sn L	28.38	15.79
W M	3.98	1.43
Totals	100.00	

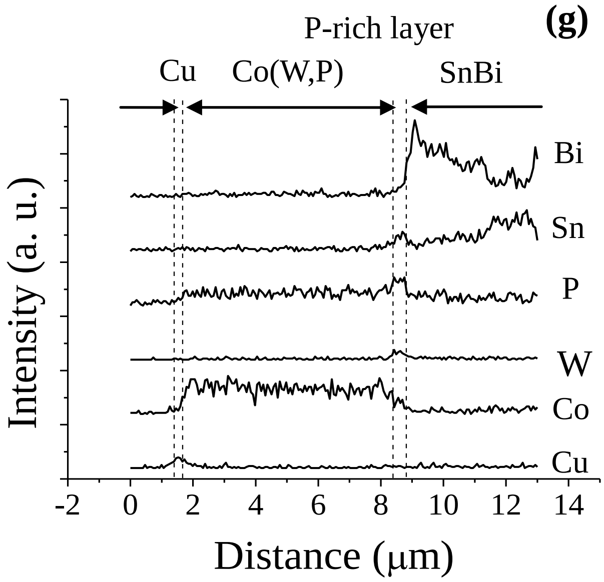

Figure 4-11. SEM micrographs of SnBi/α-Co(W,P) samples subjected to liquid-state aging for (a) 1 min, (b) 20 min, (c) 30 min and (d) 1 hr. (e) SEM/EDS spectrum of IMC, and (f) SEM/EDS spectrum of P-rich layer. (g) EDS line scan profiles corresponding to the sample shown in (d). (BEI mode; accelerating voltage = 15 kV)

Figure 4-11(g) depicts the EDS line scan profiles for the 1-hr aged samples as shown in Fig. 4-11(d). In conjunction with the TEM analysis presented below, the absence of Cu and Sn signals in the unreacted Co(W,P) implies that Co(W,P) may also serve as a stuffed-type diffusion barrier to the underlying Cu layer due to the supersaturated P elements as well as the fine Co_2P IMCs dispersed in Co(W,P). Hence, α-Co(W,P) is a mixed-type barrier applied to joints containing the SnBi solder, similar to the PbSn/α-Co(W,P) samples subjected to liquid-state aging reported previously.

Previous SEM characterization revealed that the P-rich layer seems not thickening significantly after 30-min aging. To verify this, we performed the liquid-state aging for 5 hrs and the corresponding SEM images are presented in Figs. 4-12(a) and 4-12(b). It can be seen that the thickness of P-rich layer remains unchanged after prolonged aging. Figure 4-12(c) summarizes the thicknesses of the P-rich layer and the consumed Co(W,P) as a function of the square root of time.

Although the P-rich layer did not thicken during the prolonged aging, there was no ceasing of Co(W,P) consumption. The plot shown in Fig. 4-12(c) reveals that this layer does not inhibit further alloy reactions. Subsequent TEM analysis found that the P-rich layer is a polycrystalline layer comprised of nano-scale IMCs. It is, therefore, concluded that the fine IMCs continuously detach from the P-rich interfacial layer into the molten solder while the IMCs unceasingly form as the Sn elements diffuse through the P-rich layer to react with Co(W,P).

XTEM analysis was carried out in order to explore the microstructure and composition changes at the SnBi/Co(W,P) interface and the analytical results for the sample subjected to 1-hr liquid-state aging is presented in Fig. 4-13. The polycrystalline feature of the P-rich layer was identified by the attached selected area electron diffraction (SAED) pattern which revealed various IMC types, *e.g.*, Co_3Sn_2, CoSn, CoP and SnP_3. Furthermore, the absence of a distinctive granular contrast in the P-rich layer implied extremely small IMC sizes. It is believed that the accumulated P and W elements inhibit grain coarsening during IMC formation and result in the fine IMC mixture in the P-rich layer.

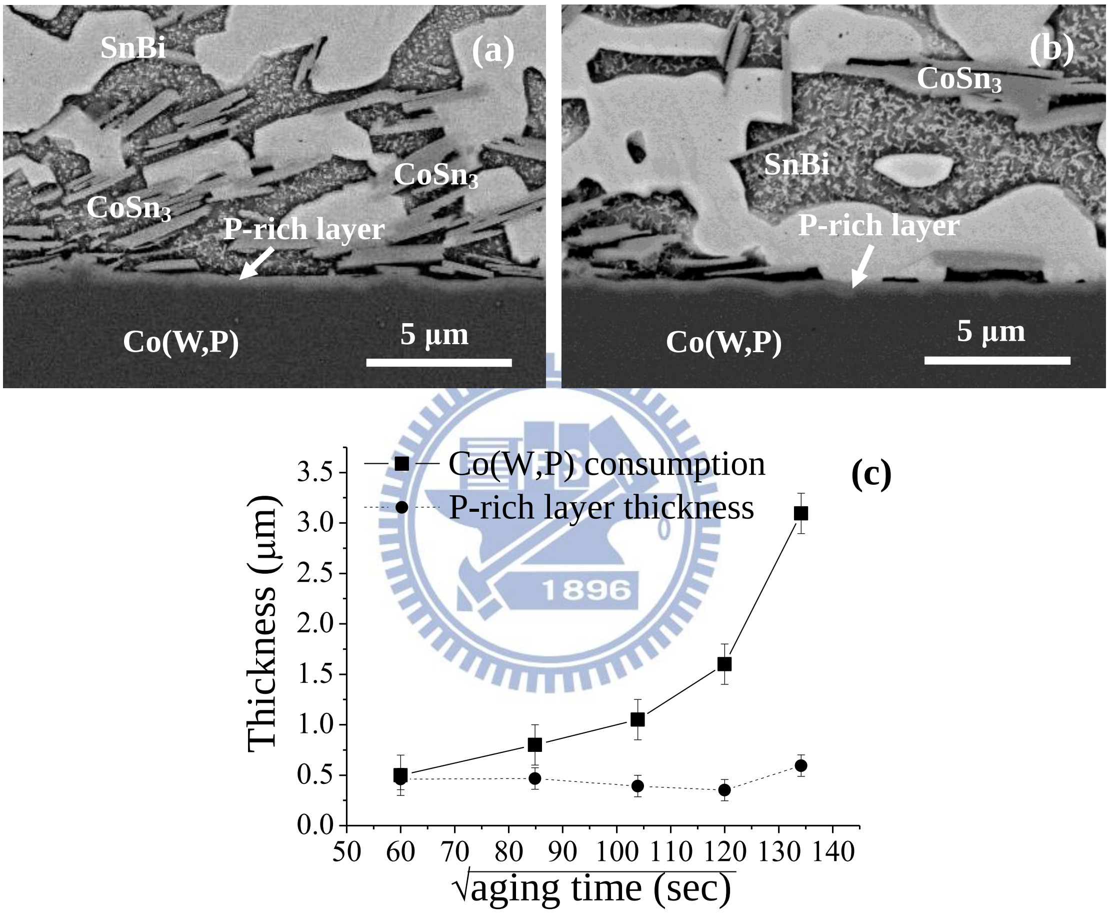

Figure 4-12. Cross-sectional SEM images of SnBi/α-Co(W,P) sample subjected to liquid-state aging for (a) 2 hrs and (b) 5 hrs. (c) Plot of thicknesses of the P-rich layer and the consumed Co(W,P) film versus square root of aging time. (BEI mode; accelerating voltage = 15 kV)

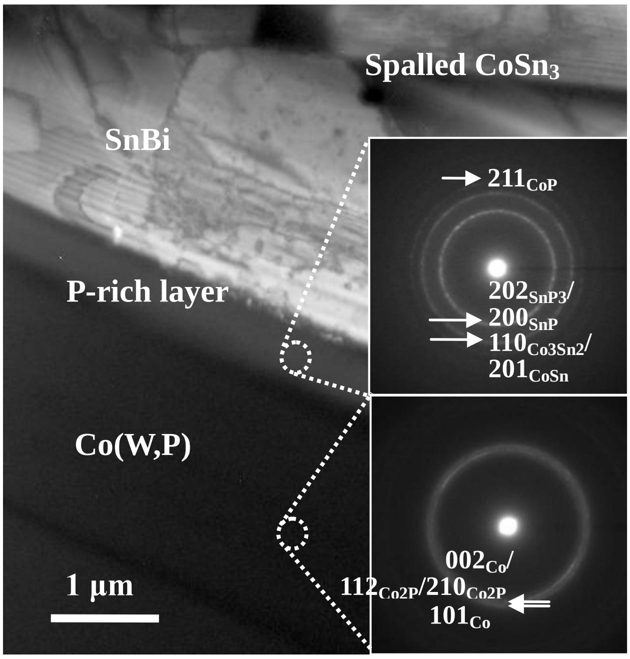

Figure 4-13. XTEM image of SnBi/α-Co(W,P) subjected to liquid-state aging for 1 hr. SAED patterns taken from P-rich layer and unreacted Co(W,P) (indicated by broken circles) are attached at right-hand side of micrograph.

An SAED pattern taken from the unreacted Co(W,P) region is also presented in Fig. 4-13. A careful examination of the diffraction pattern revealed that the α-Co(W,P) tends to recrystallize due to the high-temperature liquid-state aging and Co_2P IMCs emerges due to the supersaturated P content in Co(W,P). Grain boundaries in a polycrystalline layer may be the short-circuit diffusion paths. However, the content of Sn and Cu elements in the unreacted Co(W,P) is negligible, as illustrated by the EDS line scan profiles shown in Fig. 4-11(e). It is believed that the supersaturated P elements and Co_2P IMCs may segregate into the grain boundaries of the recrystallized

Co(W,P) to block the elemental diffusion. This confirms the mixed-type, *i.e.*, sacrificial- plus stuffed-type, diffusion barrier behavior of α-Co(W,P) in SnBi/α-Co(W,P)/Cu diffusion couple.

4.2.1.2. Solid-state Aging

Figures 4-14(a) and 4-14(b) separately present the SnBi/α-Co(W,P) samples subjected to solid-state aging for 1000 hrs together with their corresponding EDS line scan profiles. As shown in Fig. 4-14(a), $CoSn_3$ IMC clusters neighboring to an about 300-nm thick P-rich layer (P content is about 12 *at*.% and W content is about 1.8 *at*.%) were observed. The comparatively thinner P-rich layer is ascribed to the low solid-state aging temperature at 120°C in comparison with the liquid-state aging at high temperature of 250°C. EDS line scan profiles shown in Fig. 4-14(b) imply a similar barrier behavior as presented in the previous section, *i.e.*, the formation of IMCs indicates the sacrificial-type barrier characteristics while the high P content in Co(W,P) might provide the stuffed-type barrier behaviors.

An XTEM image corresponding to the sample shown in Fig. 4-14(a) is shown in Fig. 4-15(a) in which the lath-like IMCs and P-rich layer can be seen more clearly. Owing to the low solid-state aging temperature, the P-rich layer is more prone to be nano-crystalline as indicated by the broad concentric diffraction rings in the SAED

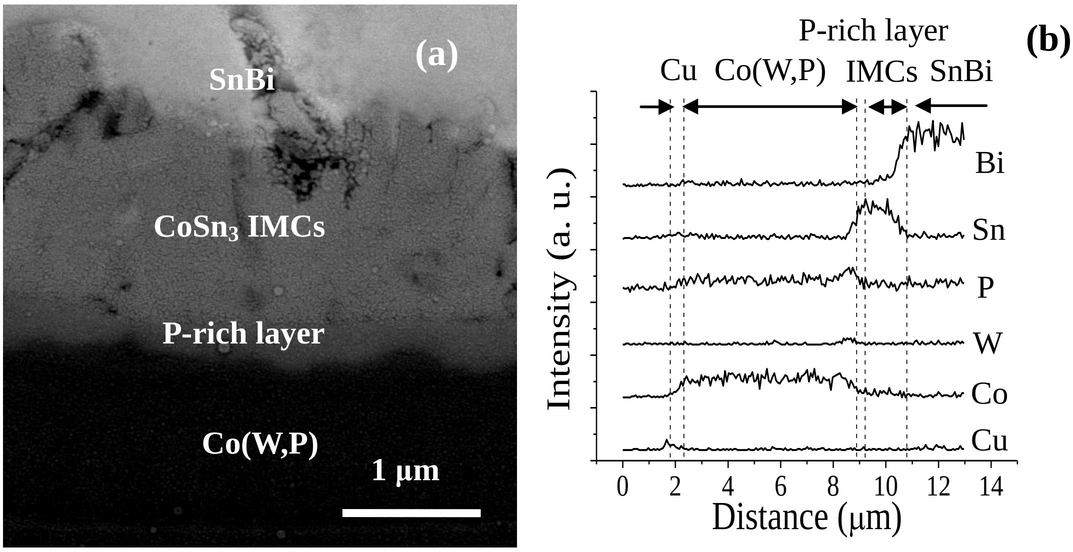

Figure 4-14. (a) Cross-sectional SEM micrograph of SnBi/α-Co(W,P) sample subjected to solid-state aging for 1000 hrs and (b) the corresponding EDS line scan profiles. (BEI mode; accelerating voltage = 15 kV)

pattern shown in Fig. 4-15(a). Figure 4-15(b) presents an XTEM image and SAED patterns taken from different portions of the unreacted Co(W,P). It can be seen from Fig. 4-15(b) that the solid-state aging temperature was too low to induce any substantial recrystallization in Co(W,P). The mainly amorphous structure in Co(W,P) seems to imply the amorphous-type barrier feature according to conventional classification schemes [29]. Nevertheless, subsequent analysis on poly-Co(W,P) samples indicated that it is disputable to correlate structure amorphism with the barrier capability. Although the high P content is the cause of amorphism, supersaturated P elements play a dominant role in inhibiting interdiffusion in the unreacted Co(W,P). Hence, in the case of SnBi/α-Co(W,P) couples subjected to solid-state aging, Co(W,P) remains a sacrificial- plus stuffed-type barrier rather than the sacrificial- plus amorphous-type barrier.

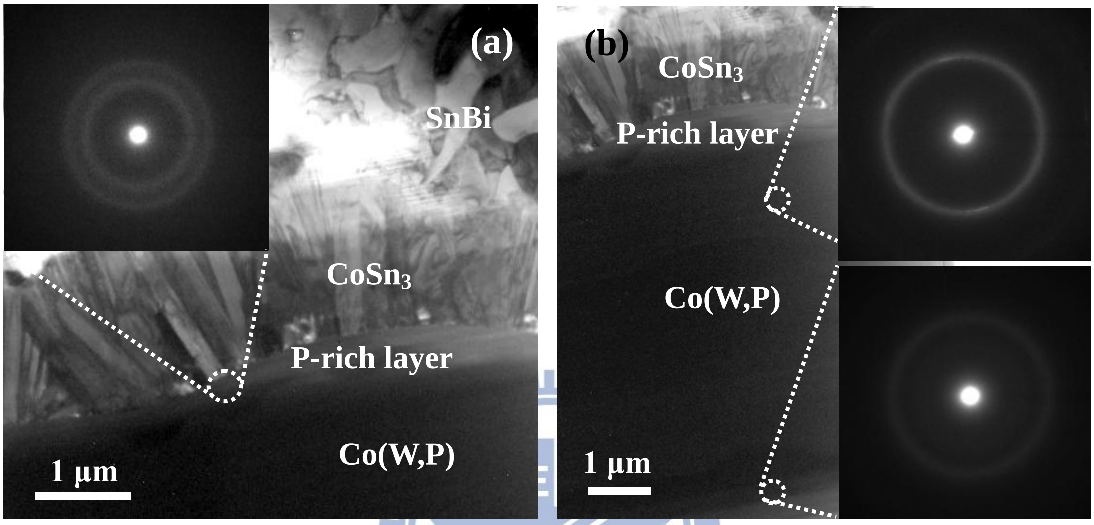

Figure 4-15. XTEM images taken from (a) reaction interface and (b) unreacted Co(W,P) in SnBi/α-Co(W,P) sample subjected to solid-state aging for 1000 hrs. The regions subjected by SAED analysis were indicated by broken circles.

4.2.2. SnBi/poly-Co(W,P) Samples

4.2.2.1. Liquid-state Aging

Figures 4-16(a)-(c) separately present the cross-sectional SEM views for a SnBi/poly-Co(W,P) couple subjected to liquid-state aging for 1, 2 and 5 hrs. EDS line scan profiles corresponding to the sample couple subjected to 1-hr liquid-state aging

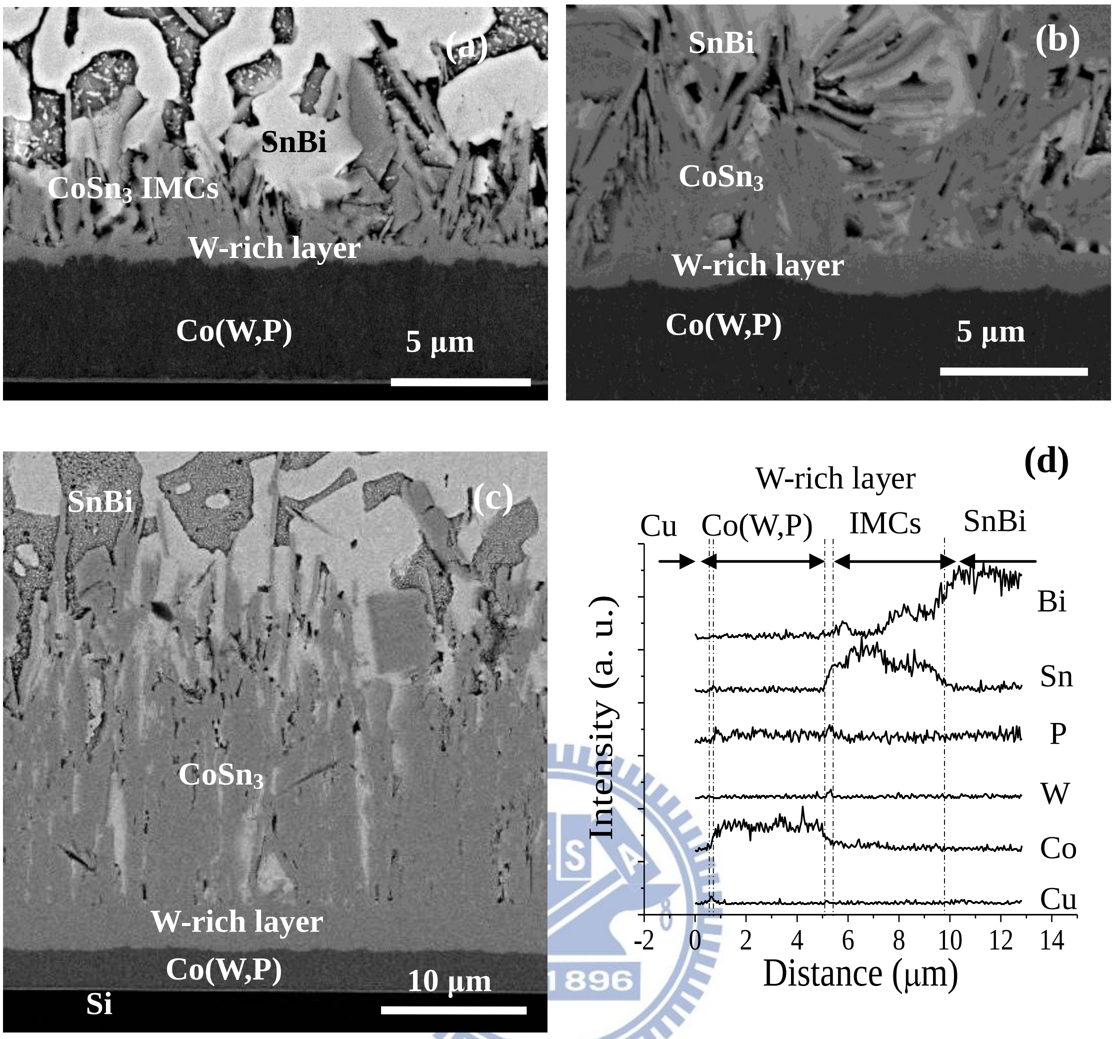

Figure 4-16. (a) Cross-sectional SEM images of SnBi/poly-Co(W,P) samples subjected to liquid-state aging for (a) 1 hr, (b) 2 hrs and (c) 5 hrs. (d) EDS line scan profiles corresponding to the sample subjected to 1-hr liquid-state aging. (BEI mode; accelerating voltage = 15 kV)

are depicted in Fig. 4-16(d). Unlike α-Co(W,P) does, lath-like $CoSn_3$ IMCs reside at the SnBi/Co(W,P) interface without spallation. SEM micrographs presented in Figs. 4-16(a)-(c) clearly depict that IMCs coarsen with the increase of aging time.

Continuous growth of IMCs clearly indicates the sacrificial-type barrier behavior of poly-Co(W,P).

Figures 4-16(a)-(c) also reveal a reaction layer between the IMCs and the Co(W,P) film. This reaction layer, in contrast to the P-rich layer observed for α-Co(W,P), consists of relatively high W content and thickens with increasing aging time. This thickening effect is illustrated in Fig. 4-17 which plots the thickness of this W-rich layer and the consumed Co(W,P) film *versus* the square root of aging time. The sacrificial nature of the poly-Co(W,P) film is further supported by the plot of consumption of Co(W,P) film *versus* the square root of aging time as shown in Fig. 4-17.

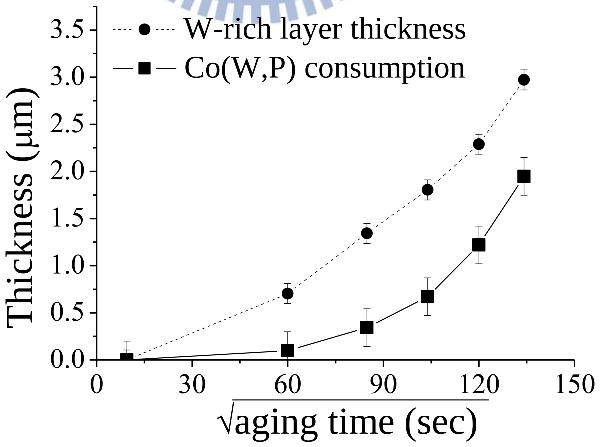

Figure 4-17. Plot of consumption of Co(W,P) layer and W-rich layer thickness *versus* square root of aging time in SnBi/poly-Co(W,P) samples subjected to liquid-state aging.

Also apparent from Fig. 4-17 is that the W-rich layer thickens at a rate faster than the rate of Co(W,P) consumption. The phase diagram for a Co-W binary alloy indicates that the solubility of W in Co is extremely low at temperatures below 500°C [94]. Hence, grain boundaries in poly-Co(W,P) are most likely the fast diffusion paths for the migration of P and W elements toward the reaction interface.

XTEM analysis for SnBi/poly-Co(W,P) couple subjected to 1-hr liquid-state aging is depicted in Fig. 4-18. SAED, in conjunction with EDS analysis, revealed the reaction layer is amorphous (see the attached SAED pattern in Fig. 4-18) with P content about 6 *at*.% and a surprisingly high W content about 15 *at*.%. Apparently, the consumption of Co by Sn to form the IMCs implies the accumulation of P and W elements at the reacting interface; the high W concentration might be due to the low solubility of W in Co and the relatively low P content in poly-Co(W,P) as discussed in Section 4.1.2. Furthermore, the Co_2P phase and/or the Co-W alloy phase detected by SAED/EDS analyses in the unreacted poly-Co(W,P) were in negligible amounts. This is ascribed to the very small P content in poly-Co(W,P) as well as the loss of W to the reaction interface *via* grain boundary diffusion. This weakens the role of stuffed-type barrier mechanism for the poly-Co(W,P) film and, therefore, we deduce that the Co(W,P) film is mainly a sacrificial-type barrier.

An interesting feature deduced from above analysis is that, even though the

W-rich layer is amorphous, it does not inhibit alloy reactions between the solder and the Co(W,P) film as illustrated by the continuous growth of IMCs into the solder as shown in Figs. 4-16(a)-(c). The diffusion barrier characteristics for amorphous films are generally attributed to the absence of fast-diffusion grain boundaries. However, amorphism may also be viewed as a chaotic structure with abundant crystalline defects which are essential for diffusion process. In conjunction with above finding, it seems that structure amorphism does not necessarily lead to the diffusion barrier capability [29]. Rather, it should be the nature of chemical bonding that governs the diffusion barrier characteristic of materials.

Another interesting finding deduced from the above characterizations is the correlation between IMCs spallation and the P content of Co(W,P) films. IMCs tend to spall away from the reacting interface for the sample containing an electroless Co layer with high P content. Guo *et al*. reported that solderability is suppressed in EN due to the presence of phosphide precipitates [120]. Sohn and Yu observed that IMCs spall away from Ni(P) surface when P content and reflow time are increased [121]. Furthermore, spallation is a result of interface energy reduction [122] and, therefore, in comparison with chunky type IMC, it would be easier for the needle-like IMC to spall away from the reaction interface due to its high surface-to-volume ratio feature. In addition to the good agreement with previous studies, our analytical results indicate that the P content in the electroless Co(W,P) layer affects not only its crystallinity, but also the structure evolution at the reacting interface and the diffusion barrier mechanism.

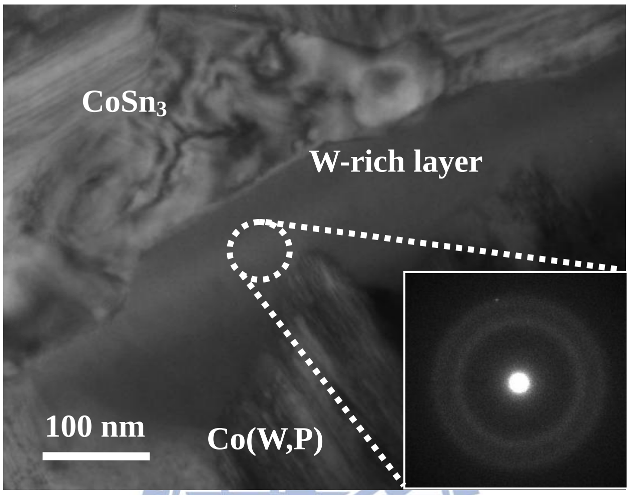

Figure 4-18. XTEM micrograph of reaction layer in SnBi/poly-Co(W,P) subjected to liquid-state aging for 1 hr. Attached SAED pattern was taken from the region in vicinity of reaction layer.

4.2.2.2. Solid-state Aging

Cross-sectional SEM views of SnBi/poly-Co(W,P) couples subjected to solid-state aging for 1000 hrs and corresponding EDS line scan profiles are presented in Figs. 4-19(a) and 4-19(b), respectively. Thick, lath-like IMCs can be seen and, according to the EDS analysis, they are mainly $CoSn_3$ type. The average IMC thickness is less than that observed in the samples subjected to liquid-state aging due to the lower solid-state aging temperature. This also leads to a thinner W-rich layer so that the SEM can barely reveal its existence. SEM characterizations on the samples aged at various time spans also found that IMCs thicken with the progress of aging time, implying the poly-Co(W,P) is mainly a sacrificial-type barrier.

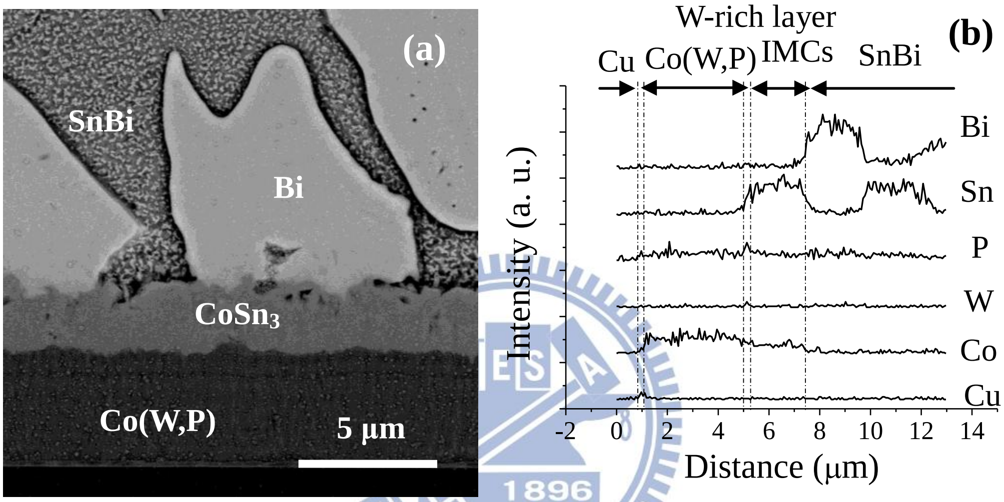

Figure 4-19. (a) Cross-sectional SEM image of SnBi/poly-Co(W,P) subjected to solid-state aging for 1000 hrs and (b) the corresponding EDS line scan profiles. (BEI mode; accelerating voltage = 15 kV)

4.2.3. Consumption of Co (W,P) with Various Crystallinities

Alloy reactions between SnBi solder and EN with different crystallinities at 110 and 130°C have been reported by Young *et al*. [123]. Since their aging temperatures are quite close to our solid-state aging temperature, a comparison is made to explore the barrier properties for EN and electroless Co(W,P) films. Figures 4-20 (a) and

4-20(b) separately present the thickness consumption data for Co(W,P) and EN layers. The data show that electroless Co(W,P) films have a lower consumption rates regardless of crystallinity. IMC thickness *versus* the square root of aging time for SnBi/Co(W,P) and SnBi/EN couples with different crystallinities are plotted in Figs. 4-21(a) and 4-21(b). The data show a slower IMC growth rate for electroless Co(W,P). Hence, electroless Co(W,P) is expected to be a better diffusion barrier to solder in comparison with EN.

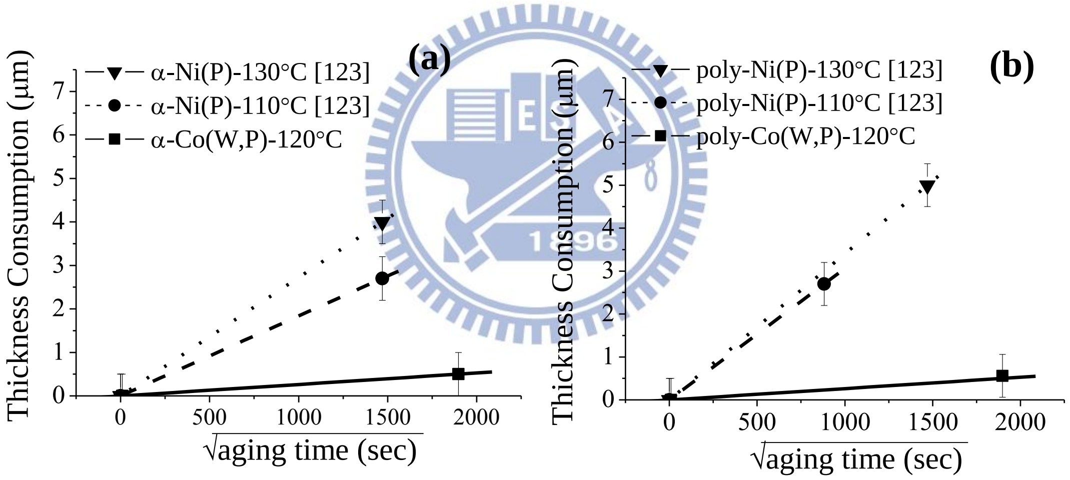

Figure 4-20. Thickness consumption of (a) α-Co(W,P) and EN and (b) poly-Co(W,P) and EN *versus* the square root of time.

Furthermore, α-Co(W,P) film is a better diffusion barrier than a crystalline Co(W,P) one due to its mixed-type barrier characteristic. Since IMCs are generally brittle, spallation might eliminate their bulk accumulation at the solder/Co(W,P) interface and affect the solder joint mechanical reliability. Nevertheless, α-Co(W,P) remains a sacrificial-type diffusion barrier that will react with solder during a reflow or soldering process. A sufficiently thick Co(W,P) layer (at least 1 μm for SnBi-related applications estimated in terms of above characterizations) is, therefore, required in order to avoid a total consumption of the barrier structure that may lead to the degradation of joint reliability.

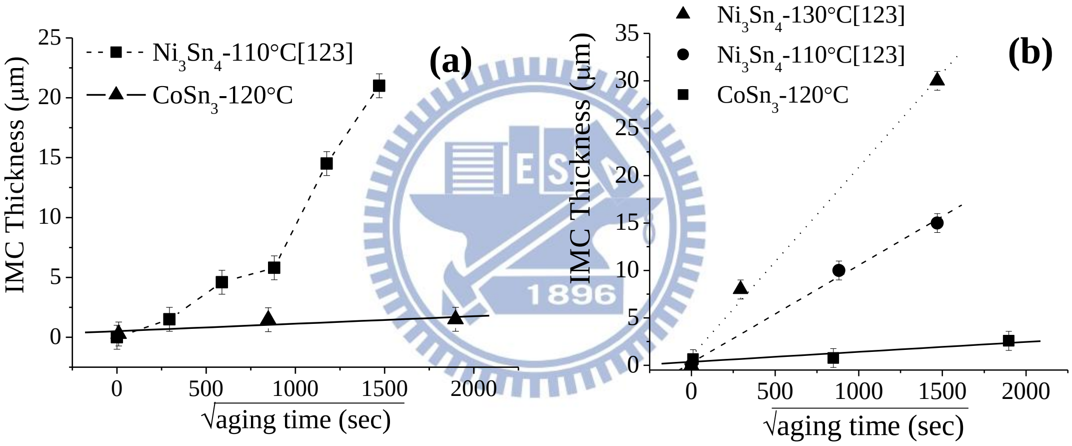

Figure 4-21. Variation of IMC thickness with the square root of time for (a) α-Co(W,P) and EN and (b) poly-Co(W,P) and EN.

4.3. Electroless Co(W,P) to SAC Solder

4.3.1. SAC/α-Co(W,P) Samples

4.3.1.1. Liquid-state Aging

Figures 4-22(a)-(e) present the SEM views of SAC/α-Co(W,P) sample at as-reflow condition and those subjected to liquid-state aging for 20 min, 1 hr, 3 hrs and 5 hrs. As shown in Fig. 4-22(a), the needle-like IMCs at the SAC/α-Co(W,P) interface and Ag_3Sn phases dispersed in the interior of solder were observed in the as-reflow sample. After 20-min aging, the spallation of lath-like IMCs into solder occurred and an about 1.7-μm thick reaction layer formed in between IMCs and Co(W,P) as depicted by Fig. 4-22(b). Figures 4-22(c)-(e) illustrate almost all IMCs spall away from the reaction layer when the aging time exceeds 1 hr and the IMCs coarsen into the irregular spheroid form. This observation supports the argument that the IMC spallation is an interface-energy-driven process [124]. In addition, the accumulation of P elements is another cause of the de-wetting of IMCs from the reacting interface.

EDS line scan profiles corresponding to the sample shown in Fig. 4-22(c) is given in Fig. 4-22(f) and Sn and Cu signals are negligibly observed in the unreacted Co(W,P). This indicates α-Co(W,P) may effectively inhibit the interdiffusion of Sn and Cu elements; however, the formation of IMCs depicted in Figs. 4-22(a)-(e) implies the sacrificial barrier behavior of α-Co(W,P).

Figures 4-23 (a) and (b) separately present the EDS spectra of Ag_3Sn and spalled IMCs shown in Fig. 4-22 (a) and (b). The composition (in *at.*%) of the spalled IMCs is about Co:Cu:Sn = 18.71: 5.21: 76.08. Previous studies of Sn-Co-Cu ternary system

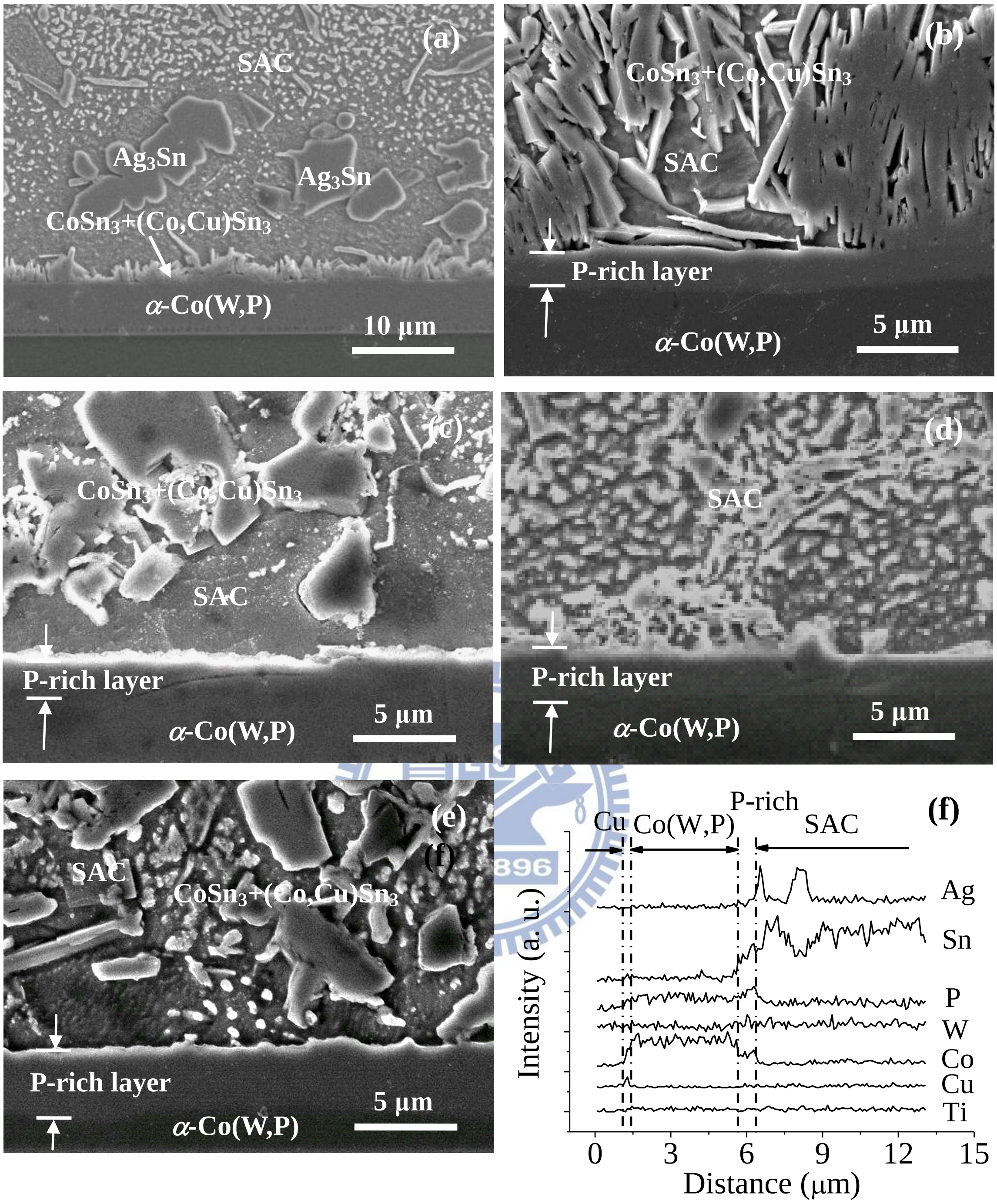
(a)
SAC
Ag$_3$Sn
Ag$_3$Sn
CoSn$_3$+(Co,Cu)Sn$_3$
α-Co(W,P)
10 µm
(b)
CoSn$_3$+(Co,Cu)Sn$_3$
SAC
P-rich layer
α-Co(W,P)
5 µm
(c)
CoSn$_3$+(Co,Cu)Sn$_3$
SAC
P-rich layer
α-Co(W,P)
5 µm
(d)
SAC
P-rich layer
α-Co(W,P)
5 µm
(e)
(f)
SAC
CoSn$_3$+(Co,Cu)Sn$_3$
P-rich layer
α-Co(W,P)
5 µm
(f)
Cu
Co(W,P)
P-rich
SAC
Ag
Sn
P
W
Co
Cu
Ti
Intensity (a. u.)
0
3
6
9
12
15
Distance (µm)

Figure 4-22. Cross-sectional SEM micrographs of (a) as-reflowed SAC/α-Co(W,P) sample and those subjected to liquid-state aging at 250℃ for (b) 20 min, (c) 1 hr, (d) 3 hrs and (e) 5 hrs. EDS line scan profiles corresponding to (c) is shown in (f). (SEI mode; accelerating voltage = 15 kV)

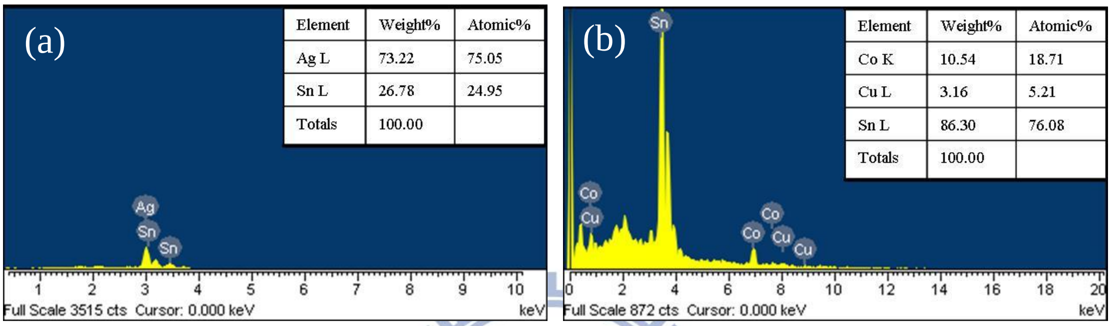

(a)

Element	Weight%	Atomic%
Ag L	73.22	75.05
Sn L	26.78	24.95
Totals	100.00	

(b)

Element	Weight%	Atomic%
Co K	10.54	18.71
Cu L	3.16	5.21
Sn L	86.30	76.08
Totals	100.00	

Figure 4-23. EDS spectra of (a) Ag_3Sn in Fig. 4-22 (a) and (b) the spalled IMCs in Fig. 4-22 (b).

indicated the solid solubility of Cu is about 4 *at.*% in $CoSn_3$ phase at 250℃ [125-126]. Hence, the spalled IMCs should be mainly the $(Co,Cu)Sn_3$ mixed with $CoSn_3$ phases. EDS analysis also revealed the P and W concentrations in the reaction layer are as high as 18 *at.*% and 2.5 *at.*%, respectively. Owing to the limited solid solubility, accumulation of P and W elements at reacting interface occurred when Co was consumed by Sn to form the IMCs as discussed previously. Such a reacting layer is termed P-rich layer as well. In addition to the interfacial energy reduction of IMCs, the high P content might also cause the IMC spallation since it suppresses the solderability as reported previously [75,81-82,120-121,127-129].

Figure 4-24 schematically plots of the thickness of P-rich layer as a function of the square root of aging time. A nearly-straight-line plot implies the diffusion-controlled mechanism for the growth of P-rich layer. Previous studies [12,85] and subsequent TEM analysis indicate the P-rich layer is in fact a mixture of nano-scale IMCs. As a result, the diffusion of Sn through P-rich layer to induce the IMC formation at the front of Co(W,P) should be the controlled process. Notably, previous study on eutectic SnBi/Co(W,P) system observed the rates of IMC formation and detachment at the P-rich layer are about the same, leading to a nearly constant value of P-rich layer thickness [85]. In contrast, the P-rich layer apparently thickened with the increase of aging time in the SAC/Co(W,P) system. This is ascribed to a relatively high Sn content in Pb-free SAC solder which results in more Sn flux into the P-rich layer and thus promotes the IMC formation.

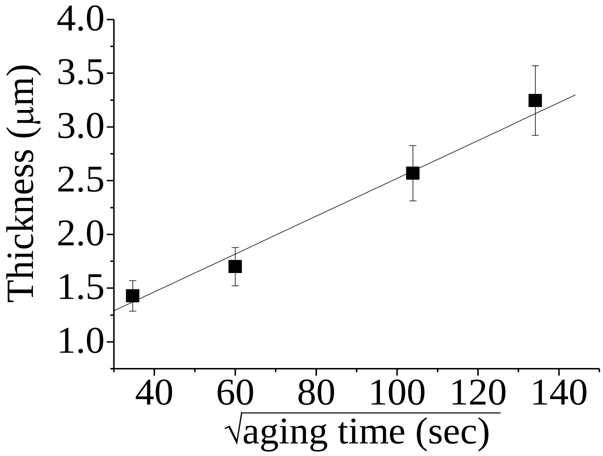

Figure 4-24. A plot of P-rich layer thickness as a function of the square root of aging time for SAC/α-Co(W,P) samples subjected to liquid-state aging test at 250℃.

The SAC/α-Co(W,P) sample subjected to 1-hr liquid-state aging was also characterized by TEM and the result is presented in Fig. 4-25. Insets at right-hand side of Fig. 4-25 show the SAED patterns taken from the P-rich layer and unreacted Co(W,P) area. Concentric rings in the SAED pattern of P-rich layer indicate the polycrystalline feature and, according to the index of pattern, such a layer is comprised of various IMC types. Further, a carful examination of SAED pattern for unreacted Co(W,P) found the initially amorphous Co(W,P) tends to recrystallize and the Co phosphide phase, Co_2P, emerges. The presence of uniformly dispersed Co_2P phase can also be seen in the TEM image of unreacted Co(W,P) as shown in Fig. 4-25. Since there is a negligible Cu and Sn diffusion into Co(W,P) as revealed by EDS analysis shown in Fig. 4-22(f), it is believed that the supersaturated P content and Co_2P precipitates might provide the stuffed-type barrier capability for α-Co(W,P). Hence, the electroless α-Co(W,P) serves as a combined-type, *i.e.*, sacrificial- plus stuffed-type, barrier in SAC/α-Co(W,P)/Cu system.

4.3.1.2. Solid-state Aging

Figures 4-26(a)-(c) present the SEM image, EDS line scan profiles and TEM micrograph of a SAC/α-Co(W,P) sample subjected to solid-state aging at 150°C for 1000 hrs. As depicted in Fig. 4-26(a), the layer-like IMCs agglomerate at the reacting

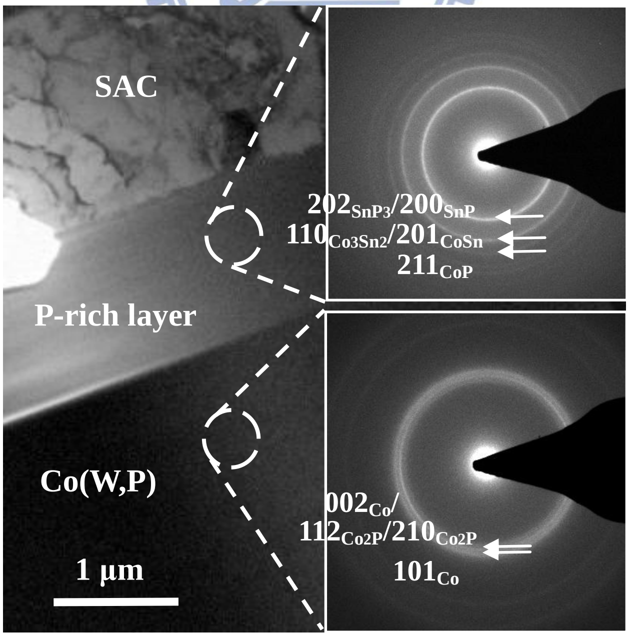

Figure 4-25. XTEM micrograph of SAC/α-Co(W,P) sample subjected to 1-hr liquid-state aging.

interface without spalling into the solder due to the solid-state aging environment. The composition (in *at*.%) of the IMCs is about Co: Cu: Sn = 4.58: 46.52: 48.9, indicating the main IMC type is the Cu_6Sn_5 phase. Cu_6Sn_5 phase exhibited a large solid solubility of Co up to 15 *at*.% at 250℃ according to the study on the Sn-Co-Cu ternary system [125-126]. Hence, the layer-like IMCs should be $(Cu,Co)_6Sn_5$ phase containing about 4.58 *at*.% Co. From the thermodynamic point of view, the $(Cu,Co)_6Sn_5$ phase was stabilized by the Co solutes in comparison with the Cu_6Sn_5 phase [125].

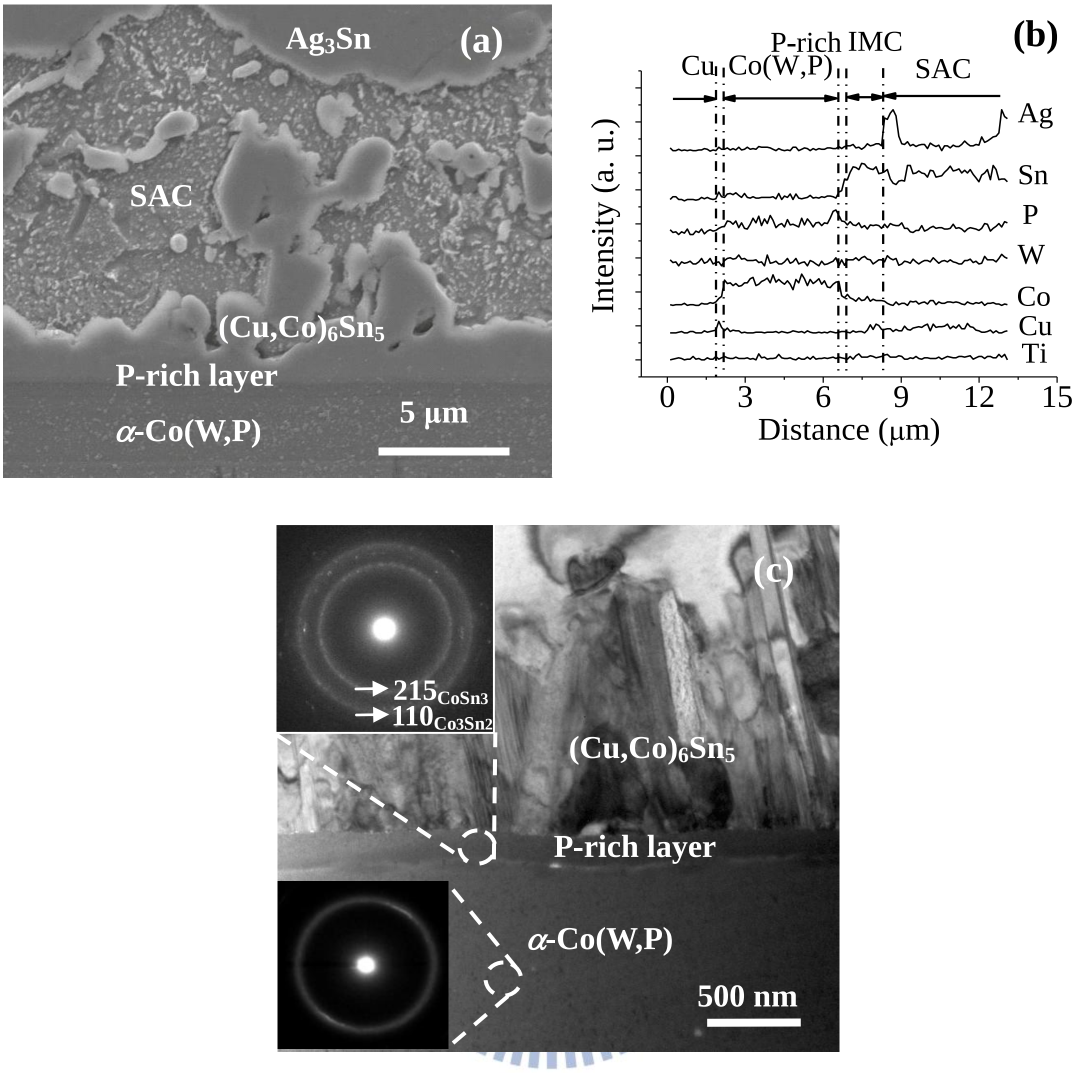

Figure 4-26. (a) SEM image (SEI mode; accelerating voltage = 15 kV), (b) EDS line scan profiles and (c) XTEM micrograph of SAC/*α*-Co(W,P) sample subjected to solid-state aging at 150°C for 1000 hrs.

As to the diffusion barrier capability of *α*-Co(W,P) layer, absence of Cu and Sn signals in unreacted Co(W,P) revealed by EDS line scan shown in Fig. 4-26(b) delineate the barrier capability of Co(W,P). Above results illustrate the sacrificial-type barrier feature of *α*-Co(W,P), similar to that reported in the liquid-state-aging experiment. Formation of polycrystalline P-rich layer was also observed by TEM as shown by the SAED inset at upper left-hand corner of Fig. 4-26(c). The emergence of bright spots randomly embedded in SAED patterns is ascribed to the relatively long solid-state aging time which results in the coarsening of IMCs in P-rich layer. Further, the TEM image contrast also reveals a fine dispersion of nano-scale precipitates in unreacted Co(W,P) and, in conjunction with SAED analysis, they should be the phosphide phase formed due to the supersaturated P elements in α-Co(W,P). Hence, the analytical results regarding of the solid-state aged sample also indicate the combined-type barrier behavior for α-Co(W,P), similar to that reported in previous section.

4.3.2. SAC/poly-Co(W,P) Samples

4.3.2.1. Liquid-state Aging

Figures 4-27(a)-(c) present the SEM image, EDS line scan profiles and TEM micrograph of SAC/poly-Co(W,P) sample subjected to the liquid-state aging at 250°C for 1 hr. EDS analysis revealed the IMC type is mainly $CoSn_3$ with some $(Co,Cu)Sn_3$ and $(Co,Ag)Sn_3$ IMCs occasionally as discussed above. In contrast to the α-Co(W,P) sample subjected to liquid-state aging, IMCs do not spall away from the reacting interface in the poly-Co(W,P) system (see Figs. 4-27(a) and 4-27(c)) and the IMC layer apparently thickens with the increase of aging time as indicated Fig. 4-28 which plots the IMC thickness as a function of aging time.

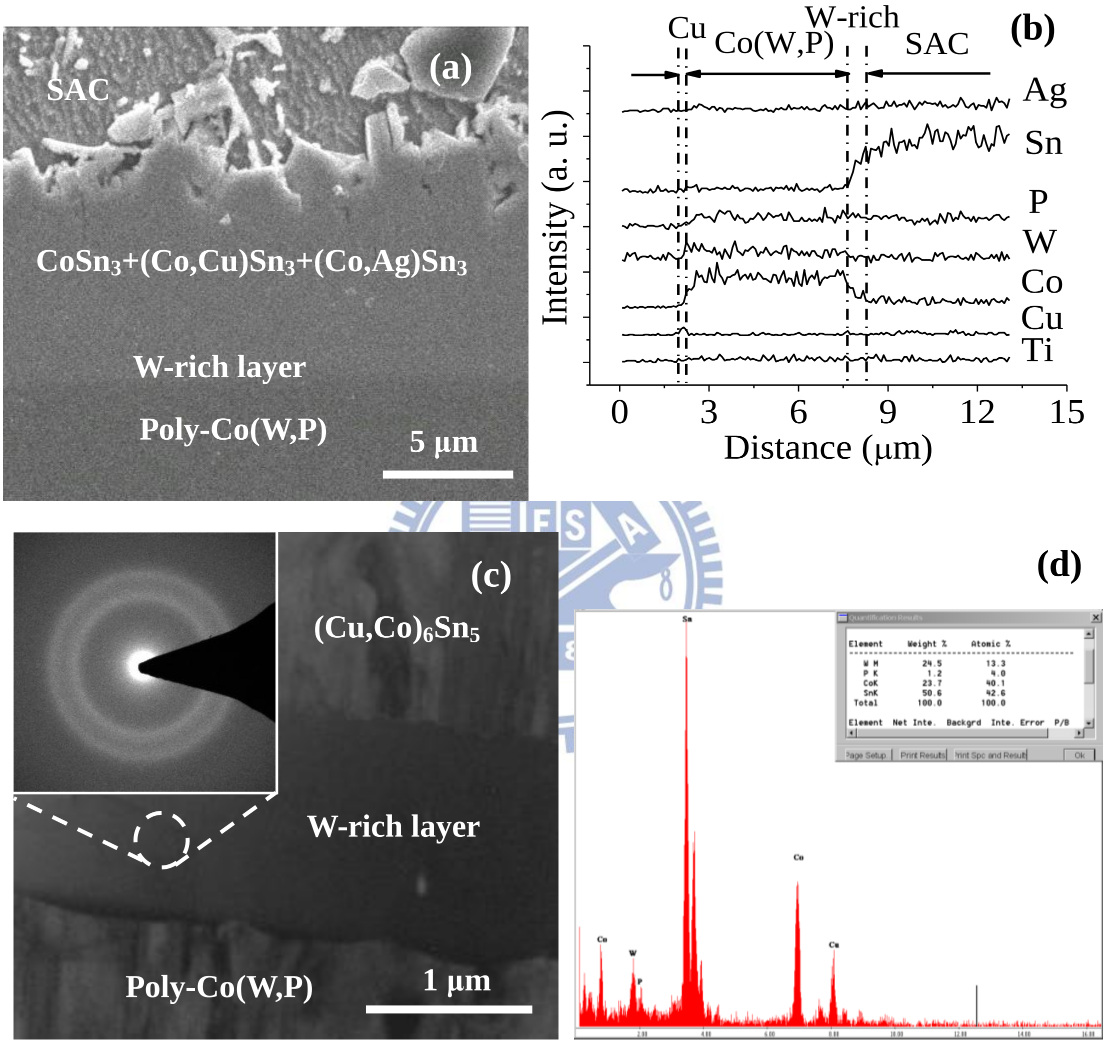

```
Element      Weight %      Atomic %
-------------------------------------------
   W M          24.5          13.3
   P K           1.2           4.0
   CoK          23.7          40.1
   SnK          50.6          42.6
  Total        100.0         100.0

Element   Net Inte.   Backgrd  Inte. Error  P/B
```

Figure 4-27. (a) SEM image (SEI mode; accelerating voltage = 15 kV), (b) EDS line scan profiles. (c) XTEM micrograph, and (d) TEM/EDS spectrum of SAC/poly-Co(W,P) sample subjected to liquid-state aging at 250°C for 1 hr.

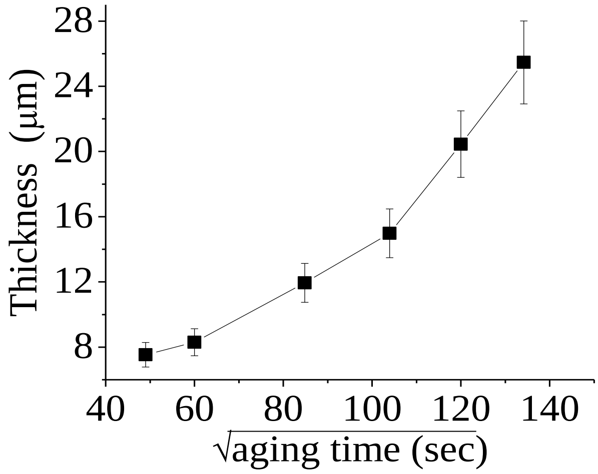

Figure 4-28. A plot of IMC thickness against the square root of aging time for SAC/poly-Co(W,P) samples subjected to liquid-state aging at 250℃.

TEM/EDS analysis revealed a distinctive feature in the poly-Co(W,P) sample that an amorphous W-rich layer (about 13.5 *at*.% W) emerges in beneath the IMCs as depicted by the XTEM micrograph shown in Fig. 4-27(c). The exceptionally high W content is ascribed to the element accumulation during the reaction of Sn and Co as well as the comparatively low P content in poly-Co(W,P). Notably, the plot of Fig. 4-28 delineates the amorphous W-rich layer does not inhibit subsequent alloy reactions of Sn and Co. Hence, the barrier capability is correlated to the nature of chemical bonds of the interacting materials [85,108], rather than the structure amorphism of the barrier layer as proposed by conventional classification scheme [29] as mentioned previously.

4.3.2.2. Solid-state Aging

SEM image, EDS line scan profiles, and XTEM micrograph of SAC/poly-Co(W,P) sample subjected to the solid-state aging at 150°C for 1000 hrs are separately presented in Figs. 4-29(a)-(c). A smoother IMC layer mainly constituted by the $(Cu,Co)_6Sn_5$ and a thinner W-rich layer were observed in the SAC/poly-Co(W,P) sample subjected to the solid-state aging, a result of the solid reacting environment and lower temperature of solid-state aging. In conjunction with the analytical results presented in the case of liquid-state aging, the electroless poly-Co(W,P) is categorized as a sacrificial-type diffusion barrier. Poly-Co(W,P) might also possess the stuffed-type barrier feature since the P elements may segregate to the grain boundaries of polycrystalline layer to block the atomic diffusion. However, such a behavior is less obvious in poly-Co(W,P) due to its lower P content in comparison with the case of α-Co(W,P). As a matter of fact, a pronounced IMC growth depicted by Fig. 4-28 clearly illustrates the dominance of sacrificial-type barrier feature in poly-Co(W,P).

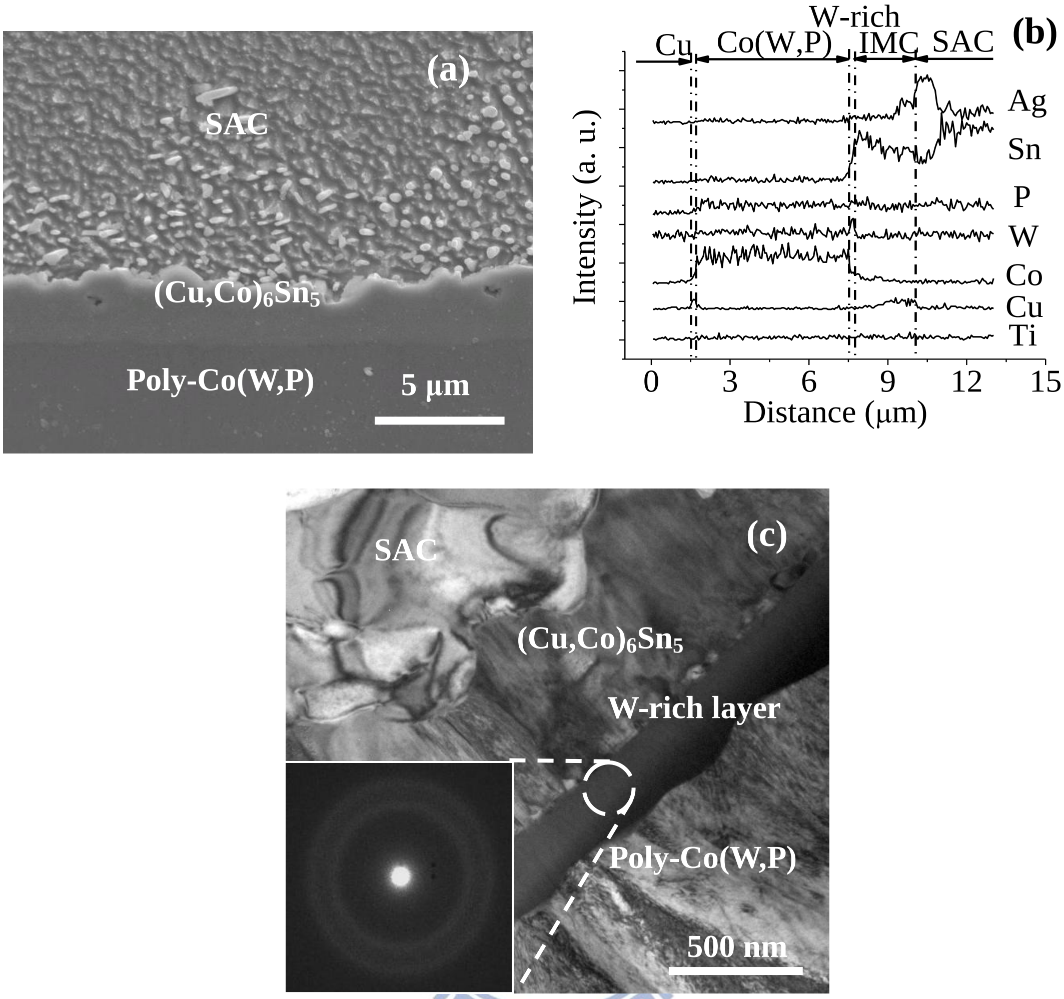

Figure 4-29. (a) SEM image (SEI mode; accelerating voltage = 15 kV), (b) EDS line scan profiles and (c) XTEM micrograph of SAC/poly-Co(W,P) sample subjected to solid-state aging at 150°C for 1000 hrs.

4.3.3. Determination of E_a of IMC Growth

In this work, the IMC thickness data as a function of time in the samples containing α-Co(W,P) and ploy-Co(W,P) subjected to solid-state aging at 130, 150 and 170°C up to 500 hrs were collected in order to determine the E_a's of IMC growth. For the purpose of comparison, the sample formed by applying SAC on pure Co metal foil was also prepared for aging test. Figure 4-30(a) plots the IMC thickness against the square root of time for various types of samples. At the same aging temperature, the IMC growth rates of SAC/electroless Co(W,P) samples are apparently slower than that of SAC/pure Co sample, evidencing the incorporation of P and W elements suppresses the Co-Sn alloy reactions and thus benefits the barrier capability. Further, the linearity of these plots implies the diffusion-controlled IMC growth in the analytical time span and, hence, the IMC thickness-time relation can be expressed as the equation (4-6) and (4-7). The values of E_a were calibrated from the slopes of ln$K$ *versus* 1/T plotted in Fig. 4-29(b), and it was found that E_a = 68, 81.8, and 110.7 kJ/mole for pure Co, electroless poly-Co(W,P), and electroless α-Co(W,P), respectively. Apparently, the relatively high P and W contents leading to the stuffed-type characteristic enhances the barrier capability of α-Co(W,P) so that it becomes a more efficient diffusion barrier. Here the improvement of barrier capability is not ascribed to the amorphism of α-Co(W,P) since previous TEM characterization has illustrated that the structure amorphism is unnecessarily correlated to the barrier capability of materials.

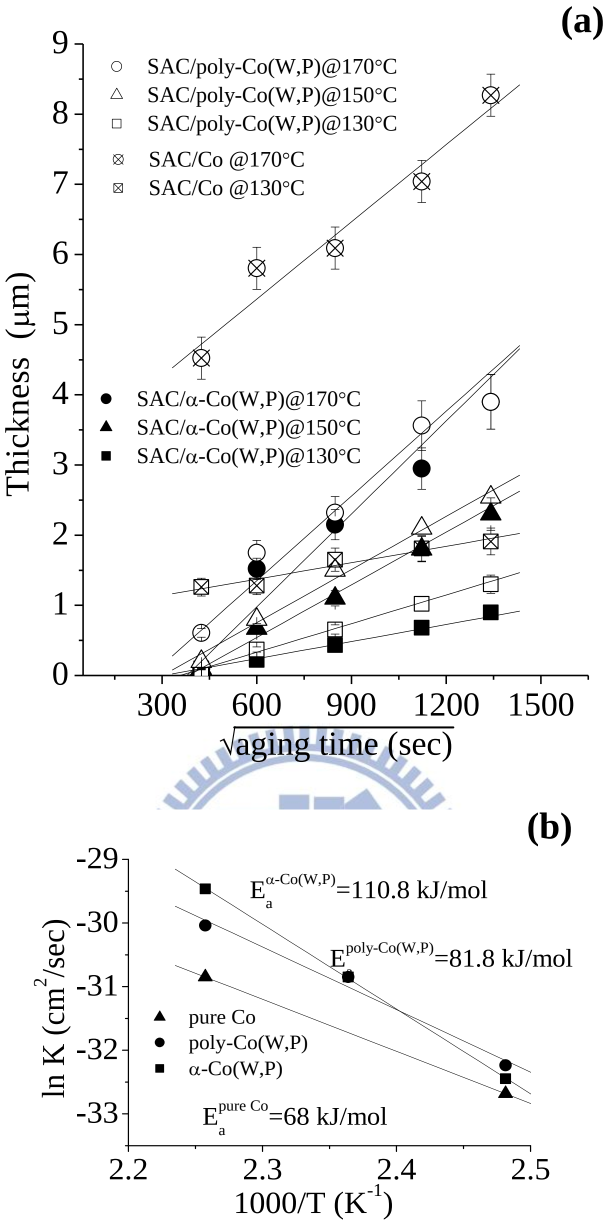

Figure 4-30. (a) IMC thickness against the square root of time for various SAC/Co samples subjected to solid-state aging at 130-170℃ up to 500 hrs. (b) Plots of ln*K* *versus* 1/*T* for the determination of the values of E_a for IMC growth.

4.3.4. Ball Shear Test

Figure 4-31 depicts the average shear strengths of SAC/α-Co(W,P) and SAC/poly-Co(W,P) samples as a function of time of liquid-state aging. Experimental results of SAC/electroless α-Ni(P) [112,130] and SAC/electrolytic Ni/Au [131] systems are also attached in Fig. 4-31 for comparison. It can be seen that, regardless of crystallinity of Co(W,P), the SAC/Co(W,P) systems exhibit rather high shear strengths in comparison with the systems utilizing Ni as the barrier layers. For SAC/α-Co(W,P) sample, the shear strength increased from 62.3 MPa to 91.6 MPa after 10-min aging. The bonding strength increased slightly when ageing time was raised to 30 min and then dropped to 80.8 MPa after 1-hr aging. Suppression of mechanical strength due to IMC spallation in the FC bonding systems has been reported previously [115,132]. In conjunction with the SEM characterizations presented in Fig. 4-22, this was similarly observed in the SAC/α-Co(W,P) sample that a decrease of bonding strength when a substantial IMC spallation occurred in the 1-hr aged sample. In the meantime, the solder became in contact with the P-rich layer with highly accumulated P elements. This leads to the deterioration of solderability which, in turn, causes the degradation of bonding strength.

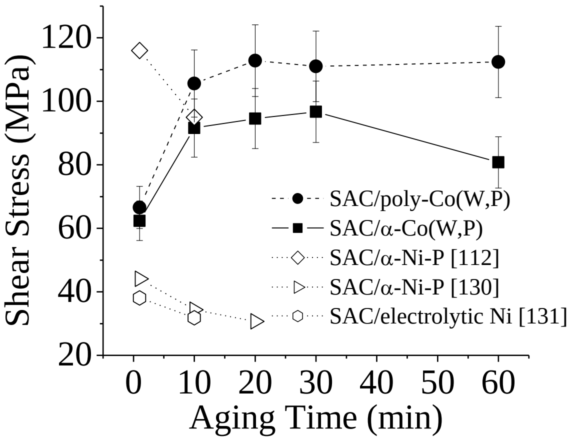

Figure 4-31 Shear strengths of SAC/Co(W,P) samples as a function of liquid-stage aging time. The results obtained by the studies [112,130,131] regarding of Ni barrier layers are also added for comparison.

As to the SAC/poly-Co(W,P) sample, maximum shear strength about 112.8 MPa was observed in 20-min aged sample and there was no drop in bonding strength when aging time extended to 1 hr. As illustrated in Fig. 4-30(a) which depicts an increase of IMC thickness with the increase of aging time, this is similar to previous studies [115,131,133-138] which reported the thickening of IMC have no apparent influence on bonding strength. Though bonding strength seems insensitive to the thickness of IMCs, the fracture mode changed in the samples subjected to prolonged aging presented as follows. Furthermore, the P content in ploy-Co(W,P) is comparatively lower than that in α-Co(W,P) and there is no IMC spallation in poly-Co(W,P) system as shown in Fig. 4-27. Analytical results presented above clearly indicate high P content is in fact adverse to the bonding strength. In practical view, the control of P content would be a key issue for electroless plating layer applied to UBM as the diffusion barrier.

Figures 4-32(a) and 4-32(b) separately present the summary of failure modes for SAC/α-Co(W,P) and SAC/poly-Co(W,P) samples in terms of the SEM observations on fracture surfaces and the JESD22-B117A Standard [107]. As revealed by a representative image of fracture surface shown in Fig. 4-33(a), both as-reflow samples exhibited the interfacial break (mode #4) mode since the exposure of IMC debris indicated the occurrence of fracture at solder/IMC interfaces. With the aging time was increased to about 10 to 20 min, about 20% of α-Co(W,P) samples transformed from interfacial break to ductile mode (mode #1) while all poly-Co(W,P) samples fractured by such a ball shear mode as illustrated by an SEM image shown in Fig. 4-33(b). Emergence of ductile mode indicated the completion of alloy interactions implies a good bonding in between solder and Co(W,P) layer so that the fracture occurs in the bulk of bumps. Pad lift (mode #2) dominated the fracture mode in α-Co(W,P) samples subjected to the aging for more than 20 min as shown by Fig. 4-32(a). The pad lift behavior is depicted by a typical fracture surface image in Fig. 4-33(c) which reveals the removal of Co(W,P) layer with solder ball to expose the Cu underlayer. We note the cracked Co(W,P) layers were occasionally observed in α-Co(W,P) samples

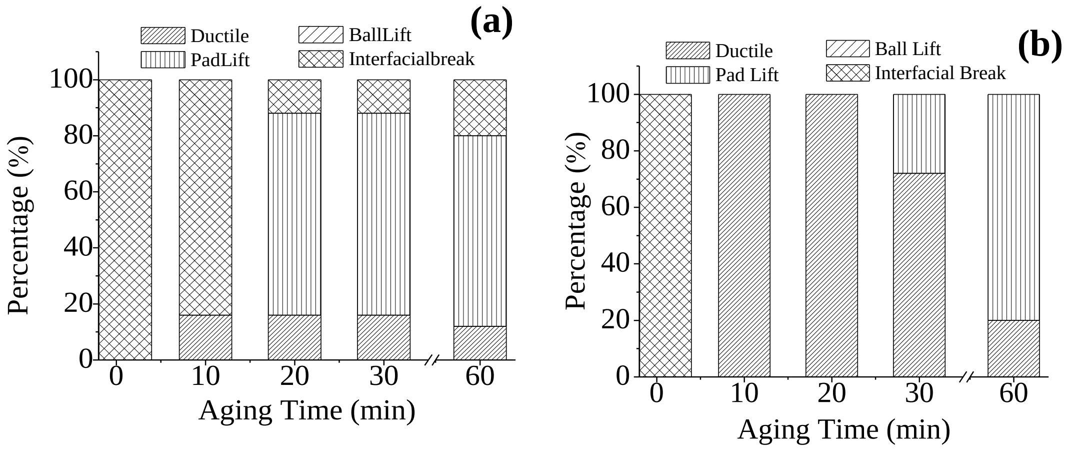

Figure 4-32. Summary of failure modes of (a) SAC/α-Co(W,P) and (b) SAC/poly-Co(W,P) samples in terms of the SEM observations on facture surfaces and JESD22-B117A Standard [93].

subjected to prolonged aging as shown in Fig. 4-33(d). In addition to the brittle features of IMCs [139-141] and deterioration of adhesion due to the high P content, the pad lift behavior might also be correlated to the formation of Co_2P precipitates and the glassy transition of α-Co(W,P) layer. The precipitation hardening increases the hardness and suppresses the toughness of α-Co(W,P) layer. The amorphous-to-crystalline transition in aged Co(W,P) layer caused a change of thermal expansion coefficient (CTE) which, in turn, induced the thermal stress that might break the barrier layer. Delamination and, hence, the pad lift occurred to degrade the bonding strength of α-Co(W,P) samples subjected to prolonged aging. This might be another weakness for amorphous-type diffusion barrier when exposed to high-temperature environments in practical applications.

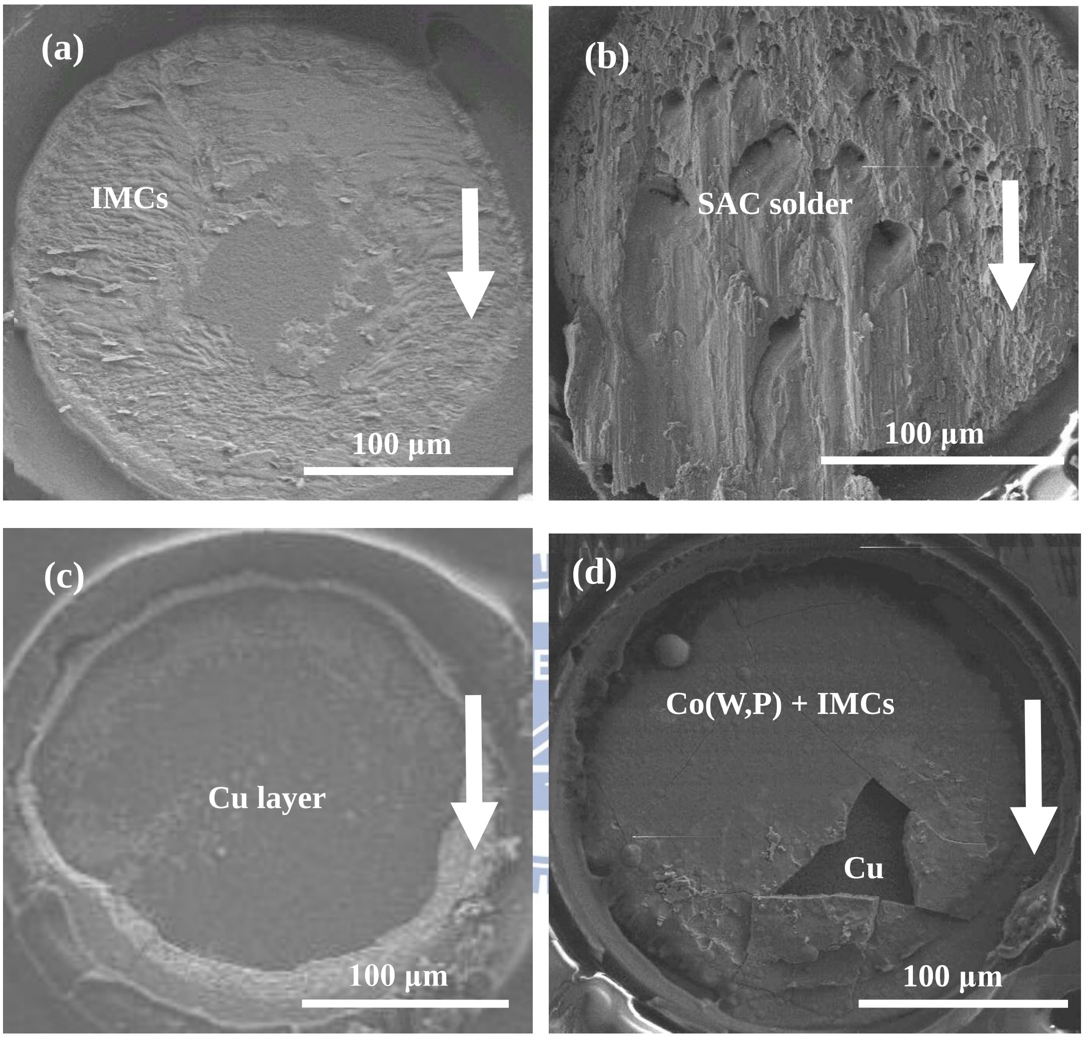

Figure 4-33. Fracture surfaces of (a) as-reflow SAC/poly-Co(W,P) sample, (b) SAC/poly-Co(W,P) sample subjected to 20-min aging, (c) SAC/α-Co(W,P) sample subjected to 20-min aging and (d) crack of Co(W,P) layer in SAC/α-Co(W,P) sample subjected to 30-min aging. The arrow in each micrograph indicates the shear direction.

Ductile mode remained the main fracture mode for poly-Co(W,P) samples subjected to aging up to 30 min. The desired failure mode is ascribed to the relatively low P content and absence of recrystallization in aged poly-Co(W,P) layer. As to the samples aged for 1 hr, the pad lift became the dominant failure mode. Though no obvious drop in bonding strength, the breakage in a brittle manner was observed during the shear test in a large portion of 1-hr aged poly-Co(W,P) samples. The pad lift behavior might be ascribed to the deterioration of adhesion of electroless Co(W,P) on Cu underlayer; however, the exact origin of this phenomenon is still required further study.

Chapter 5

Conclusions

Diffusion barrier characteristics of electroless α-Co(W,P) and poly-Co(W,P) layers to PbSn, SnBi, and SAC solders are presented. The values of E_a of IMC growth and bonding properties of PbSn/Co(W,P) and SAC/Co(W,P) systems with various crystallinities are reported as well.

In all samples containing α-Co(W,P) subjected to liquid-state aging, spallation of IMCs into solders, formation of polycrystalline P-rich layer and recrystallization of α-Co(W,P) were observed. For solder/α-Co(W,P) samples subjected to solid-state aging, a thick IMC without spallation and an underlying P-rich layer formed in between solders and Co(W,P). Analytical results indicated such a P-rich layer cannot retard subsequent Co-Sn interactions and the α-Co(W,P) layer serves as a combined type, *i.e.*, the sacrificial- plus stuffed-type, barrier regardless of aging type.

For the samples containing poly-Co(W,P) subjected to the liquid-state aging, IMCs neighboring to an amorphous W-rich layer was observed at the solder/Co(W,P) interface regardless of aging types. The poly-Co(W,P) layer served mainly as a sacrificial-type barrier. The incapability of W-rich layer to inhibit subsequent alloy reactions indicated structure amorphism does not necessarily imply the barrier property. As a matter of fact, the barrier capability of materials should correlate to the nature of chemical bonds.

The E_a's of IMC growth in PbSn/α-Co(W,P), PbSn/poly-Co(W,P), PbSn/pure Co, SAC/α-Co(W,P), SAC/poly-Co(W,P), and SAC/pure Co samples deduced from solid-state aging were found to be 338.6, 167.5, 89, 110.7, 81.8, and 68 kJ/mol, respectively. The enhancement of barrier capability in α-Co(W,P) is ascribed to its relatively high P and W contents which lead to the stuffed-type characteristic in the electroless layer.

Ball shear test revealed a dominance of ductile failure in both PbSn/α-Co(W,P) and PbSn/poly-Co(W,P) samples, whereas interfacial break dominated at short-time aged samples and pad lift dominated when aging time was long in SAC/α-Co(W,P) case. The decrement of bonding strength due to pad lift failure was ascribed to the deterioration of adhesion due to high P content, toughness loss due to the formation of Co_2P precipitates and the thermal stress induced by the change of CTE due to the recrystallization of α-Co(W,P) layer. Except in the as-reflow sample, the ductile mode dominated the failure of SAC/poly-Co(W,P) samples in most aging conditions. As the result, relatively high P content in α-Co(W,P) might be a concern on future applications since it degrades the mechanical performance of FC bonding.

References

1. *Flip Chip Technologies*, ed. by J.H. Lau, McGraw-Hill, New York, (1996).

2. R.H. Uang, K.C. Chen, S.W. Lu, H.T. Hu, S.H. Huang, in: L.T. Beng, C. Lee ,T. K. Chuan (Eds), *Proceedings of 3rd IEEE Electronic Packaging Technology Conference*, Singapore, *EPTC2000*, December 5-7, (2000), p.292.

3. M.W. Liang, T.-E. Hsieh, C.C. Chen and Y.T. Hung, "Electroless Copper/Nickel Films Deposited on AlN Substrates", *Jpn. J. Appl. Phys.*, **43** (2004), p.8258-8266.

4. T. Oppert, E. Zakel, T. Teutsch, in: *Proceedings of the International Electronics Manufacturing Technology Symposium (IEMT) Symposium*, Omiya, Japan, April 15-17, 1998, *Proceedings of 2nd IEMT/IMC Symposium*, (1998), p.106.

5. T. Teutsch, T. Oppert, E. Zakel and E. Klusmann, in: *Electronic Component and Technology Conference*, Las Vegas, NV, USA, IEEE 2000, (2000), p.107.

6. G.O. Mallory and J.B. Hajdu, *Electroless Plating: Fundamentals and Applications*, AESF Orlando, Florida, USA, (1990).

7. E.J. O'Sullivan, A.G. Schrott, M. Paunovic, C.J. Sambucetti, J.R. Marino, P.J. Bailey, S. Kaja and K.W. Semkow, "Electrolessly Deposited Diffusion Barriers for Microelectronics", *IBM J. Res. Dev.*, **42**(1998), p.607-620.

8. M.W. Liang, H.T. Yen and T.-E. Hsieh, "Investigation of Electroless

Cobalt-phosphorous Layer and its Diffusion Barrier Properties of PbSn Solder", *J. Electron. Mater.*, **35** (2006), p. 1593-1599.

9. A. Kohn, M. Eizenberg, Y. Shacham-Diamand and Y. Sverdlov, "Characterization of Electroless Deposited Co(W,P) Thin Film for Copper Metallization", *Mater. Sci. Eng. A*, **302**(2001), p.18-25.
10. A. Kohn, M. Eizenberg, Y. Shacham-Diamand, B. Israel and Y. Sverdlov, "Evaluation of Electroless Deposited Co(W,P) Thin Film as Diffusion Barriers for Copper Metallization", *Microelectron. Eng.*, **55**(2001), p.297-303.
11. A. Kohn, M. Eizenberg and Y. Shacham-Diamand, "The Role of Microstructure in Nanocrystalline Conformal $Co_{0.9}W_{0.02}P_{0.08}$ Diffusion Barriers for Copper Metallization", *Appl. Surf. Sci.*, **212-213**(2003), p.367-372.
12. W.C. Wu, T.-E. Hsieh and H.C. Pan, "Investigation of Electroless Co(W,P) Thin Film as the Diffusion Barrier of Under Bump Metallurgy", *J. Electrochem. Soc.*, **155**(2008), p.D369-D376.
13. R. Singh and R.K. Ulrich, "High and Low Dielectric Constant Materials", *The Electrochemical Society INTERFACE*, **8**(Summer 1999), p.26-30.
14. K. Holloway and P.M. Fryer, "Tantalum as a Diffusion Barrier between Copper and Silicon", *Appl. Phys. Lett.*, **57**(1990), p.1736-1738.
15. K. Holloway, P.M. Fryer, C. Cabral, Jr., J. M.E. Harper, P.J. Bailey and K.H.

Kelleher, “Tantalum as a Diffusion Barrier between Copper and Silicon: Failure Mechanism and Effect of Nitrogen Additions”, *J. Appl. Phys.*, **71**(1992), p.5433-5444.

16. D.S. Yoon, H.K. Baik and S.M. Lee, “Effect on Thermal Stability of a Cu/Ta/Si Heterostructure of the Incorporation of Cerium Oxide into the Ta Barrier”, *J. Appl. Phys.*, **83**(1998), p.8074-8076.
17. R.H. Havemann and J.A. Hutchby, “High Performance Interconnects: An Integration Overview”, *Proceedings of the IEEE*, Vol.89, No.5, May 2001.
18. S. Hymes, S.P. Murarka, C. Shepard and W.A. Lanford, “Passivation of Copper by Silicide Formation in Dilute Silane”, *J. Appl. Phys.*, **71**(1992), p.4623-4625.
19. W.A. Lanford, P.J. Ding, W. Wang, S. Hymes and S.P. Muraka, “Low Temperature Passivation of Copper by Doping with Al or Mg”, *Thin Solid Films*, **262**(1995), p.234-241.
20. W.A. Lanford, P.J. Ding, Wei Wang, S. Hymes, S.P. Muraka, “Alloying of Copper for Use in Microelectronic Metallization”, *Mater. Chem. Phys.*, **41**(1995), p.192-198.
21. P. J. Ding, W.A. Lanford, S. Hymes and S.P. Murarka, “Oxidation Resistant High Conductivity Copper Films”, *Appl. Phys. Lett.*, **64**(1994), p.2897-2899.
22. P. J. Ding, W. A. Lanford, S. Hymes and S.P. Murarka, “Effects of the Addition of

Small Amounts of Al to Copper: Corrosion, Resistivity, Adhesion, Morphology, and Diffusion”, *J. Appl. Phys.*, **75**(1994), p.3627-3631.

23. J.M. Sterigerwald, S.P. Muraka, R.J. Gutmann and D.J. Duquette, “Chemical Process in the Chemical Mechanical Polishing of Copper”, *Mater. Chem. Phys.*, **41**(1995), p.217-228.
24. C.W. Kaanta, S.G. Bombardier, W.J. Cote, W.R. Hill, G. Kerszykowski, H.S. Landis, D.J. Poindexter, C.W. Pollard, G.H. Ross, J.G. Ryan, S. Wolff and J.E. Cronin, in: *Proceedings of the 8th VLSI Multilevel Interconnection Conference*, “Dual Damascene: A ULSI Wiring Technology”, *IEEE VMIC Conf.*, (1991), p.144-152.
25. J.W. Mayer and S.S. Lau, *Electronic Materials Science: For Integrated Circuits in Si and GaAs*, Macmillan, New York, (1990), p160-162.
26. E.M. Davis, W.E. Harding, R.S. Schwartz and J.J. Corning, “Solid Logic Technology: Versatile High Performance Microelectronics”, *IBM J. Res. Dev.*, **8**(1964), p.102.
27. Leif Halbo and Per Ohlckers, *Electronics Components, Packaging and Production*, University of Oslo, Norway, (1995).
28. 謝宗雍，*微電子材料與製程*，第十章，電子封裝技術，p.385-467，2000 年。

29. M.A. Nicolet, “Diffusion Barriers in Thin Films”, *Thin Solid Films*, **52**(1978), p.415-443.

30. S. Anhock, A. Ostmann, H. Oppermann, R. Aschenbrenner and H. Reichl, “Reliability of Electroless Nickel for High Temperature Applications”, *Electronic Materials and Packaging*, 1999 International Symposium on Advance Packaging Materials.

31. 顏慧婷，*“以無電鍍技術沉積鈷磷合金應用於銲錫擴散阻障層之研究”*，*國立交通大學材料與科學工程學系*，*碩士論文*，民國 94 年。

32. K.C. Hung, Y.C. Chan and C.W. Tang, “Metallurgical Reaction and Strength of Electroless Ni-P Solder Joints for Advanced Packaging Applications”, *J. Mater. Sci.*, **11**(2000), p.587-593.

33. P.T. Vianco and D.R. Frear, “Issues in the Replacement of Lead-bearing”, *JOM*, **45**(1993), p.14-18.

34. D.R. Frear, J.W. Jang, J.L. Lin and C. Zhang, “Pb-Free Solders for Flip-Chip Interconnects”, *JOM*, **53**(2001), p.28-32.

35. K.L. Erickson, P.L. Hopkins and P.T. Vianco, “Modeling the Solid-state Reaction between Sn-Pb Solder and a Porous Substrate Coating”, *J. Electron. Mater.*, **27**(1998), p.1177-1192.

36. P.T. Vianco, A.C. Kilgo and R. Grant, “Intermetallic Compound Layer Growth

by Solid State Reactions between 58Bi-42Sn Solder and Copper", *J. Electron. Mater.*, **24**(1995), p.1493-1505.

37. J.K. Kivilahti, "The Chemical Modeling of Electronic Materials and Interconnects", *JOM*, **54** (2002), p.52–57.

38. T. Laurila, V. Vuorinen and J.K. Kivilahti, "Interfacial Reactions between Lead-free Solders and Common Base Materials", *Mater. Sci. Eng. R-Rep.*, **49**(2005), p.1-60.

39. *Binary Alloy Phase Diagrams*, ed. by T.B. Massalski, 2nd ed., ASM International, Materials Park, OH (1990).

40. J.D. Bernal, "The Complex Structure of the Copper-tin Intermetallic Compounds", *Nature*, **122**(1928), p.54.

41. A. Gangulee, G.C. Das and M.B. Bever, "An *X*-ray Diffraction and Calorimetric Investigation of the Compound Cu_6Sn_5", *Metall. Mater. Trans. B*, **4**(1973), p.2063-2066.

42. A.K. Larsson, L. Stenberg and S. Lidin, "The Superstructure of Domain-twinned η'-Cu_6Sn_5", *Acta Crystallogr. B*, **50**(1994), p.636-643.

43. C.R. Kao, "Microstructures Developed in Solid-Liquid Reactions: Using Cu-Sn Reaction, Ni-Bi Reaction, and Cu-In Reaction as Examples", *Mater. Sci. Eng. A*, **238**(1997), p.196-201.

44. R.A. Gagliano, G. Ghosh and M.E. Fine, “Nucleation Kinetics of Cu_6Sn_5 by Reaction of Molten Tin with a Copper Substrate”, *J. Electron. Mater.*, **31**(2002), p.1195-1202.

45. H.C. Bhedwar, K.K. Ray, S.D. Kulkarni and V. Balasubramanian, “Kirkendall Effect Studied in Copper-tin Diffusion Couples”, *Scripta Metall.*, **6**(1972), p.919-922.

46. M. Onishi and H. Fujibuchi, “Reaction-Diffusion in the Cu-Sn System”, *Trans. Jpn. Inst. Met.*, **16**(1975), p.539-548.

47. C. Wagner, “The Evaluation of Data Obtained with Diffusion Couples of Binary Single-Phase and Multiphase Systems”, *Acta Metall.*, **17**(1969), p.99-107.

48. K.N. Tu and R.D. Thompson, “Kinetics of Interfacial Reaction in Bimetallic Cu-Sn Thin Films”, *Acta Metall.*, **30**(1982), p.947-952.

49. L. Revay, “Interdiffusion and Formation of Intermetallic Compounds in Tin-copper Alloy Surface Coatings”, *Surf. Technol.*, **5** (1977), p.57-63.

50. Z. Mei, A.J. Sunwoo and J.W. Morris, Jr., “Analysis of Low-Temperature Intermetallic Growth in Copper-Tin Diffusion Couples”, *Metal. Trans. A*, **23**(1992), p.857-864.

51. Minseok Oh, “Growth Kinetics in Intermetallic Phases in the Cu-Sn Binary and the Cu-Ni-Sn Ternary Systems at Low Temperatures”, *Doctorate Dissertation*,

Lehigh University, 1994.

52. C. Schmetterer, H. Flandorfer, K.W. Richter, U. Saeed, M. Kauffman, P. Roussel and H. Ipser, “A New Investigation of the System Ni-Sn”, *Intermetallics,* **15**(2007), p.869-884.

53. F. Lihl and H. Kirnbauer, “Untersuchung binärer metallischer Systeme mit Hilfe des Amalgamverfahrens. Das System Nickel-Zinn”, *Monatsh. Chem.*, **86**(1955), p.745-751.

54. H. Fjellvag and A. Kjekshus, “Structural Properties of Co_3Sn_2, Ni_3Sn_2 and Some Ternary Derivatives”, *Acta Chem. Scand.*, **40A**(1986), p.23-30.

55. M. Ellner, “Über Die Kristallchemischen Parameter Der Ni-, Co- und Fe-haltigen Phasen Vom NiAs-Typ”, *J. Less Common Met.*, **48**(1976), p.21-52.

56. A. Leineweber, M. Ellner and E.J. Mittermeijer, “A NiAs/Ni_2In-Type Phase $Ni_{1+x}Sn$ ($0.35<x<0.45$) with Incommensurate Occupational Ordering of Ni”, *J. Solid State Chem.,* **159(**2001), p.191-197.

57. A. Leineweber, O. Oeckler, and U. Zachwieja, “Static Atomic Displacements of Sn in Disordered NiAs/Ni_2In Type HT-$Ni_{1+\delta}Sn$”, *J. Solid State Chem.,* **177**(2004), p.936-945.

58. A. Leineweber, “Variation of the Crystal Structures of Incommensurate LT′-$Ni_{1+\delta}Sn$ ($\delta = 0.35, 0.38, 0.41$) and Commensurate LT-$Ni_{1+\delta}Sn$ ($\delta = 0.47, 0.50$)

with Composition and Annealing Temperature", *J. Solid State Chem.*, **177**(2004), p.1197-1212.

59. S. Bader, W. Gust and H. Hieber, "Rapid Formation of Intermetallic Compounds by Interdiffusion in the Cu-Sn and Ni-Sn Systems", *Acta Metall. Mater.*, **43**(1995), p.329-337.
60. J. Haimovich, "Intermetallic Compound Growth in Tin and Tin-lead Platings over Nickel and its Effects on Solderability", *Welding Research Supplement*, **68**(1989), p.102-111.
61. V. Vuorinen, H. Yu, T. Laurila and J.K. Kivilahti, "Formation of Intermetallic Compounds between Liquid Sn and Various $CuNi_x$ Metallizations", *J. Electron. Mater.*, **37**(2008), p.792-805.
62. D.-G. Kim and S.-B. Jung, "Intermetallic Compound Formation and Growth Kinetics in Flip Chip Joints Using Sn-3.0Ag-0.5Cu Solder and Ni-P Under Bump Metallurgy", *Mater. Trans.*, **46**(2005), p.1295-1300.
63. V. Vuorinen, T. Laurila, H. Yu and J.K. Kivilahti, "Phase Formation between Lead-free Sn-Ag-Cu Solder and Ni(P)/Au Finishes", *J. Appl. Phys.*, **99**(2006), 023530.
64. K. Zeng and K.N. Tu, "Six Cases of Reliability Study of Pb-Free Solder Joints in Electronic Packaging Technology", *Mater. Sci. Eng. R-Rep.*, **38**(2002), p.55-105.

65. S.K. Kang and V. Ramachandran, “Growth Kinetics of Intermetallic Phases at the Liquid Sn and Solid Ni Interface”, *Scripta Metall.*, **14**(1980), p.421-424.

66. W.J. Thomlinson and H.G. Rhodes, “Kinetics of Intermetallic Compound Growth Between Nickel, Electroless Ni-P, Electroless Ni-B and Tin at 453 to 493K”, *J. Mater. Sci*., **22**(1987), p.1769-1772.

67. C.Y. Lee and K.L. Lin, “The Interaction Kinetics and Compound Formation between Electroless Ni-P and Solder”, *Thin Solid Films*, **249**(1994), p.201-206.

68. K.L. Lin and J.T. Chang, “The Elemental Interaction in the Electrodeposited Pb-Sn/Electroless Ni-P Deposit/Al Multilayer upon Heat Treatment”, *Scripta Metall.*, **30**(1994), p.559-564.

69. J.W. Jang, P.G. Kim, K.N. Tu, D.R. Frear and P. Thomson, “Solder Reaction-assisted Crystallization of Electroless Ni(P) Under-Bump Metallization in Low Cost Flip Chip Technology”, *J. Appl. Phys*., **85**(1999), p.8456-8463.

70. P.L. Liu, Z. Xu, and J.K. Shang, “Thermal Stability of Interface between Electroless Ni and Sn-Pb Eutectic Solder: Part A. Interfacial Chemistry and Microstructure”, *Metall. Mater. Trans. A*, **31**(2000), p.2857-2866.

71. H. Matsuki, H. Ibuka and H. Saka, “TEM Observation of Interfaces in a Solder Joint in a Semiconductor Device”, *Sci. Tech. Adv. Mater.*, **3**(2002), p.261-270.

72. J. G. Lee, F. Guo, K.N. Subramanian and J.P. Lucas, “Intermetallic Morphology

around Ni Particles in Sn-3.5Ag Solder”, *Solder. Surf. Mt. Technol.*, **14**(2002), p.11-17.

73. L.C. Shiau, C.E. Ho and C.R. Kao, “Reactions between Sn-Ag-Cu Lead-Free Solders and the Au/Ni Surface Finish in Advanced Electronic Packages”, *Solder. Surf. Mt. Technol.*, **14**(2002), p.25-29.

74. M.K. Bhargava and K.J. Schubert, “Crystal Structure of NiSn”, *J. Less-Common Met.*, **33**(1973), p.181-189.

75. C.W. Hwang, K. Suganuma, M. Kiso, and S. Hashimoto, “Interface Microstructures between Ni-P Alloy Plating and Sn-Ag-(Cu) Lead-Free Solders”, *J. Mater. Res.*, **18**(2003), p.2540-2543.

76. J.W. Yoon, C.B. Lee and S.B. Jung, “Growth of an Intermetallic Compound Layer with Sn-3.5Ag-5Bi on Cu and Ni-P/Cu during Aging Treatment”, *J. Electron. Mater.*, **32**(2003), p.1195-1202.

77. Y.-D. Jeon, K.-W. Paik, K.-W. Bok, W.-S. Choi and C.-L. Cho, “Studies of Electroless Nickel Under Bump Metallurgy-Solder Interfacial Reactions and Their Effects on Flip Chip Solder Joint Reliability”, *J. Electron. Mater.*, **31**(2002), p.520-528.

78. H. Lu, C.L. Kang, Stephen C.K. Wang and H. Gong, “Evaluation of Commercial Electroless Nickel Chemicals for a Low Cost Wafer Bumping Process”, *Semicond.*

Sci. Technol., **17**(2002), p911-917.

79. K.C. Hung and Y.C. Chan, “Study of Ni_3P Growth due to Solder Reaction Assisted Crystallization of Electroless Ni-P Metallization”, *J. Mater. Sci. Lett.*, **19**(2000), p.1755-1757.
80. J.W. Jang, P.G. Kim, K.N. Tu, D.R. Frear and P. Thompson, “Solder Reaction-Assisted Crystallization of Electroless Ni-P Under Bump Metallization in Low Cost Flip Chip Technology”, *J. Appl. Phys.*, **85**(1999), p.8456-8463.
81. Y.C. Lin and J.G. Duh, “Phase Transformation of the Phosphorus-Rich Layer in SnAgCu/Ni-P Solder Joints”, *Scripta Mater.*, **54**(2006), p.1661-1665.
82. Y.C. Lin, J.G. Duh and B.S. Chiou, “Wettability of Electroplated Ni-P in Under Bump Metallurgy with Sn-Ag-Cu Solder”, *J. Electron. Mater.*, **35** (2006), p.7-14.
83. Y.C. Lin and J.G. Duh, “Optimal Phosphorous Content Selection for the Soldering Reaction of Ni-P Under Bump Metallization with Sn-Ag-Cu Solder”, *J. Electron. Mater.* **35**(2006), p.1665-1671.
84. A. Kumar, M. He and Z. Chen, “Barrier Properties of Thin Au/Ni-P Under Bump Metallization for Sn-3.5Ag Solder”, *Surf. Coat. Tech.*, **198**(2005), p.283-286.
85. H.C. Pan and T.-E. Hsieh, “An Investigation of Diffusion Barrier Characteristics of an Electroless Co(W,P) Layer to Lead-Free SnBi solder”, *J. Electron. Mater.*, **40**(2011), p.330-339.

86. H.C. Pan and T.-E. Hsieh, “Diffusion Barrier Characteristics of Electroless Co(W,P) Thin Films to Lead-Free SnAgCu Solder”, *J. Electrochem. Soc.*, **158**(2011), p.123-129.

87. H.C. Pan and T.-E. Hsieh, “Diffusion barrier characteristics and shear fracture behaviors of eutectic PbSn solder/electroless Co(W,P) samples”, *Mater. Sci. Eng. B*, **177**(2012), p.61-68.

88. A. Lang and W. Jeitschko, “Two New Phases in the System Cobalt-Tin: The Crystal Structures of α- and β-$CoSn_3$”, *Z. Metallkd.*, **87**(1996), p.759-764.

89. M. Jiang, J. Sato, I. Ohnuma, R. Kainuma, and K. Ishida, “A Thermodynamic Assessment of the Co-Sn System”, *Computer Coupling of Phase Diagrams and Thermochemistry*, **28**(2004), p.213-220.

90. W. J. Zhu, H. S. Liu , J. Wang, and Z. P. Jin, “Formation of intermetallic compound (IMC) between Sn and Co substrate”, *J. Alloy Compd.*, **456**(2008), p.113-117.

91. W. J. Zhu, J. Wang, H. S. Liu , Z. P. Jin, and W. P. Gong, “The interfacial reaction between Sn–Ag alloys and Co substrate”, *Mater. Sci. Eng. A*, **456**(2007), p.109-113.

92. C. H. Wang and S. W. Chen, “Sn/Co solid/solid interfacial reactions”, *Intermetallics*, **16**(2008), p. 524-530.

93. C. H. Wang and S. W. Chen, “Cruciform pattern formation in Sn/Co couples”, *J. Mater. Res.*, **22**(2007), p. 3404-3409.

94. *Binary Alloy Phase Diagrams*, ed. by T. B. Massalski, ASM International, Materials Park, OH, (1986).

95. G. C. Chi and G. S. Cargill III, *J. Appl. Phys*., **50** (1979), p. 2713-2720.

96. K. Hüller, M. Sydow and G. Dietz, “Magnetic Anisotropy, Magnetostriction and Intermediate Range Order in Co-P Alloys”, *J. Magn. Magn. Mater*., **53**(1985), p.269-274.

97. M. Paunovic, P.J. Bailey, R.G. Schad and D.A. Smith, “Electrochemically Deposited Diffusion Barriers”, *J. Electrochem. Soc*., **141**(1994), p.1843-1850.

98. K. Hono and D.E. Laughlin, “Evidence of Phosphorous Segregation in Grain Boundaries in Electroless-plated Co-P Thin Film”, *J. Magn. Magn. Mater*., **80**(1989), L137-141.

99. T. Takayama, M. Y. Wey, and T. Nishizawa, *Trans. Jpn. Inst. Met.*, **22**(1981), p. 315-325.

100. L. A. Neumeier and J. L. Holman, *U. S. Bur. Mines Rep. Invest.* (1967), p. 6956.

101. *Handbook of Corrosion Engineering*, ed. by P.R. Roberge, McGraw-Hill, Hightstown, NJ, USA (2000), Chap.9, p.787.

102. 莊萬發，*無電解鍍金-化學鍍金技術*，復漢出版社，(1996)。

103. 曾威綱，“*無電鍍鈷合金薄膜對銅矽擴散阻障效能之研究*”，*逢甲大學*，*碩士論文*，民國 91 年。

104. N. Petrov, Y. Sverdlov and Y. Shacham-Diamand, “Electrochemical Study of the Electroless Deposition of Co(P) and Co(W,P) Alloy”, *J. Electrochem. Soc.*, **149**(2002), p.C187-C194.

105. *Physico-chemical Origins of the Chemical Reduction of Cobalt*, ed. by K.M. Gorbunova, Science Publishing, Moscow, (1974).

106. JSDEC Standard, JESD22-A103C.

107. JSDEC Standard, JESD22-B117A.

108. D.A. Porter, K.E. Easterling, *Phase Transformations in Metals & Alloys*, Chapman & Hall, London, (1981), Chap.1.

109. V.I. Dybkov and O.V. Duchenko, “Growth Kinetics of Compound Layers at the Nickel-bismuth Interface”, *J. Alloy Compd*., **234**(1996), p.295-300.

110. A. Sharif and Y.C. Chen, “Dissolution Kinetics of BGA Sn-Pb and Sn-Ag Solders with Cu Substrates during Reflow”, *Mater. Sci. Eng. B*, **106**(2004), p.126-131.

111. D.Q. Yu, C.M.L. Wu, C.M.T. Law, L. Wang and J.K.L. Lai, “Intermetallic Compounds Growth between Sn-3.5Ag Lead-free Solder and Cu Substrate by Dipping Method”, *J. Alloy Compd.*, **392**(2005), p.192-199.

112. D.G. Kim, J.W. Kim, S.S. Ha, B.I. Noh, J.M. Koo, D.W. Park, M.W. Ko and S.B.

Jung, “Effect of Reflow Numbers on the Interfacial Reaction and Shear Strength of Flip-chip Solder Joints ”, *J. Alloy Compd.,* **458**(2008), p.253-260.

113. M.O. Alam, Y.C. Chan and K.C. Hung, “Reliability Study of the Electroless Ni-P Layer against Solder Alloy”, *Microelectron. Reliab.,* **42**(2002), p.1065-1073.

114. C.B. Lee, S.B. Jung, Y.E. Shin and C.C. Shur, “Effect of Isothermal Aging on Ball Shear Strength in BGA Joints with Sn-3.5Ag-0.75Cu Solder”, *Mater. Trans.,* **43**(2002), p.1858-1863.

115. P.C. Shih and K.L. Lin, “Interfacial Microstructure and Shear Behavior of Sn-Ag-Cu Solder Balls Jointed with Sn-Zn-Bi Paste”, *J. Alloy Compd.,* **422**(2006), p.153-163.

116. J.W. Yoon, H.S. Chun and S.B. Jung, “Interfacial Reaction and Mechanical Characterization of Eutectic Sn-Zn/ENIG Solder Joints during Reflow and Aging”, *Mater. Trans.,* **46**(2005), p.2386-2393.

117. A. Sharif and Y.C. Chan, ”Investigation of Interfacial Reactions between Sn-Zn Solder with Electrolytic Ni and Electroless Ni(P) Metallization”, *J. Alloy Compd.,* **440**(2007), p.117-121.

118. M.N. Islam, Y.C. Chan, A. Sharif and M.O. Alam, “Comparative Study of the Dissolution Kinetics of Electrolytic Ni and Electroless Ni-P by the Molten Sn3.5Ag0.5Cu Solder Alloy”, *Microelectron. Reliab.,* **43**(2003), p.2031-2037.

119. S.M.L. Nai, J. Wei and M. Gupta, “Interfacial Intermetallic Growth and Shear Strength of Lead-free Composite Solder Joints”, *J. Alloy Compd.*, **473**(2009), p.100-106.

120. J.J. Guo, A.P. Xian, J.K. Shang, “Degradation of Solderability of Electroless Nickel by Phosphide Particles”, *Surf. Coat. Tech.*, **202**(2007), p.268-274.

121. Y.C. Sohn, J. Yu, S.K. Kang, D.Y. Shih and T.Y. Lee, “Spalling of Intermetallic Compounds during the Reaction between Lead-Free Solders and Electroless Ni-P Metallization”, *J. Mater. Res.*, **19**(2004), p.2428-2436.

122. J.W. Jang, L.N. Ramanathan, J.K. Lin, and D.R. Frear, “Spalling of Cu_3Sn Intermetallics in High-Lead 95Pb5Sn Solder Bumps on Cu Under Bump Metallization during Solid-state Annealing”, *J. Appl. Phys.*, **95**(2004), p.8286-8289.

123. B.L. Young, J.G. Duh, and G.Y. Jang, “Compound Formation for Electroplated Ni and Electroless Ni in the Under-bump Metallurgy with Sn-58Bi Solder during Aging”, *J. Electron. Mater.*, **32**(2003), p.1463-1473.

124. C.Y. Liu, H.K. Kim, K.N. Tu and P.A. Totta, “Dewetting of Molten Sn on Au/Cu/Cr Thin-Film Metallization”, *Appl. Phys. Lett.*, **69**(1996), p.4014-4016.

125. C. H. Wang and C. Y. Kuo, “Coupling Effect of the Interfacial Reaction in Co/Sn/Cu Diffusion Couples”, *J. Electron. Mater.*, **39**(2010), p. 1303-1308.

126. Y. K. Chen, “Sn-Co-Cu-Ni phase equilibria and Sn-Co-(Cu)/Ni interfacial reactions”, Master thesis, National Tsing Hua University, (2009).

127. C.E. Ho, R.Y. Tsai, Y.L. Lin and C.R. Kao, “Effect of Cu Concentration on the Reactions between Sn-Ag-Cu Solders and Ni”, *J. Electron. Mater.*, **31**(2002), p.584-590.

128. Y.C. Lin, T.Y. Shih, S.K. Tien and J.G. Duh, “Suppressing Ni-Sn-P Growth in SnAgCu/Ni-P Solder Joints”, *Scripta Mater.*, **56**(2007), p.49-52.

129. V. Vuorinen, T. Laurila, H. Yu and J.K. Kivilahti, “Phase Formation between Lead-free Sn-Ag-Cu Solder and Ni(P)/Au Finishes”, *J. Appl. Phys.*, **99**(2006), 023530.

130. X. Gu, Y.C. Chan, D. Yang and B.Y. Wu, “The Shearing Behavior and Microstructure of Sn-4Ag-0.5Cu Solder Joints on a Ni-P-Carbon Nanotubes Composite Coating”, *J. Alloy Compd.*, **468**(2009), p.553-557.

131. P. Liu, P. Yao and J. Liu, ”Effects of Multiple Reflows on Interfacial Reaction and Shear Strength of SnAgCu and SnPb Solder Joints with Different PCB Surface Finishes”, *J. Alloy Compd.*, **470**(2009), p.188-194.

132. C.W. Hwang, K. Suganuma, M. Kiso and S. Hashimoto, “Influence of Cu Addition to Interface Microstructure between Sn-Ag Solder and Au/Ni-6P Plating”, *J. Electron. Mater.*, **33**(2004), p.1200-1209.

133. J.W. Yoon, S.W. Kim and S.B. Jung, "Effect of Reflow Time on Interfacial Reaction and Shear Strength of Sn-0.7Cu Solder/Cu and Electroless Ni-P BGA Joints", *J. Alloy Compd.*, **385**(2004), p.192-198.

134. J.W. Yoon, S.W. Kim and S.B. Jung, "Interfacial Reaction and Mechanical Properties of Eutectic Sn-0.7Cu/Ni BGA Solder Joints during Isothermal Long-term Aging", *J. Alloy Compd.*, **391**(2005), p.82-89.

135. J.W. Yoon, S.W. Kim and S.B. Jung, "IMC Morphology, Interfacial Reaction and Joint Reliability of Pb-free Sn-Ag-Cu Solder on Electrolytic Ni BGA Substrates", *J. Alloy Compd.*, **392**(2005), p.247-252.

136. C.T. Lin, C.S. Hsi, M.C. Wang, T.C. Chang and M.K. Liang, "Interfacial Microstructures and Solder Joint Strengths of the Sn-8Zn-3Bi and Sn-9Zn-1Al Pb-free Solder Pastes on OSP Finished Printed Circuit Boards", *J. Alloy Compd.*, **459**(2008), p.225-231.

137. P. Yao, P. Liu and J. Liu, "Effects of Multiple Reflows on Intermetallic Morphology and Shear Strength of SnAgCu–*x*Ni Composite Solder Joints on Electrolytic Ni/Au Metallized Substrate", *J. Alloy Compd.*, **462**(2008), p.73-79.

138. A.K. Gain, T. Fouzder, Y.C. Chan, A. Sharif and W.K.C. Yung, "Investigation of Small Sn-3.5Ag-0.5Cu Additions on the Microstructure and Properties of Sn-8Zn-3Bi Solder on Au/Ni/Cu Pads", *J. Alloy Compd.*, **489**(2010), p.678-684.

139. H.T. Lee, S.Y. Hu, T.F. Hong and Y.F. Chen, “The Shear Strength and Fracture Behavior of Sn-Ag-*x*Sb Solder Joints with Au/Ni-P/Cu UBM”, *J. Electron. Mater.*, **37**(2008), p.867-873.
140. J. Shen and Y.C. Chan, “Effects of ZrO_2 Nanoparticles on the Mechanical Properties of Sn-Zn Solder Joints on Au/Ni/Cu Pads”, *J. Alloy Compd.*, **477**(2009), p.552-559.
141. S.Y. Chang, Y.C. Huang and Y.M. Lin, “Mechanical Property and Fracture Behavior Characterizations of 96.5Sn-3.0Ag-0.5Cu Solder Joints”, *J. Alloy Compd.*, **490**(2010), p.508-514.

Curriculum Vitae

2011/01

Hung-Chun Pan（潘虹君）

PERSONAL DATA

Born: March 25, 1978, Ping-Tung County, Taiwan, R.O.C.

Nationality: Taiwan, R.O.C.

Office Address: Department of Materials Science and Engineering, National Chiao-Tung University, 1001, Ta-Hsueh Rd., Hsinchu, Taiwan 30010, R.O.C.

Tel: 886-3-5712121 ext. 55338.

E-mail: jennifera_pan@yahoo.com.tw

EDUCARION

Ph.D. Candidate, Department of Materials Science and Engineering, National Chiao-Tung University, Hsinchu, Taiwan, Sept., 2002-present.

Master of Science, Department of Mechanical Engineering, Chang Gung University, Tao-Yuan County, Taiwan, Sept., 2000-July, 2002.

Bachelor of Science, Department of Mechanical Engineering, Yuan Ze University, Tao-Yuan County, Taiwan, Sept., 1996-July, 2000.

PUBLICATIONS

Journal Articles:

1. W.C. Wu, Tsung-Eong Hsieh, and **Hung-Chun Pan**, (2008), “Investigation of Electroless Co(W,P) Thin Film as the Diffusion Barrier of Under Bump Metallurgy”, *J. Electrochem. Soc.*, **155**(5), p.D369-D376.
2. **Hung-Chun Pan** and Tsung-Eong Hsieh, “An Investigation of Diffusion Barrier Characteristics of an Electroless Co(W,P) Layer to Lead-Free SnBi solder”, *J. Electron. Mater.*, **40**(3)(2011), p.330-339.
3. **Hung-Chun Pan** and Tsung-Eong Hsieh, “Diffusion Barrier Characteristics of Electroless Co(W,P) Thin Films to Lead-Free SnAgCu Solder”, *J. Electrochem. Soc.*, **158**(11)(2011), p.123-129.
4. **Hung-Chun Pan** and Tsung-Eong Hsieh, “Diffusion barrier characteristics and shear fracture behaviors of eutectic PbSn solder/electroless Co(W,P) samples”, *Mater. Sci. Eng. B*, **177**(1)(2012), p.61-68.

Conference Papers:

1. 潘虹君、吳文成、謝宗雍, “無電鍍鈷鎢磷擴散阻障層之微觀分析研究”, 2007年中國材料科學年會論文集, P03-118 (2007).
2. **Hung-Chun Pan** and Tsung-Eong Hsieh, “Investigation of Electroless Co(W,P)

Layers as the Diffusion Barrier of Under Bump Metallurgy”, *International Materials Research Conference (iMRS)*, Chongqing, China, C.4.11, 9-12 June (2008).

3. **Hung-Chun Pan** and Tsung-Eong Hsieh, “An Investigation of Diffusion Barrier Characteristics of Electroless Co(W,P) Layer to Lead-Free SnBi Solder”, *5th Annual Device Packaging Conference (DPC2009)* held by *International Microelectronics And Packaging Society (IMAPS)*, Scottsdale, Arizona, USA, D.3.7, 9-12 March (2009).
4. **Hung-Chun Pan** and Tsung-Eong Hsieh, “A Study of Diffusion Barrier Characteristics of Electroless Co(W,P) Layers to Lead-free SnAgCu Solder”, *Materials Research Society (MRS) 2008 SPRING MEETING*, San Francisco, CA, USA, D.3.7, 14-17 April (2009).

AWARDS

1. 2007年*中國材料科學*，學生論文獎佳作獎, Nov. (2007).
2. 2008 *iMRS*, Best Student Paper Award, June (2008).